

AD-A010 484

GASDYNAMIC LASERS: THEORY EXPERIMENT AND  
THE STATE OF THE ART

John D. Anderson, Jr.

Maryland University

Prepared for:

Air Force Office of Scientific Research

May 1974

DISTRIBUTED BY:

**NTIS**

National Technical Information Service  
U. S. DEPARTMENT OF COMMERCE  
5285 Port Royal Road, Springfield Va. 22151



Department of Aerospace Engineering  
University of Maryland, College Park

ADA010484

Gasdynamic Lasers: Theory  
Experiment and the State  
of the Art

John D. Anderson, Jr.

Presented at the von Karman Institute for Fluid  
Dynamics, Brussels, Belgium as part of Lecture  
Series 65, "High Power Gas Lasers," March 1974

This research was supported in part by the  
Air Force Office of Scientific Research  
under Grant No. 74-2575

Distribution of this report is unlimited

May 1974

AIR FORCE OFFICE OF SCIENTIFIC RESEARCH (AFOSR)  
NOTICE OF TRANSMISSION TO THE

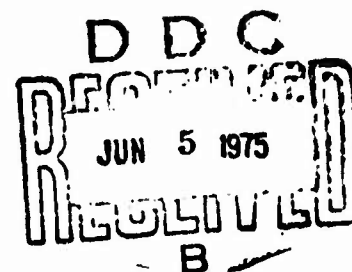
This technical report has been reviewed and is  
approved for public release under AFR 150-12 (7b).

Distribution is unlimited.

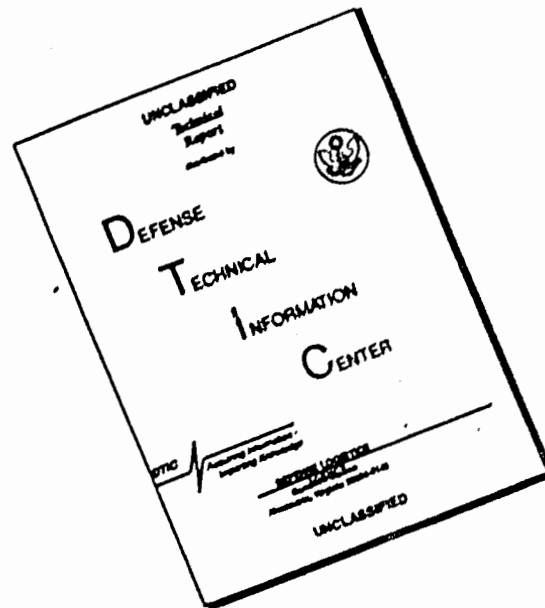
D. W. TAYLOR

Technical Information Officer

Reproduced by  
NATIONAL TECHNICAL  
INFORMATION SERVICE  
U.S. Department of Commerce  
Springfield, VA 22151



# DISCLAIMER NOTICE



THIS DOCUMENT IS BEST QUALITY AVAILABLE. THE COPY FURNISHED TO DTIC CONTAINED A SIGNIFICANT NUMBER OF PAGES WHICH DO NOT REPRODUCE LEGIBLY.

GASDYNAMIC LASERS: THEORY,  
EXPERIMENT AND THE  
STATE-OF-THE-ART

BY

John D. Anderson, Jr.  
Professor and Chairman  
Department of Aerospace Engineering  
University of Maryland  
College Park, Maryland, U.S.A. 20742

Prepared for the course entitled  
High Energy Gas Lasers  
von Karman Institute for Fluid Dynamics  
11-15 March 1974



REPORT DOCUMENTATION PAGE		READ INSTRUCTIONS BEFORE COMPLETING FORM
1. REPORT NUMBER AFOSR - TR - 75 - 0671	2. GOVT ACCESSION NO.	3. RECIPIENT'S CATALOG NUMBER
4. TITLE (and Subtitle)  GASDYNAMIC LASERS: THEORY EXPERIMENT AND THE STATE OF THE ART		5. TYPE OF REPORT & PERIOD COVERED INTERIM
		6. PERFORMING ORG. REPORT NUMBER
7. AUTHOR(s) JOHN D ANDERSON JR		8. CONTRACT OR GRANT NUMBER(s) AFOSR 74-2575
9. PERFORMING ORGANIZATION NAME AND ADDRESS UNIVERSITY OF MARYLAND DEPARTMENT OF AEROSPACE ENGINEERING COLLEGE PARK, MARYLAND 20742		10. PROGRAM ELEMENT, PROJECT, TASK AREA & WORK UNIT NUMBERS 681308 9750-02 61102F
11. CONTROLLING OFFICE NAME AND ADDRESS AIR FORCE OFFICE OF SCIENTIFIC RESEARCH/NA 1400 WILSON BOULEVARD ARLINGTON, VIRGINIA 22209		12. REPORT DATE May 1974
		13. NUMBER OF PAGES
14. MONITORING AGENCY NAME & ADDRESS (if different from Controlling Office)		15. SECURITY CLASS. (of this report) UNCLASSIFIED
		15a. DECLASSIFICATION/DOWNGRADING SCHEDULE
16. DISTRIBUTION STATEMENT (of this Report)  Approved for public release; distribution unlimited.		
17. DISTRIBUTION STATEMENT (of the abstract entered in Block 20, if different from Report)		
18. SUPPLEMENTARY NOTES		
19. KEY WORDS (Continue on reverse side if necessary and identify by block number) GASDYNAMIC LASER HIGH POWER LASER LASER		
20. ABSTRACT (Continue on reverse side if necessary and identify by block number) A set of lecture notes is presented for use in a course on Gasdynamic Lasers. The subject matter includes Physics considerations, calculation of gasdynamic laser performance, comparison between theory and experiment, optical cavity considerations and fluid-dynamic problems. The approach is to present the basic physics and aerodynamics leading to actual ability to design a gasdynamic laser.		

## TABLE OF CONTENTS

	<u>Page</u>
I. GASDYNAMIC LASERS: THEORY AND EXPERIMENT	1
A. INTRODUCTION	1
B. ELEMENTARY PHYSICS	4
1. Energy Levels and Population Inversion	4
2. Why Does a Population Inversion Make a Laser Work?	9
3. Definition and Calculation of Small-Signal Gain	11
4. CO <sub>2</sub> -H <sub>2</sub> -H <sub>2</sub> O or He System	17
C. CALCULATION OF GASDYNAMIC LASER PERFORMANCE	21
1. Analysis	21
2. Vibrational Model	27
3. Results	32
4. Comparison with Basov	33
5. Coupled and Uncoupled Flows	38
6. Recapitulation	43
7. Power Extraction	44
D. COMPARISON BETWEEN THEORY AND EXPERIMENT	49
1. Kinetic Rate Data	49
2. Nonequilibrium Gas Dynamics	49
3. Small-Signal Gain	50
4. NOL 3-Megawatt Arc Tunnel	52
5. NOL 12.7 cm Shock Tunnel	60
6. Arc Tunnel Experiments	69
7. Shock Tunnel Experiments	75
8. Other Experiments	78

	<u>Page</u>
E. INVERSIONS BEHIND NORMAL SHOCK WAVES	83
II. GASDYNAMIC LASERS: STATE-OF-THE-ART	89
A. INTRODUCTION	89
B. INCREASED H <sub>2</sub> O CONTENT	91
C. INCREASED TEMPERATURE	98
D. BINARY SCALING	103
E. CARBON MONOXIDE GDL	108
F. DOWNSTREAM MIXING GASDYNAMIC LASERS	110
III. OPTICAL CAVITY CONSIDERATIONS AND FLUID DYNAMIC PROBLEMS	120
A. INTRODUCTION	120
B. CAVITY TYPES	121
1. Amplifiers	121
2. Resonators	123
C. CAUSES OF BEAM DISTORTION IN GDL's	128
1. Shock Waves	128
2. Turbulence	134
3. Non-uniform Gain Profiles	135
D. AERODYNAMIC WINDOWS	139
IV. EPILOGUE	147
REFERENCES	148
APPENDIX A: The Effect of Kinetic Rate Uncertainties on Gasdynamic Laser Performance	A-1
APPENDIX B: Kinetic Rates	A-5
APPENDIX C: Investigation of a Mixing CO <sub>2</sub> GDL	C-5

GASDYNAMIC LASERS: THEORY,  
EXPERIMENT AND THE STATE-OF-THE-ART

by

John D. Anderson, Jr.  
Professor and Chairman  
University of Maryland  
College Park, Maryland, U.S.A. 20742

I. GASDYNAMIC LASERS: THEORY and EXPERIMENT

A. INTRODUCTION

Consider in your imagination a supersonic wind tunnel, such as those commonly found in many aerodynamic laboratories. However, when this particular tunnel is turned on, we do not measure the lift and drag on an aerodynamic model, or the pressure and heat transfer distributions over a surface. Instead, when the switch is thrown for this particular tunnel, we see a very powerful laser beam propagating from the test section. Indeed, this is not a wind tunnel at all, but rather it is a gasdynamic laser.

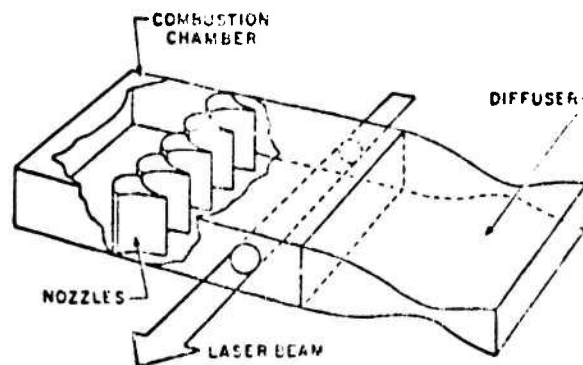
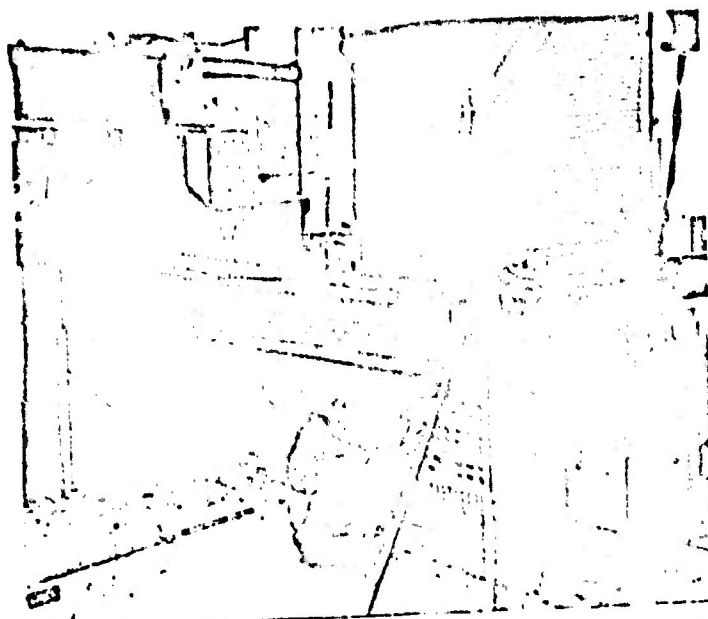


Fig. 1

Schematic Drawing of Gasdynamic Laser

As shown schematically in Figure 1, a gasdynamic laser takes a hot, high pressure mixture of gases (usually  $\text{CO}_2$ ,  $\text{N}_2$  and  $\text{H}_2\text{O}$  or He) and expands this mixture very rapidly through a supersonic nozzle. During the expansion, the gas is turned into a laser medium (a population inversion is created). The supersonic laser gas then passes into the test section (laser cavity), where, if mirrors are placed on both sides of the test section, a beam of laser energy is extracted perpendicular to the flow. The supersonic stream then enters a diffuser, where it is shocked down to subsonic speeds and generally exhausted to the atmosphere.

Why are gasdynamic lasers so important? The answer, purely and simply, is that they are very high power devices. In fact, gasdynamic lasers (GDL's) have spearheaded a breakthrough in high energy laser devices. For example, a multimode, continuous wave power output of 60 KW from a  $\text{CO}_2$ - $\text{N}_2$  GDL has been reported by Gerry<sup>1</sup>, and an average laser power of 400 KW has been extracted for four milliseconds from a shock tube GDL by Klosterman and Hoffman<sup>2</sup> working in the laser group at the University of Washington. A major factor in this breakthrough is that, unlike early electric discharge lasers with their attendant problems of arc discharges in large volumes, GDL's can be scaled to large sizes without major physical complications. A picture of a large-scale GDL is shown in Figure 2.



Reproduced from  
best available copy.

Fig. 2 *Gasdynamic Laser at AVCO Corp.*

A historical note is in order here. The concept of a gasdynamic laser was initiated as early as 1962 by Basov and Oraevskii<sup>3</sup>, who suggested that population inversions in molecular systems could be created by rapid heating or cooling of the system. Subsequently, in 1965 Hurle and Hertzberg<sup>4</sup> suggested that such cooling and population inversions could be obtained in the rapid, nonequilibrium expansion of an initially hot gas through a supersonic nozzle. They considered the specific case of electronic level inversions in expanding Xe, but were unsuccessful in measuring such inversions in the laboratory. Then, Kantowitz combined this idea with his previous work on vibrational nonequilibrium in CO<sub>2</sub> (see Reference 5), and in 1966, he and a group of physicists and engineers at the AVCO Everett Research Laboratory operated the first GDL, using a mixture of CO<sub>2</sub>-H<sub>2</sub>-H<sub>2</sub>O (see Reference 1). At about the same time, Basov et al<sup>6</sup> carried out a theoretical analysis of population inversions in CO<sub>2</sub>-N<sub>2</sub> expanding mixtures, and predicted that substantial inversions can indeed occur under suitable conditions for the gas mixture ratio and the nozzle reservoir pressure and temperature.

However, Basov missed an essential point, namely, that the inclusion of a "catalyst" such as  $H_2O$  or He is necessary for the attainment of reasonable population inversions. Basov used older values of the vibrational energy exchange rates which resulted in optimistic values of the population inversions; indeed, using more recent rates as compiled by Taylor and Bitterman<sup>7</sup>, Anderson<sup>8</sup> has shown that the  $CO_2-H_2$  mixtures considered by Basov et al do not yield significant inversions. The group at AVCO recognized this fact, and have reported experiments using  $CO_2-H_2-H_2O$  mixtures as early as 1966<sup>1</sup>. Theoretical calculations showing the beneficial role of  $H_2O$  were reported by Anderson<sup>8</sup> in 1969. The exact role of  $H_2O$  or He as a catalyst is discussed later in these notes.

Since these initial experiments and calculations, the technology and fundamental understanding of  $CO_2-H_2$  GDL's has grown precociously. This growth is exemplified by experiments carried out in arc tunnels<sup>9-12</sup>, shock tunnels<sup>2,11,13-17</sup> and combustion driven devices<sup>1,18-20</sup>, and by theoretical calculations reported in References 6,8,11,12,21-26. Moreover, gasdynamic lasers using CO as the lasing medium have also been demonstrated<sup>29</sup>. It is the purpose of these notes to bring the reader up-to-date in this state-of-the-art.

## B. ELEMENTARY PHYSICS

### 1. Energy Levels and Population Inversion

Consider a collection of molecules in a gas. Pick one of the molecules and examine it. The molecule is moving about in space -- hence it has translational energy; it is rotating about its principal axes -- hence it has rotational kinetic energy; the atoms that make up the molecule may be vibrating back and forth from some equilibrium position -- hence

it has vibrational kinetic and potential energy; and finally, the electrons move about the nuclei of the molecule -- hence it has kinetic and potential energy of electronic origin. However, the amazing quality of these various forms of molecular energy is that they can not be any arbitrary value. Rather, one of the most important discoveries of modern physics is that the molecule, at any given instant, has to occupy one of a very specific set of energy levels, i.e., the energy values of a molecule are quantized. This is shown schematically in Figure 3. Now, instead of one molecule, imagine the whole collection, say  $10^6$  molecules, and look at the first quantized energy level  $\epsilon_0$  (the ground state). There may be 400,000 molecules in this level at some instant in time. The number 400,000 is called the population  $N_0$  of the  $\epsilon_0$  level. Next, look at the first excited level,  $\epsilon_1$ ; there may be 200,000 molecules in this level, hence  $N_1 = 200,000 =$  the population of the  $\epsilon_1$  level; and so forth. The set of numbers,  $N_0, N_1, N_2, \dots, N_i, \dots$  is called the population distribution over the energy levels of the gas. The nature of this population distribution is of vital importance for laser action. For example, consider the vibrational energy of a molecular gas. If the gas is in thermodynamic equilibrium, the population distribution will exponentially decrease with increasing  $\epsilon_i$ , as shown on the left of Figure 4, i.e., it will follow a Boltzmann distribution. A major characteristic of this equilibrium distribution is that  $N_{i+1} < N_i$ . However, if the gas is disturbed at any instant, say by means of an electric discharge, or by a very sudden temperature change, then the population distribution can become a



↑ INCREASING ENERGY

•  
•  
•  
 $\frac{\epsilon_i, N_i}{}$   
•  
•  
•  
 $\frac{\epsilon_3, N_3}{}$   
 $\frac{\epsilon_2, N_2}{}$   
 $\frac{\epsilon_1, N_1}{}$   
 $\frac{\epsilon_0, N_0}{}$

$\boxed{\epsilon_i}$  ENERGY OF THE  $i^{\text{th}}$  LEVEL

$\boxed{N_i}$  NUMBER OF GAS PARTICLES  
IN THE  $i^{\text{th}}$  LEVEL AT ANY  
INSTANT IN TIME, i.e.,  
THE POPULATION OF THE  
 $i^{\text{th}}$  LEVEL

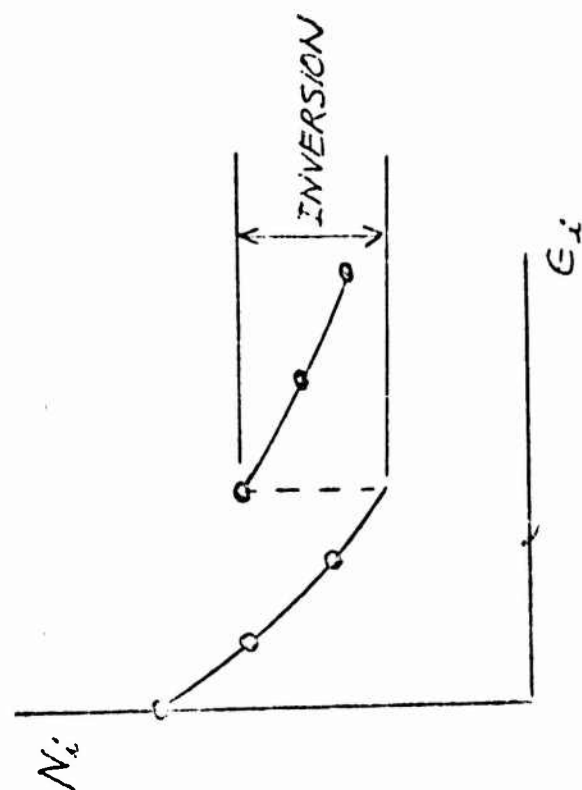
AT ANY INSTANT IN TIME,  
THE SET OF NUMBERS

$\boxed{N_0, N_1, N_2, N_3, \dots, N_i, \dots}$

IS CALLED THE POPULATION  
DISTRIBUTION

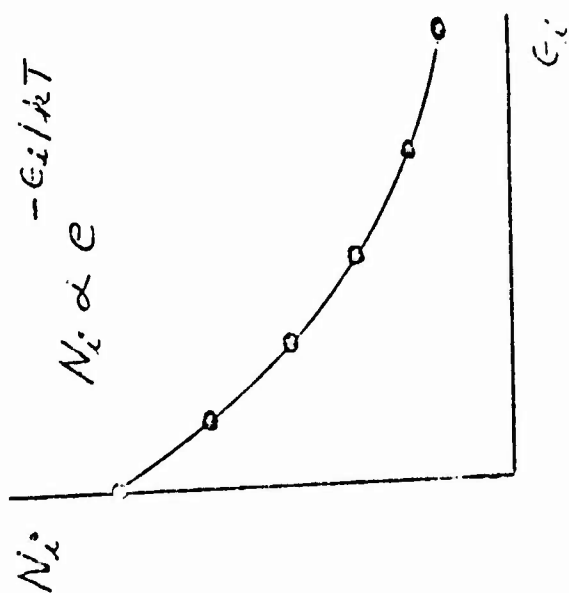
Fig. 3

NON-EQUILIBRIUM



$N_{i+1} > N_i$   
POPULATION  
INVERSION

EQUILIBRIUM



$N_{i+1} < N_i$

Fig. 4

nonequilibrium distribution, and it is even possible that, at some instant,  $N_{i+1} > N_i$ . This situation, where the number of molecules in a higher lying energy level is greater than the number in a lower lying level, is called a population inversion. The population inversion is the essence of laser action, and the attainment of this population inversion by means of rapid cooling of the gas is the essence of a gasdynamic laser. Specifically, when a gas expands through a supersonic nozzle, as shown in Figure 5, the gas temperature decreases very rapidly. Indeed, a fluid element moving through the nozzle can experience temperature changes as high as  $10^6$  degrees per second in the throat region of the nozzle. In fact, expansion through a minimum-length supersonic nozzle is the fastest practical means of cooling a gas. Therefore, it is reasonable to expect that, for certain conditions, a population inversion can be created in such an expansion.

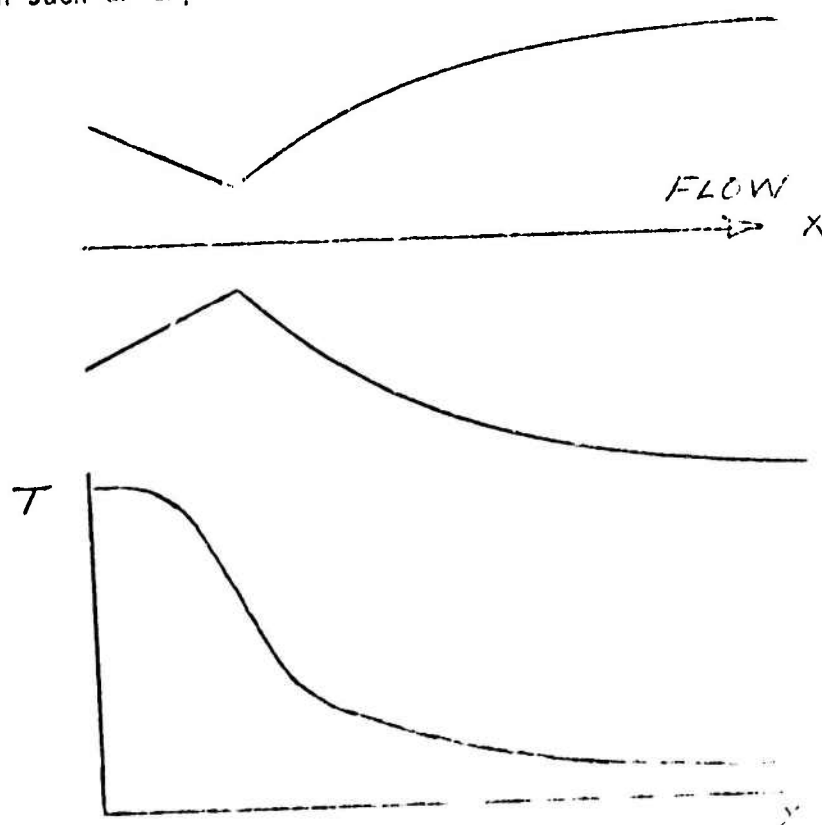


Fig. 5

With the above discussion in mind, the pivotal and first problem in studying, understanding and analyzing a gasdynamic laser is to examine the nonequilibrium flow through a nozzle, and the behavior of this flow as it moves downstream through the laser cavity. Specifically, we wish to calculate the population distribution as it varies through the nozzle for a mixture of  $\text{CO}_2\text{-N}_2$  and  $\text{H}_2\text{O}$  or He, and we wish to examine the conditions under which a population inversion will develop. This will be the subject of Section C of these notes. However, before we address this problem, we should answer the following question.

## 2. Why Does a Population Inversion Make a Laser Work?

Consider two energy levels of the molecules in a gas. There are three mechanisms by which these energy levels interact with radiation: spontaneous emission, stimulated emission, and absorption. These are illustrated in Figure 6.

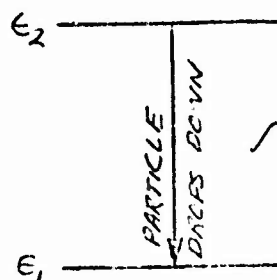
Now, consider a single molecule in a field of radiation, where the radiative intensity per unit frequency is  $I_\nu$ .

$(A_{21})_\nu$  = number of spontaneous radiative transitions per second per particle per unit frequency. This is called the Einstein spontaneous emission coefficient, and sometimes the Einstein transition probability.

$(B_{21})_\nu I_\nu$  = number of induced radiative transitions per second per particle per unit frequency.  $(B_{21})_\nu$  is the Einstein induced emission coefficient.

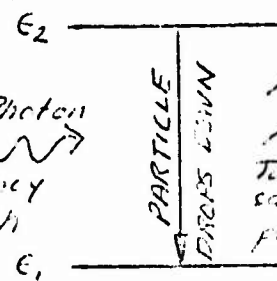
$(B_{12})_\nu I_\nu$  = number of radiative transitions per second per particle per unit frequency due to absorption.  $(B_{12})_\nu$  is the Einstein absorption coefficient.

Consider a slab of gas of geometric thickness  $dx$ , as shown in Figure 6. Let  $I_\nu$  be the radiative intensity (energy per second per unit area) incident on the left side of the slab, and let  $(dI)_\nu$  be the



Photon is emitted with energy  $h\nu = E_2 - E_1$ . It can be emitted in any direction.

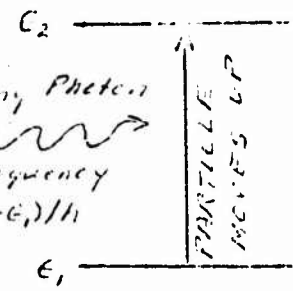
SPONTANEOUS EMISSION



Incident Photon of frequency  $\nu = (E_2 - E_1)/h$

Two photons of exactly same frequency, in phase with and in same direction as incident photon.

STIMULATED EMISSION



Incident Photon of frequency  $\nu = (E_2 - E_1)/h$

ABSORPTION

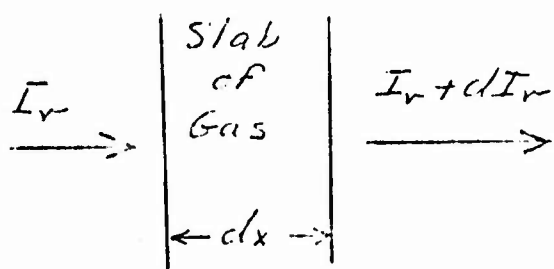


Fig. 6

change in intensity while traversing the slab. Also, let  $N_1$  and  $N_2$  be the number of molecules per unit volume in the  $\epsilon_1$  and  $\epsilon_2$  energy levels respectively. Then, from the above definitions, we can simply write down

$$(dI)_r = \left[ \underbrace{(A_{21})_r N_2}_{\text{spontaneous emission}} + \underbrace{(B_{21})_r I_r N_2}_{\text{induced emission}} - \underbrace{(B_{12})_r I_r N_1}_{\text{absorption}} \right] \nu_r dx \quad (1)$$

For the infrared wavelengths characteristic of molecular lasers, the spontaneous emission is negligible<sup>12</sup>. Also, in general,  $(B_{21})_\nu = \frac{g_1}{g_2} (B_{12})_\nu$ , as shown in Reference 12 and in most modern physics textbooks. Here,  $g_1$  and  $g_2$  are statistical weights of the levels. Hence, eq. (1)

becomes

$$\frac{(dI)_r}{I_r} = (B_{12})_r \left( \frac{g_1}{g_2} N_2 - N_1 \right) h\nu_r dx \quad (2)$$

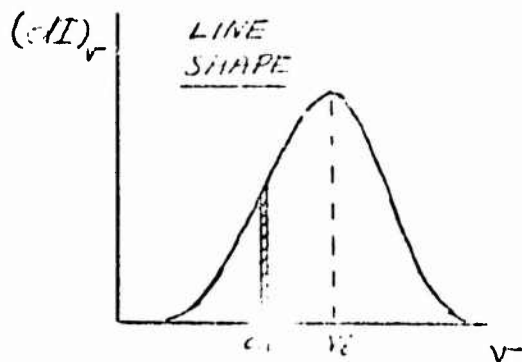
Now we can answer our original question. Looking at eq. (2),  $(dI)_\nu/I_\nu$  will be positive when  $(\frac{g_1}{g_2} N_2 - N_1) > 0$ , i.e., when a population inversion exists between the  $\epsilon_2$  and  $\epsilon_1$  energy levels. Hence, a population inversion leads to an amplification of the radiative intensity  $I_\nu$ . This is the laser effect, and this is why a population inversion makes a laser work!

### 3. Definition and Calculation of Small-Signal Gain

The small-signal laser gain is an extremely important figure of merit for gas laser devices; it is to laser physicists what lift and drag coefficients are to aerodynamicists. It is also a direct measurement of the population inversion. Everything else being equal, the higher the small-signal gain, the easier laser action can be obtained in a gas. Therefore, because we have just discussed the reasons why a population inversion laser work, we now extend this discussion to the analysis of small-signal gain. Also, the following results are necessary

for our subsequent discussions on the theory and experimental measurements of gasdynamic laser performance.

Let us consider stimulated emission and absorption, ignoring spontaneous emission as stated previously. Consider again the slab of



gas of geometric thickness,  $dx$ , with radiation of intensity  $I_\nu$  (per unit frequency) incident normally on the slab as shown in Fig. 6. The radiative intensity absorbed in a given spectral line of the gas is  $(dI)_\nu$  (per unit frequency).

Due to line broadening effects in the gas (natural, Doppler and collision),  $(dI)_\nu$  varies over a narrow frequency range, as shown in the sketch on the left. This gives rise to the line shape. The intensity of radiation between  $\nu$  and  $\nu+d\nu$  is  $(dI)_\nu d\nu$ . The integrated radiative intensity (total intensity absorbed by the line) is

$$dI = \int_{\nu} (dI)_\nu d\nu$$

The spectral absorption coefficient,  $\alpha_\nu$ , is defined as

$$(dI)_\nu = -\alpha_\nu I_\nu dx \quad (3)$$

Examining eq. (3), if  $I_\nu$  decreases as it traverses the slab of gas, then  $dI_\nu$  is negative and  $\alpha_\nu$  is a positive number. On the other hand, if  $I_\nu$  increases as in the laser effect, then  $dI_\nu$  is positive, and  $\alpha_\nu$  has to be a negative quantity. Rather than deal with a "negative absorption coefficient" a new coefficient is defined as

$$(dI)_\nu = G_{0\nu} I_\nu dx \quad (4)$$

where  $G_0$  is the small-signal gain coefficient.

$$G_{0\nu} = -\alpha \quad (5)$$

Since the small signal gain coefficient is the same as a "negative absorption coefficient", let us pursue our discussion in terms of the absorption coefficient. Comparing eqs. (2) and (3), we see that

$$\alpha_\nu = h\nu (B_{12})_\nu \left( N_1 - \frac{g_1}{g_2} N_2 \right) \quad (6)$$

It is common to express  $(B_{12})_\nu$  in terms of the Einstein coefficient for spontaneous emission,  $(A_{21})_\nu$ , where (see, for example, Ref. 30)

$$(A_{21})_\nu = \frac{8\pi h\nu^3}{c^2} (L_{12})_\nu$$

Thus, eq. (6) becomes,

$$\alpha_\nu = \frac{c^2}{8\pi\nu^2} (A_{21})_\nu \left( N_1 - \frac{g_1}{g_2} N_2 \right) \quad (7)$$

Eq. (7) gives the spectral absorption coefficient,  $\alpha_\nu$ . Define the integrated absorption coefficient as  $\int \alpha_\nu d\nu$  where the integral is taken over the entire spectral line.

Thus

$$\int_\nu \alpha_\nu d\nu = \frac{c^2}{8\pi\nu^2} \left( N_1 - \frac{g_1}{g_2} N_2 \right) \int_\nu (A_{21})_\nu d\nu \quad (8)$$

Note: The interval of integration over  $\nu$  is small (lines are usually narrow), so that  $\nu$  in the factor  $c^2/8\pi\nu^2$  in eq. (8) can be considered constant. Letting  $\int (A_{21})_\nu d\nu \equiv A_{21}$ , we have

$$\int_\nu \alpha_\nu d\nu = \frac{c^2}{8\pi\nu^2} A_{21} \left( N_1 - \frac{g_1}{g_2} N_2 \right) \quad (9)$$



Since  $\frac{c}{\nu} = \lambda$ , eq. (9) becomes

$$\int_{\nu} \mathcal{A}_{\nu} d\nu = \frac{\lambda^2}{8\pi} A_{21} \left( N_1 - \frac{g_1}{g_2} N_2 \right) \quad (10)$$

Eq. (10) gives the integrated absorption coefficient. Eq. (10) is more useful than eq. (7) because  $A_{21}$ , not  $(A_{21})_0$ , is available from laboratory measurements. To see this more clearly, recall eq. (2).

$$(dI)_r = -(B_{12})_r \left( N_1 - \frac{g_1}{g_2} N_2 \right) I_r h\nu c dx$$

$$(dI)_r = \frac{c^2}{8\pi h \nu^3} (A_{21})_r \left( N_1 - \frac{g_1}{g_2} N_2 \right) I_r h\nu c dx$$

$$(dI)_r = \frac{\lambda^2}{8\pi} (A_{21})_r \left( N_1 - \frac{g_1}{g_2} N_2 \right) I_r c dx \quad (11)$$

Now, integrate eq. (11) over the thickness of the slab. Let  $L$  = slab thickness

$$\int_{I_{r,in}}^{I_{r,out}} \frac{(dI)_r}{I_r} = - \frac{\lambda^2}{8\pi} (A_{21})_r \left( N_1 - \frac{g_1}{g_2} N_2 \right) \int_0^L c dx$$

$$\frac{I_{r,out}}{I_{r,in}} = e^{-\frac{\lambda^2}{8\pi} (A_{21})_r \left( N_1 - \frac{g_1}{g_2} N_2 \right) L}$$

For small values of the exponent, i.e., small  $L$ ,

$$\frac{I_{r,out}}{I_{r,in}} = 1 - \frac{\lambda^2}{8\pi} (A_{21})_r \left( N_1 - \frac{g_1}{g_2} N_2 \right) L + \dots \quad (12)$$

The total radiative intensity absorbed over the entire spectral line is

$I_{abs}$ , where

$$I_{abs} = \int_{\nu} (I_{r,in} - I_{r,out}) d\nu \quad (13)$$

Assume that a continuous light source is used in an absorption experiment, i.e.,  $I_{r,in}$  is constant over the frequency interval of the spectral line.

Combining eqs. (12) and (13):

$$I_{abs} = \int_{\nu} \left[ I_{rin} - I_{rout} + I_{rin} \frac{\lambda^2}{8\pi} (A_{21})_{\nu} \left( N_1 - \frac{g_1}{g_2} N_2 \right) L \right] c/\nu$$

$$I_{abs} = I_{rin} \frac{\lambda^2}{8\pi} \left( N_1 - \frac{g_1}{g_2} N_2 \right) L \int_{\nu} (A_{21})_{\nu} c/\nu$$

$$I_{abs} = \frac{\lambda^2 A_{21}}{8\pi} \left( N_1 - \frac{g_1}{g_2} N_2 \right) L I_{rin} \quad (14)$$

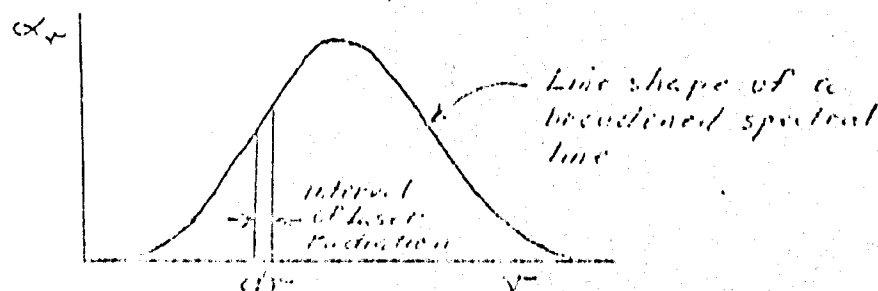
$I_{abs}$  is measured in the lab. In turn,  $A_{21}$  is calculated from eq. (14). Therefore, it is  $A_{21}$ , not  $(A_{21})_{\nu}$ , that is usually obtained from experiment. Thus, as stated earlier, eq. (10) for the integrated absorption coefficient is more directly related to experimental observation than is eq. (7) for the spectral absorption coefficient. Also, keep in mind that  $A_{21}$  is a physical constant of the molecule.

We have seen that in a conventional absorption experiment using a continuous light source, it is the integrated absorption coefficient  $\int \alpha_{\nu} d\nu$  and hence  $A_{21}$  which is obtained from the data. Values for  $A_{21}$ , and also for the radiative lifetime,

$$\tau \equiv \frac{1}{A_{21}}$$

are commonly quoted in the literature.

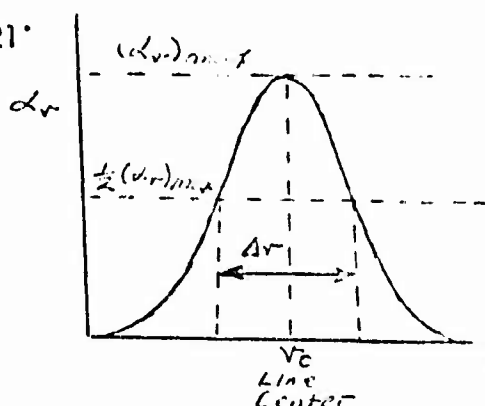
Now, consider laser radiation. This radiation is highly monochromatic. The laser cavity is generally tuned to emit radiation over a very small frequency interval. This interval is usually much smaller than the linewidth of a spectral line.



BEST AVAILABLE COPY

Hence, the absorption coefficient measured with laser radiation is the spectral absorption coefficient,  $\alpha_\nu$ .

Now, let us relate  $\alpha_\nu$  to the integrated absorption coefficient and to  $A_{21}$ .



Define a line shape factor,

$g(\nu, \nu_0)$  as:

$$\alpha_\nu = g(\nu, \nu_0) \int \alpha_\nu d\nu \quad (15)$$

where  $\int \alpha_\nu d\nu$  is obtained

from eq. (10).

Thus, from the definition, eq. (15),  $\int g(\nu, \nu_0) d\nu = 1$  where, as usual, the interval of integration is over the entire spectral line.

For pressures above 10-20 torr, the line shape is dominated by collision broadening (or pressure broadening). It has been demonstrated that, for this case, the line shape is a Lorentz curve (see for example, Ref. 30).

$$g(\nu, \nu_0) = \frac{\Delta \nu}{2\pi} \frac{1}{[(\nu - \nu_0)^2 + (\Delta \nu/2)^2]} \quad (16)$$

Here,  $\Delta \nu$  is the line width (see sketch), given by

$$\Delta \nu = \frac{Z}{\pi} \quad (17)$$

where  $Z$  is the molecular collision frequency.

For absorption at line center,  $\nu - \nu_0 = 0$  and, from eqs. (15), (16) and (17),

$$\alpha_\nu = \frac{2}{\pi \Delta \nu} \int \alpha_\nu d\nu = \frac{2}{Z} \int \alpha_\nu d\nu$$

Substitute eq. (10) into the above

$$\alpha_\nu = \frac{\lambda^2}{4\pi} \frac{A_{21}}{N_1 - \sum_{j=2}^J N_j} \left( N_1 - \sum_{j=2}^J N_j \right) \quad (18)$$

Now, recalling our definition of small-signal gain coefficient, eq. (4), and combining eqs. (5) and (18), we have

$$G_0 = \frac{\lambda^2}{4\pi} \frac{N_{21}}{\tau_{12}} \left( \frac{g_1}{g_2} N_2 - N_1 \right) \quad (19)$$

In terms of the radiative lifetime,  $\tau_{12} = 1/\Lambda_{21}$ ,

$$G_0 = \frac{\lambda^2}{4\pi \tau_{12}} Z \left( \frac{g_1}{g_2} N_2 - N_1 \right) \quad (20)$$

Eq. (20) is our desired result for small-signal gain coefficient.

Note that, for a given gas, the number densities,  $N_i$ , are proportional to pressure,  $p$ , whereas the collision frequency is proportional to  $p/T^{1/2}$ , where  $T$  is temperature. Hence, eq. (20) indicates that, for oscillation at line center (which is the case for most lasers),  $G_0$  is explicitly independent of pressure. However, the reader should note that in the gasdynamic laser, the nonequilibrium properties of the nozzle expansion are dependent on  $p$ . Hence, eq. (20) is implicitly dependent on  $p$  through the dependence of  $N_1$  and  $N_2$  on  $p$ .

For  $\text{CO}_2$  lasers,  $\lambda = 10.6 \mu$  and  $\tau_{12} = 5.33$  sec. (see Reference 31). Also, the collision cross-sections for evaluating  $Z$  can be found in Appendix A of Reference 35.

Finally, note that, from eq. (20), small-signal gain is directly proportional to the population inversion, and hence an experimental measurement of  $G_0$  is a measurement of population inversion.

#### 4. $\text{CO}_2$ - $\text{H}_2$ - $\text{H}_2\text{O}$ or He System

The specific energy level diagram for  $\text{CO}_2$  and  $\text{H}_2$  is shown in Figure 7. Note that  $\text{CO}_2$ , being a linear triatomic molecule, has three fundamental vibrational modes: the symmetric stretching mode ( $\nu_1$ ), the doubly-degenerate bending mode ( $\nu_2$ ), and the asymmetric stretching

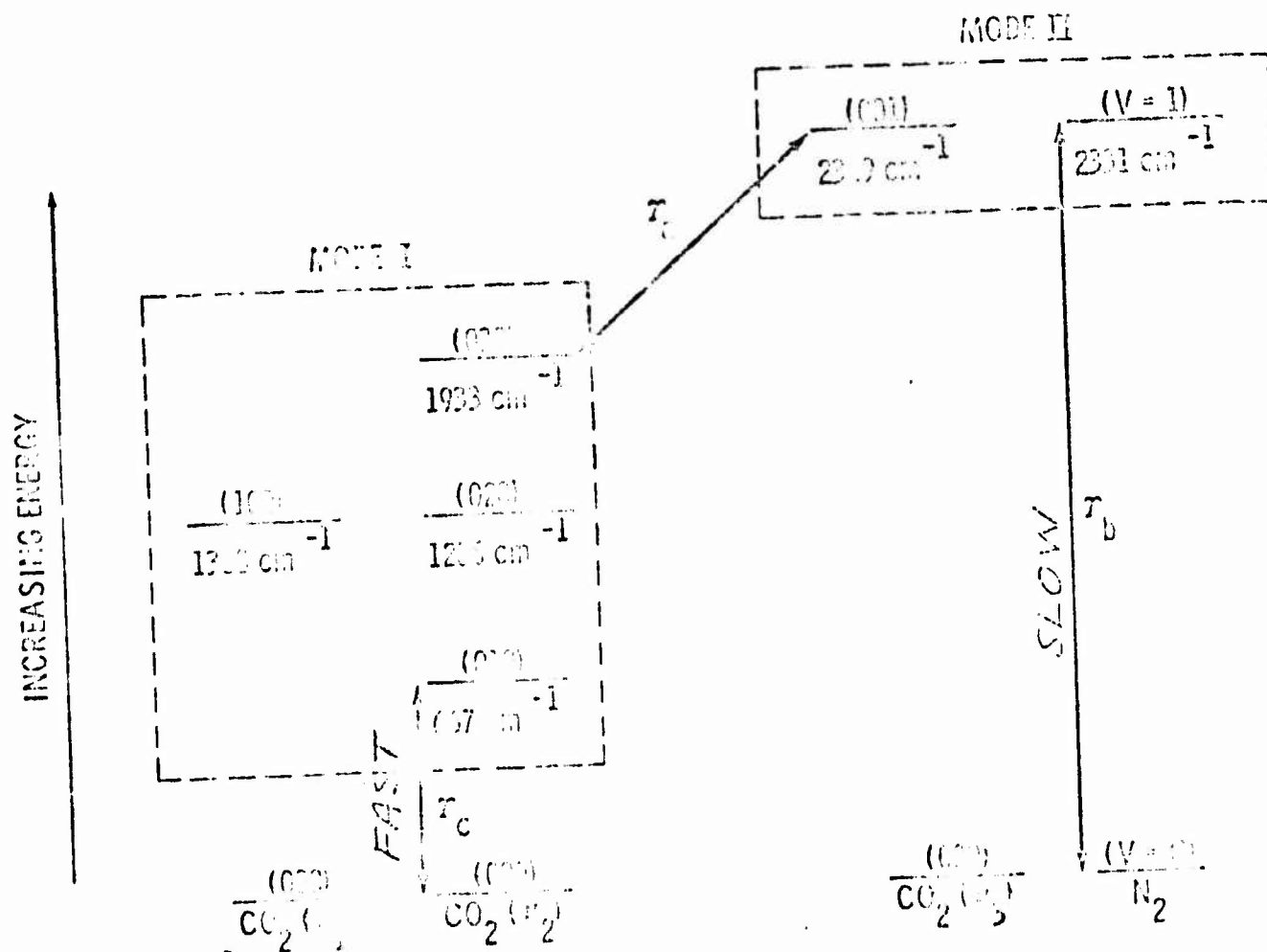


Fig. 7 Schematic of the grouping of energy levels for the vibrational levels

mode ( $v_3$ ). Each of these modes has its own ladder of quantized energy levels, with the triple-quantum number notation ( $v_1, v_2, v_3$ ) to designate each level.  $\text{CO}_2$  is the laser gas, and of particular importance is the (001) upper laser level in the  $v_3$  mode, and the (100) lower laser level in the  $v_1$  mode. This laser transition takes place at a wavelength depending on the particular rotational levels involved. In fact, note that each vibrational level has a series of closely spaced rotational levels superimposed on it, and the actual laser transition takes place between two distinct vibration-rotation levels. These levels are shown schematically in Figure 3, where J denotes the rotational quantum number. A relative transition that results in  $\Delta J = -1$  is a member of the "P Branch", and several of the possible  $\text{CO}_2$  laser transitions (P(20), P(16), P(12)) are shown in Figure 3. If the gas translational temperature is near room temperature, and the laser cavity is properly tuned, the P(20) transition is generally observed.

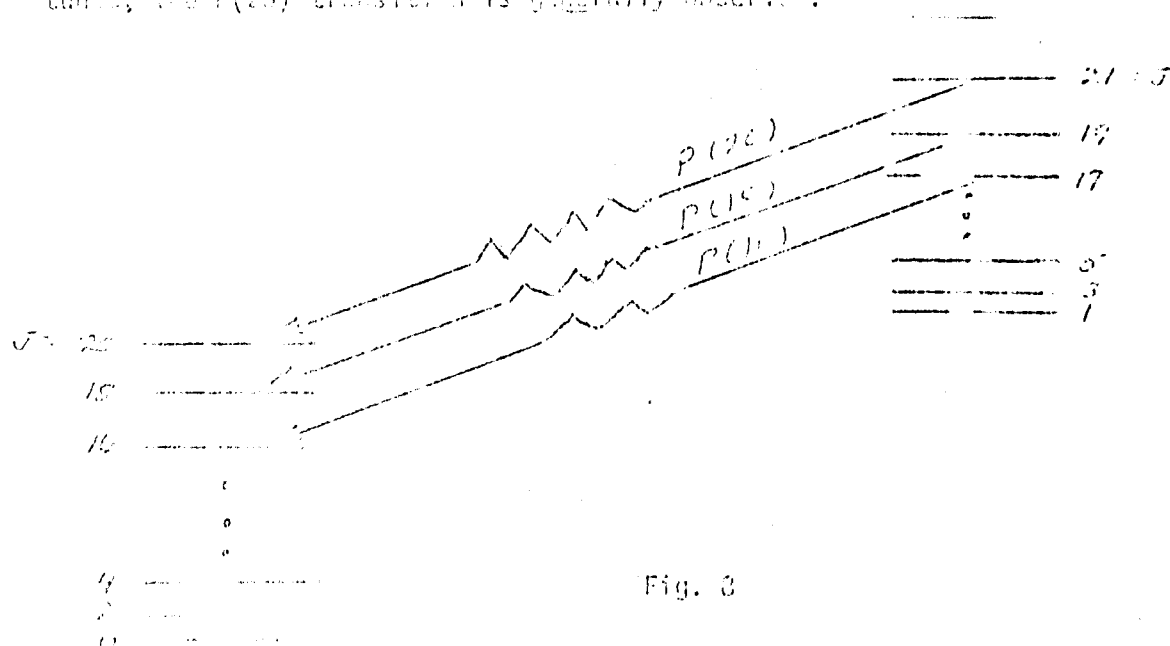


Fig. 3

Returning to Figure 7, note that the  $v_1$  and  $v_2$  modes are grouped together in a box called Mode I, and the  $v_3$  mode and  $\Pi_2$  are grouped into another box called Mode II. This is done to illustrate the net effect of all the complex vibrational energy exchanges taking place due to molecular collisions. The details of this system will be discussed in Section C. However, at this point it is sufficient to point out that the  $\Pi_2$  vibrational energy relaxes very slowly under a sudden change in temperature. In fact, pure  $\Pi_2$  has the longest relaxation time of any diatomic molecule known to the author. Since the  $v = 1$  level of  $\Pi_2$  is very close to the  $\text{CO}_2$  (001) level, then the (001) level also relaxes slowly. On the other hand, the  $v_1$  and  $v_2$  modes (hence the (100) level) equilibrate very rapidly with changes in temperature.

Now we can see in a qualitative sense how the inversion occurs in a supersonic expansion. In the reservoir, we have a hot, vibrationally excited mixture of  $\text{CO}_2$ - $\Pi_2$ - $\text{D}_2$  or He. Molecules are populating the higher lying energy levels, but since the gas is in thermal equilibrium in the reservoir, there are fewer molecules in (001) than there are in (100). When the gas expands through the supersonic nozzle, the temperature drops drastically. In the process, Mode II relaxes slowly, whereas Mode I relaxes rapidly. Molecules slowly drop out of the (001) level, and rapidly drop out of the (100) level. In other words, the population of the (001) level,  $N_{001}$ , tends to "hang up", or "freeze", whereas the population of the (100) level is rapidly depleted due to its fast equilibration with the cool gas. The net result can be a population inversion, i.e.,  $N_{001} > N_{100}$ . A major role of  $\text{D}_2$  or He in this scheme, as we understand it at present, is to speed up the equilibration of

Mode I, hence increasing the population inversion. The over-all, complex vibrational relaxation mechanism will be addressed in more detail in Section C.

### C. CALCULATION OF GASDYNAMIC LASER PERFORMANCE

#### 1. Analysis

In this section, we now discuss the details of calculating gasdynamic laser gain and power. An accurate prediction of the population inversion in an expanding gas encompasses an accurate solution of the nonequilibrium, gas dynamic flow through a convergent-divergent nozzle. Previous numerical solutions of high-temperature, quasi-one-dimensional nonequilibrium nozzle flows where vibrational and chemical nonequilibrium conditions prevail both upstream and downstream of the throat have been obtained with some effort by means of a number of independent, steady-flow analyses<sup>33</sup>. On the other hand, a useful, alternative approach has recently been presented in References 34 and 35, namely, a time-dependent technique which entails the finite-difference solution of the unsteady, quasi-one-dimensional conservation equations in steps of time, starting from assumed initial distributions of the flow-field variables throughout the nozzle. The steady-state nonequilibrium nozzle flow is approached at large times. The main virtue of the time-dependent solution is its simplicity; the governing equations are solved by means of a simple, explicit, finite-difference scheme. no additional mathematical methods are necessary to treat special contingencies that can arise in the analysis of nonequilibrium nozzle flows, no



difficulties are encountered in starting the nonequilibrium flow from equilibrium reservoir conditions, very large spacings can be taken between grid points along the nozzle, and the unknown critical mass flow is automatically approached at large times. As a result, no problems are encountered in the throat region with the saddle-point singularity which plagues the steady-flow formulation.

The discussion that follows is patterned after the technique described in Reference 8. Consider the grid point system shown schematically in Figure 9 for a nozzle of specified shape,  $A = A(x)$ , where  $A$  is the cross-sectional area. There are two sets of equally spaced grid points; one set involves relatively fine spacing from the reservoir to slightly downstream of the throat in order to enhance numerical accuracy in the flow region where nonequilibrium phenomena develop at a fast rate, and the second set involves coarse spacing further downstream where nonequilibrium phenomena are usually progressing at a slow rate. This grid network differs from that of Reference 34, which considered equally spaced grid points throughout the nozzle. In the present results 15 and 5 spaces were employed for the fine and coarse grids, respectively, i.e. a total of 21 grid points were employed throughout the nozzle.

The analysis begins by assuming initial values for the density  $\rho$ , velocity  $u$ , temperature  $T$ , and the nonequilibrium quantities  $q_i$  at all grid points throughout the nozzle. The precise quantities represented by  $q_i$  will be discussed later. Equilibrium reservoir conditions for  $\rho$ ,  $T$  and  $q_i$  are assumed at the first grid point and held fixed, invariant with time. At each internal grid point, spatial derivatives are then computed from central finite-differences,

$$\frac{\partial g}{\partial x} = \frac{g(x+\Delta x) - g(x-\Delta x)}{2\Delta x} \quad (21)$$

$$\frac{\partial^2 g}{\partial x^2} = \frac{g(x+\Delta x) - 2g(x) + g(x-\Delta x)}{(\Delta x)^2} \quad (22)$$

where  $g$  stands for  $\rho$ ,  $u$ ,  $T$  and  $q_i$ . The numbers for the  $x$ -derivatives obtained from equations (21) and (22) are then substituted into the quasi-one-dimensional, unsteady, conservation equations

$$\text{Continuity} \quad \frac{\partial \rho}{\partial t} = -\frac{1}{A} \frac{\partial (\rho u A)}{\partial x} \quad (23)$$

$$\text{Momentum} \quad \frac{\partial u}{\partial t} = -\left[ \frac{1}{\rho} \frac{\partial \rho}{\partial x} + u \frac{\partial u}{\partial x} \right] \quad (24)$$

$$\text{Energy} \quad \frac{\partial e}{\partial t} = -\left[ \frac{\rho}{\rho} \left( \frac{\partial u}{\partial x} + u \frac{\partial \ln T}{\partial x} \right) + u \frac{\partial e}{\partial x} \right] \quad (25)$$

$$\text{Rate} \quad \frac{\partial q_i}{\partial t} = w_i(\rho, T, q_i) - u \frac{\partial q_i}{\partial x} \quad (26)$$

$$\text{State} \quad p = \rho R T \quad (27)$$

where  $q_i$  can be the population or energy per unit mass associated with a given vibrational energy level (or grouping of levels), and  $w_i$  is the net internal rate of production of  $q_i$  due to detailed vibration-vibration and vibration-translation collisions within the gas mixture.

Values of the time derivatives,  $\frac{\partial g}{\partial t}$ , are directly obtained from equations (23) through (27), and these numbers are subsequently inserted into an expression containing the first three terms of a Taylor's series expansion in time, i.e.,

$$g(t+\Delta t) = g(t) + \left( \frac{\partial g}{\partial t} \right)_t \Delta t + \left( \frac{\partial^2 g}{\partial t^2} \right)_t \frac{\Delta t^2}{2} \quad (28)$$

Equation (28) allows the direct computation of all flow-field

variables at all internal grid points at time  $(t+\Delta t)$  from the known flow-field variables at time  $t$ . Values for  $g(t)$  are known; as previously noted, values for  $(\frac{\partial g}{\partial t})_t$  are obtained from equations (23) through (27). Numbers for  $(\frac{\partial^2 g}{\partial t^2})_t$  can be obtained by differentiation of equations (23) through (26) with respect to  $t$ ; however, such an operation introduces mixed derivatives,  $\frac{\partial^2 g}{\partial x \partial t}$ , values for which are simply obtained by differentiation of equations (23) through (26) with respect to  $x$ . Hence, starting from assumed initial values for the flow-field variables throughout the nozzle, new values of the flow-field distributions are computed in steps of time from equation (28), continuing for many time steps until the steady-state solution is approached at large times (where  $\frac{\partial g}{\partial t}$  and  $\frac{\partial^2 g}{\partial t^2}$  both approach zero). For the present study, this steady-state solution is the desired result.

The most recent calculations using the above approach employ a slightly modified technique discussed in References 32 and 35. The modification consists of using

$$g(t+\Delta t) = g(t) + \left( \frac{\partial g}{\partial t} \right)_{\text{ave}} \Delta t \quad (29)$$

in lieu of eq. (28). Here, the time derivative is not evaluated at time  $t$  as in eq. (28); rather, an average value between  $t$  and  $(t+\Delta t)$  is utilized. This average value is obtained from the general method of MacCormack, who has shown that the general scheme is of second-order accuracy. The results obtained using either approach yield the same results<sup>35</sup>. However, by using eq. (29) with MacCormack's

finite-difference scheme, a considerable simplification in computer programming and reductions in execution time are obtained. See Ref. 35 for more details.

The value of  $\Delta t$  employed in equations (28) or (29) must satisfy two stability criteria<sup>34</sup>

$$\Delta t \leq \Delta x / (u+a) \quad (30)$$

where  $a$  is the local frozen speed of sound, and

$$\Delta t < \tau \quad (31)$$

where  $\tau$  is the characteristic relaxation time for the fastest finite-rate molecular relaxation process occurring within the mixture. Equation (30) is the Courant-Friedrichs-Levy<sup>37</sup> stability criterion, which in physical terms states that  $\Delta t$  must be no greater than the time required for a sound wave to propagate from one grid point to the next, and equation (31) states that  $\Delta t$  must be no greater than the characteristic time of the finite-rate molecular energy exchange processes occurring within the flowing gas. This latter stability criterion is plausible on physical grounds, and has been demonstrated empirically in Reference 34.

Because central finite-differences are employed, equations (21) through (28) can be applied to the internal points only. For each time step, values for  $\rho$ ,  $u$ ,  $T$  and  $q_i$  at the last grid point (nozzle exit) and  $u$  at the first grid point (nozzle inlet) are obtained by extrapolation, as discussed in Reference 34. Also, for the actual numerical computations, equations (21) through (30) are rewritten

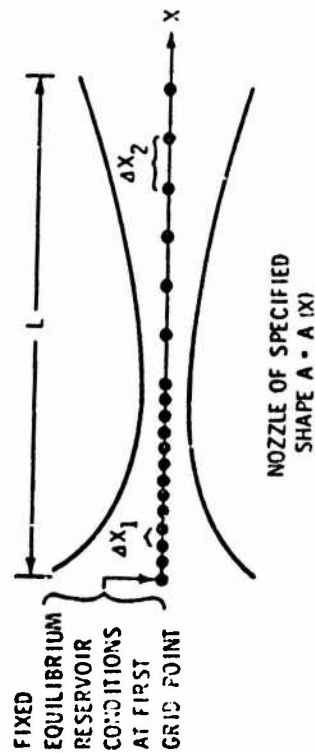


Fig. 9 SKETCH OF THE COORDINATE SYSTEM AND GRID POINTS

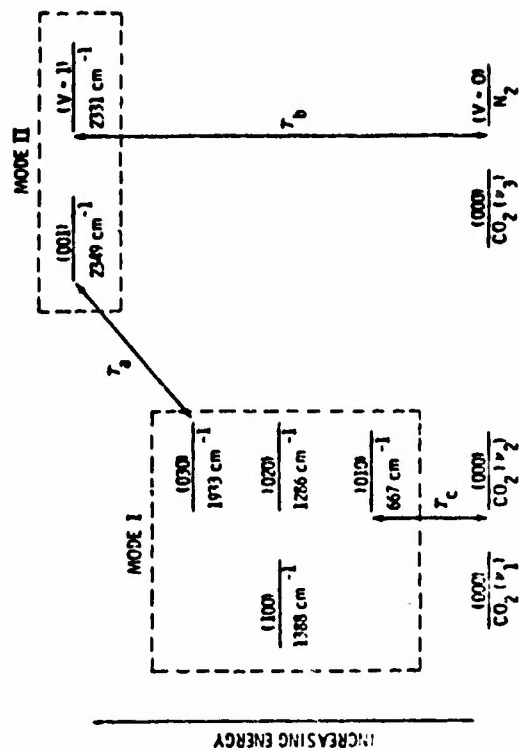


Fig. 10 SCHEMATIC OF THE GROUPING OF ENERGY LEVELS FOR THE VIBRATIONAL MODEL

in nondimensional form (Reference 34) so that the magnitudes of all variables would be approximately the same.

## 2. Vibrational Model

The vibrational model assumed in the present study is a reasonable approximation for the many detailed translation-vibration and vibration-vibration molecular collisional energy exchanges which can occur in  $\text{CO}_2\text{-N}_2\text{-H}_2\text{O}$  or  $\text{CO}_2\text{-N}_2\text{-He}$  mixtures. Figure 10 shows a schematic diagram of the major participating vibrational energy levels for  $\text{CO}_2$  and  $\text{N}_2$  at the temperature considered in the present investigation (from 300 to 1500°K). In 1969, Taylor and Bitterman<sup>7,38</sup> made a thorough study and compilation of the collisional transition probabilities for this system. Their results show an extremely fast, resonant, vibrational energy exchange between the  $v = 1$  level of  $\text{N}_2$  and the (001) level of  $\text{CO}_2$ , as well as a very fast exchange between the (100) and (020) levels of  $\text{CO}_2$  due to Fermi resonance. In addition, vibrational energy is rapidly transferred among the lower excited levels of the degenerate mode  $v_2$  in  $\text{CO}_2$  due to the nearly equal spacing of these levels. Hence, these fast transitions appear to justify a vibrational model which groups the participating levels into two "modes" (Modes I and II in Figure 10) which are assumed in equilibrium within themselves, but not with each other.

More recent kinetic data obtained since 1969 are summarized in References 25 and 26. In fact, Reference 25 is reproduced in its entirety as Appendices A and B in these Notes. The reader should consult Appendices A and B for up-to-date kinetic rates before attempting

any calculations of his own.

In the following discussion of the vibrational model, a CO<sub>2</sub>-N<sub>2</sub>-H<sub>2</sub>O mixture will be assumed for purposes of illustration. CO<sub>2</sub>-N<sub>2</sub>-He is handled in the same manner, with H<sub>2</sub>O replaced by He in all subsequent equations.

The net vibrational energies per unit mass contained within each "mode",  $(e_{vib})_I$  and  $(e_{vib})_{II}$ , are chosen as the dependent non-equilibrium variables; hence, equation (26) represents two rate equations with  $q_i = (e_{vib})_I$  and  $(e_{vib})_{II}$  respectively. The relaxation of these energies is assumed to be described by the simple-harmonic oscillator relaxation equations:

$$\dot{w}_1 = \frac{d(e_{vib})_I}{dt} = \frac{1}{\tau_I} [(e_{vib})_I^{eq} - (e_{vib})_I] \quad (32a)$$

when  $q_i = (e_{vib})_I$ , and

$$\dot{w}_2 = \frac{d(e_{vib})_{II}}{dt} = \frac{1}{\tau_{II}} [(e_{vib})_{II}^{eq} - (e_{vib})_{II}] \quad (32b)$$

when  $q_i = (e_{vib})_{II}$ . In equations (32a) and (32b),  $(e_{vib})_I^{eq}$  and  $(e_{vib})_{II}^{eq}$  are the equilibrium vibrational energies that would be contained in Modes I and II respectively at the local gas translational temperature T, and  $\tau_I$  and  $\tau_{II}$  are the characteristic relaxation times for Modes I and II respectively.  $\tau_I$  and  $\tau_{II}$  are averages which characterize the net rate of energy transfer into and out of Modes I and II; this energy transfer is assumed to be governed by the major transitions (heavy arrows in Figure 10) which are identified with the relaxation times  $\tau_a$ ,  $\tau_b$ ,  $\tau_c$ . These relaxation times are themselves averages

of the detailed  $\text{CO}_2\text{-CO}_2$ ,  $\text{CO}_2\text{-N}_2$ ,  $\text{CO}_2\text{-H}_2\text{O}$ ,  $\text{N}_2\text{-N}_2$  and  $\text{N}_2\text{-H}_2\text{O}$  collisions; such averages for a mixture of gases are obtained from the "parallel resistance" mixture rule:

$$\frac{1}{\tau_a} = \frac{X_{\text{CO}_2}}{(\tau_a)_{\text{CO}_2\text{-CO}_2}} + \frac{X_{\text{N}_2}}{(\tau_a)_{\text{CO}_2\text{-N}_2}} + \frac{X_{\text{H}_2\text{O}}}{(\tau_a)_{\text{CO}_2\text{-H}_2\text{O}}} \quad (33a)$$

$$\frac{1}{\tau_b} = \frac{X_{\text{CO}_2}}{(\tau_b)_{\text{N}_2\text{-CO}_2}} + \frac{X_{\text{N}_2}}{(\tau_b)_{\text{N}_2\text{-N}_2}} + \frac{X_{\text{H}_2\text{O}}}{(\tau_b)_{\text{N}_2\text{-H}_2\text{O}}} \quad (33b)$$

$$\frac{1}{\tau_c} = \frac{X_{\text{CO}_2}}{(\tau_c)_{\text{CO}_2\text{-CO}_2}} + \frac{X_{\text{N}_2}}{(\tau_c)_{\text{CO}_2\text{-N}_2}} + \frac{X_{\text{H}_2\text{O}}}{(\tau_c)_{\text{CO}_2\text{-H}_2\text{O}}} \quad (33c)$$

$x_i$  denotes the mole fraction of chemical species  $i$ . For the present results, values for the denominators of the terms on the r.h.s. of equations (33a, b and c) are obtained directly from Reference 38.

(However, the reader should consult Appendices A and B of the present notes for more recent kinetic rates.) In turn, the average relaxation times for Modes I and II are obtained from

$$\tau_I = \tau_c \quad (34)$$

$$\frac{1}{\tau_{II}} = \left[ \frac{X_{\text{CO}_2}}{\tau_a} + \frac{X_{\text{N}_2}}{\tau_b} \right] \cdot \frac{1}{(X_{\text{CO}_2} + X_{\text{N}_2})} \quad (35)$$

These values are subsequently employed in equations (32).

Parenthetically, the general quantity  $\tau$  can be interpreted as a mean time required for a single particle to make a transition from one state to another state due to collisions with other particles. In turn,  $\tau^{-1}$  can be interpreted as the number of transitions per second



per particle. Hence, on a physical basis, equations (33a, b and c) simply state that the total number of transitions per second per particle due to collisions with all species present in the mixture is the sum of the transitions per second per particle due to collisions with each individual species. Equations (34) and (35) have similar physical interpretations, except now the "transitions" are from one mode to another.

The above model for treating the complex vibrational energy transfer processes is approximate, and its limitations are discussed in Reference 11.

It is sufficient to state here that the model is intended only for the calculation of population inversions in  $\text{CO}_2\text{-H}_2\text{-H}_2\text{O}$  or He mixtures; it is not necessarily valid for other gases, nor can it be used when substantial amounts of radiative energy interact with the gas.

An alternative to the above model is the exact solution of the master relaxation equations for each energy level<sup>39</sup>. However, for many cases of interest, comparisons with experiment (to be discussed) show that such a detailed treatment is not absolutely necessary, and that the present model yields reasonable accuracy.

Referring again to equations (32a) and (32b),  $(e_{\text{vib}})_I$  and  $(e_{\text{vib}})_{II}$  are treated as the dependent nonequilibrium variables. From these energies, different vibrational temperatures,  $(T_{\text{vib}})_I$  and  $(T_{\text{vib}})_{II}$ , are defined from the following equilibrium relations:

$$(e_{vib})_I = c_{CO_2} R_{CO_2} \left\{ \left( \frac{h\nu_1}{k} \right) \left[ e^{h\nu_1/kT_{vibI}} - 1 \right]^{-1} + (2h\nu_2/k) \left[ e^{h\nu_2/kT_{vibI}} - 1 \right]^{-1} \right\} \quad (36a)$$

and

$$(e_{vib})_{II} = c_{CO_2} R_{CO_2} \left( \frac{h\nu_3}{k} \right) \left[ e^{h\nu_3/kT_{vibII}} - 1 \right]^{-1} + c_{N_2} R_{N_2} \left( \frac{h\nu}{k} \right) \left[ e^{h\nu/kT_{vibII}} - 1 \right]^{-1} \quad (36b)$$

In equations (36a and b),  $c_{CO_2}$  and  $R_{CO_2}$  are the mass fraction and specific gas constant respectively for  $CO_2$ ;  $c_{N_2}$  and  $R_{N_2}$  are defined similarly for  $N_2$ ;  $\nu_1$ ,  $\nu_2$  and  $\nu_3$  are the normal vibrational frequencies of the symmetric stretching, the bending, and the asymmetric stretching modes respectively for  $CO_2$ ; and  $\nu$  is the normal vibrational frequency for  $N_2$ . In turn,  $(T_{vib})_I$  and  $(T_{vib})_{II}$  are used to compute populations of energy levels within modes I and II assuming a Boltzmann distribution locally within each mode. For example, the population of the (001) level in  $CO_2$  is obtained from

$$N_{001} = N_{CO_2} e^{-h\nu_3/kT_{vibII}} / Q \quad (37)$$

where

$$Q = \left[ 1 - e^{-h\nu_1/kT_{vibI}} \right]^{-1} \left[ 1 - e^{-h\nu_2/kT_{vibI}} \right]^{-2} \left[ 1 - e^{-h\nu_3/kT_{vibII}} \right]^{-1} \quad (38)$$

and the population of the (100) level in  $CO_2$  is obtained from

$$N_{100} = N_{CO_2} e^{-h\nu / k T_{vib I}} / Q \quad (39)$$

In the above formulation, the role of  $H_2O$  or He as a catalyst enters the analysis through its presence in equations (33a, b and c).

As a final note with regard to the present analysis,  $(e_{vib})_I$  and  $(e_{vib})_{II}$  are inherent parts of the time-dependent nonequilibrium nozzle flow solution, and are computed at each time step during the transient approach to steady-state conditions. Then, after the steady-state is achieved, the vibrational temperatures and populations are computed from equations (36) through (39).

### 3. Results

The numerical nature of the time-dependent, vibrational nonequilibrium nozzle solution is clearly shown in Figure 11, which illustrates the shape of the  $(e_{vib})_{II}$  distribution through a wedge nozzle at several times during its approach to the steady state. In Figure 11,  $R$  is the specific gas constant for the mixture. The dotted line shows the assumed initial distribution at  $t = 0$ , the solid lines show distributions after 400, 800 and 1000 time steps, and the solid dots show the final, steady-state, nonequilibrium distribution obtained after approximately 3000 time steps. Similar transient variations and the subsequent approach to the steady-state occur for all other flow variables throughout the nozzle.

The final, steady-state  $(e_{vib})_{II}$  distribution shown in Figure 11, taken in conjunction with the simultaneous steady-state

$(e_{\text{vib}})_I$  distribution, leads to the steady-flow results shown in Figures 12 through 14. In Figure 12, the two vibrational temperature distributions are compared with the translational temperature distribution. Note that Mode II relaxes much slower than Mode I, and that both Modes I and II are not in equilibrium with the local translational temperature except near the nozzle reservoir. Also, note that  $(T_{\text{vib}})_{II}$  begins to diverge from  $T$  in the subsonic section of the nozzle, with  $[(T_{\text{vib}})_{II} - T] = 120^\circ\text{K}$  at the throat. Hence, nonequilibrium effects upstream of the throat are noticeable. In Figure 13, the populations  $N_{001}$  and  $N_{100}$  of the (001) and (100) levels respectively in  $\text{CO}_2$  are shown as functions of distance along the wedge nozzle. At approximately 0.26 cm downstream of the throat, the populations of the (001) and (100) levels are equal, and a substantial population inversion develops further downstream. This population inversion is shown in Figure 14 in terms of  $(N_{001} - N_{100})/N_{\text{CO}_2}$  where  $N_{\text{CO}_2}$  is the local number density of  $\text{CO}_2$  particles. If the nozzle exhausts into a constant area duct as shown in Figure 14, the inversion will continue to increase beyond the nozzle exit until Mode I equilibrates with  $T$ , beyond which the inversion will slowly decrease due to the moderate deactivation of Mode II. As emphasized in References 7 and 38, the equilibration of Mode I with  $T$  is enhanced by the presence of  $\text{H}_2\text{O}$  in the mixture.

#### 4. Comparison with Basov

Basov et al.<sup>6</sup> have published results for population inversions created in a supersonic expansion of a  $\text{CO}_2\text{-N}_2$  mixture through a hyperbolic

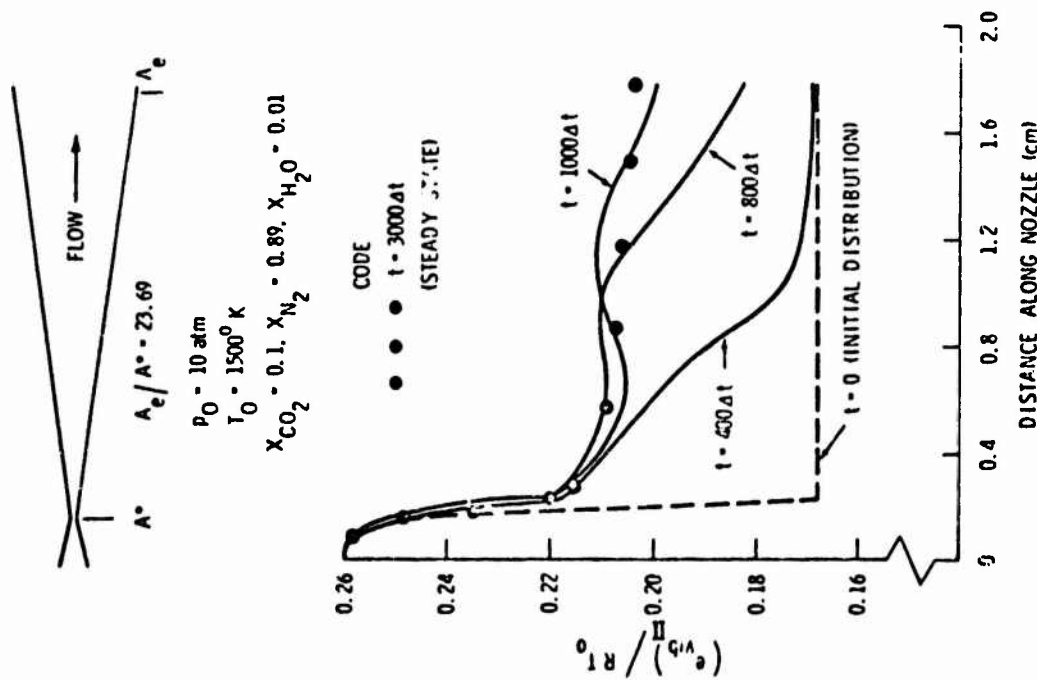


Fig. 11 TRANSIENT AND FINAL STEADY-STATE MODE II VIBRATIONAL ENERGY ALONG NOZZLE

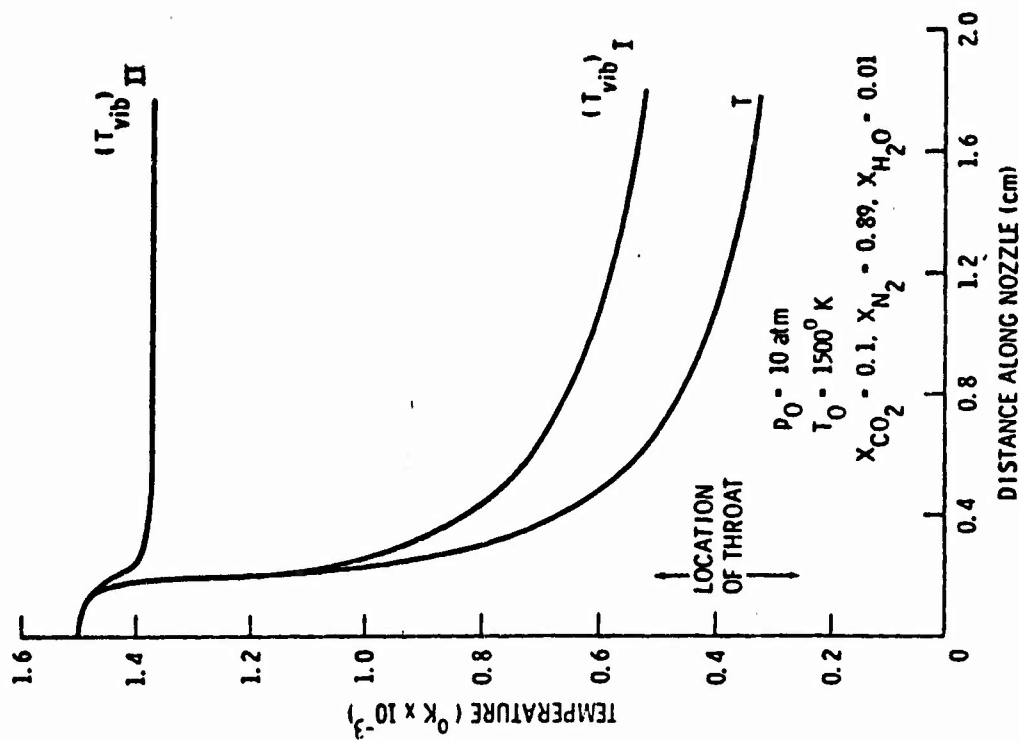


Fig. 12 COMPARISON OF THE STEADY-STATE VIBRATIONAL AND TRANSLATIONAL TEMPERATURE DISTRIBUTIONS THROUGHOUT NOZZLE

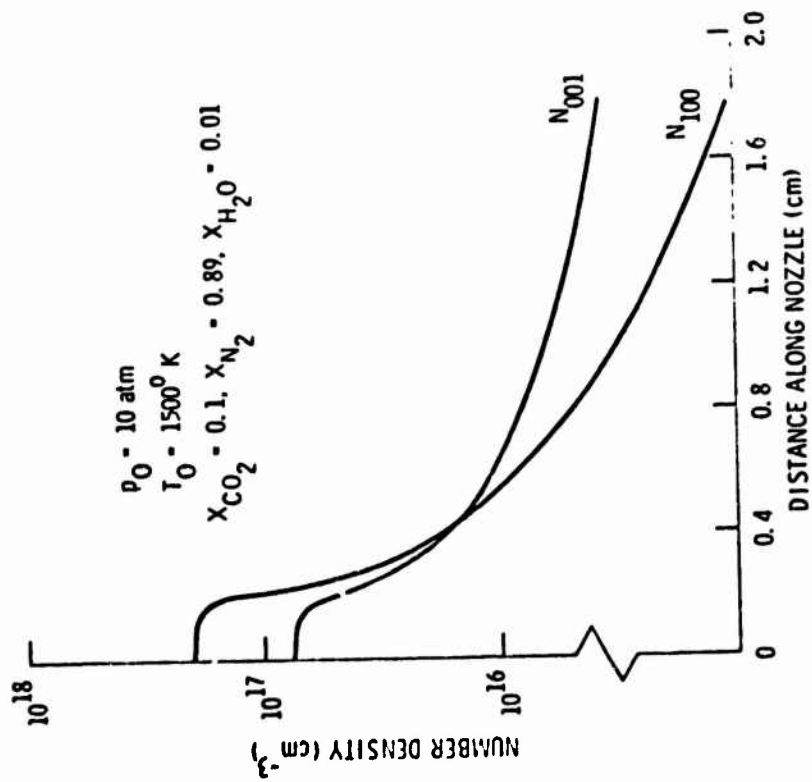


Fig. 13 STEADY-STATE POPULATION DISTRIBUTIONS THROUGHOUT NOZZLE

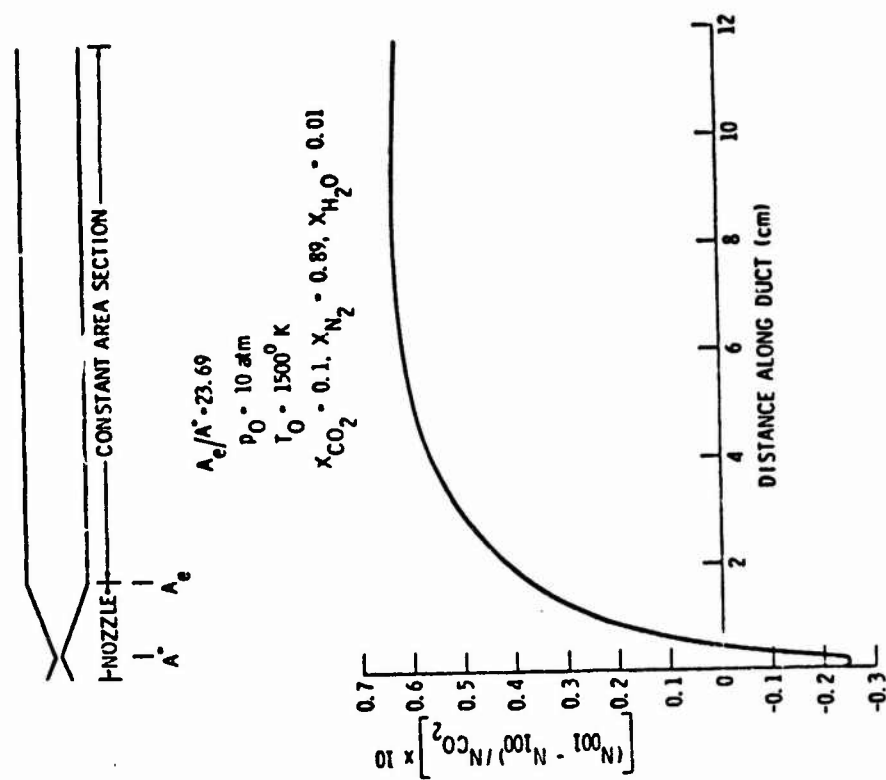


Fig. 14 STEADY-STATE DISTRIBUTION OF POPULATION INVERSION THROUGHOUT NOZZLE

nozzle; in contrast to the present results shown in Figures 11 through 14, Basov did not include the effect of  $H_2O$  on the population inversions. Also in contrast to the present analysis, Basov assumed equilibrium conditions from the reservoir to the throat. In order to provide a comparison with the results of Reference<sup>6</sup>, results are obtained with the present time-dependent analysis for a nozzle shape,  $p_0$ ,  $T_0$  and mixture ratio identical to those of Reference<sup>6</sup>. Figures 15 and 16 show the resulting comparison; Figure 15 illustrates the populations  $N_{100}$  and  $N_{001}$  as a function of distance through the nozzle, and Figure 16 shows the population inversion distribution throughout the nozzle.  $N_0$  is the total reservoir number density for the gas mixture. A study of Figure 15 shows that Basov predicts a slower relaxation of the (001) level and a faster relaxation of the (100) level in comparison to the present results. Consequently, as seen in Figure 16, Basov's results show a population inversion, whereas for the given conditions the present results predict no population inversion. The present results embody detailed information on transition probabilities reported in Reference 38, whereas Basov used somewhat cruder information for transition probabilities. A comparison of these two sets of transition data show approximate agreement for the collision probability for deactivation of the (001) level; on the other hand, Basov used probabilities for deactivation of the (010) level (hence the (100) level, which is closely coupled by fast resonant exchanges) which are more than an order of magnitude larger than those presented in Reference 38. Consequently, the differences

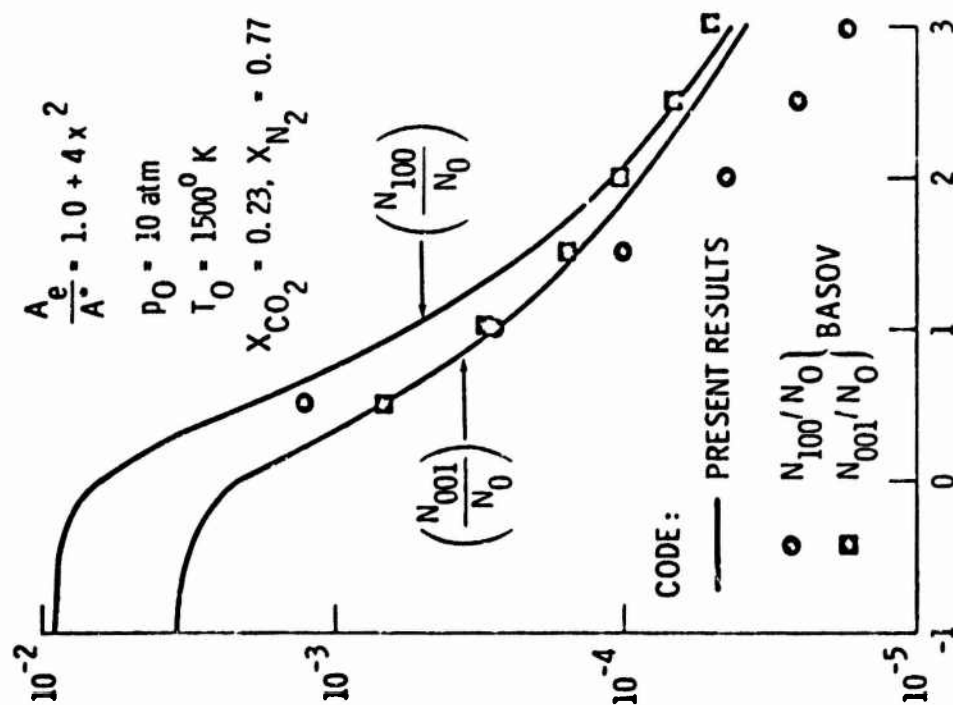


Fig. 15 STEADY-STATE POPULATION DISTRIBUTIONS THROUGHOUT NOZZLE; COMPARISON OF PRESENT RESULTS WITH THOSE OF BASOV ET AL

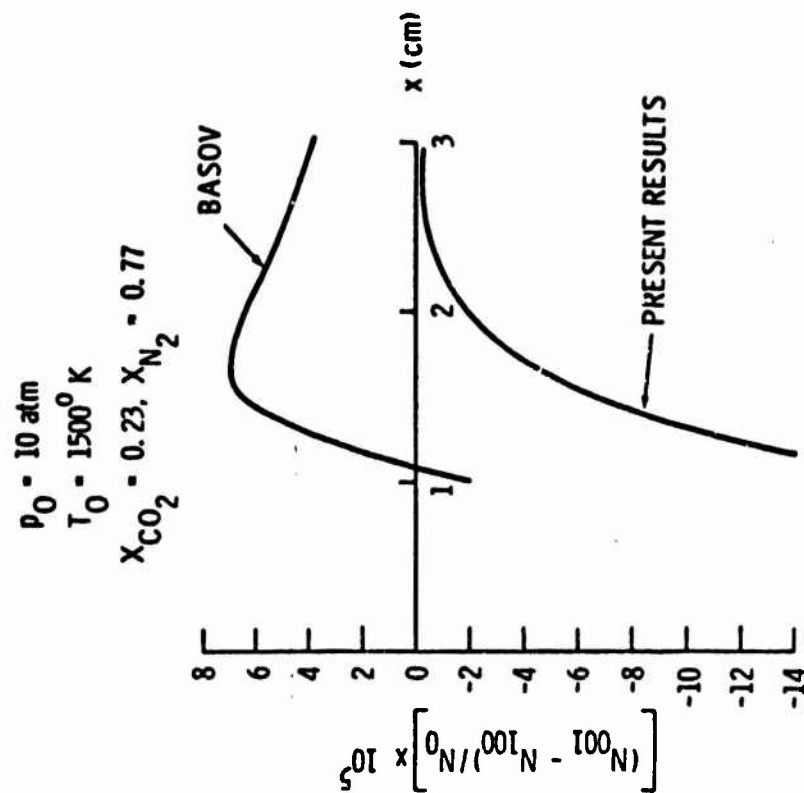


Fig. 16 STEADY-STATE DISTRIBUTION OF POPULATION INVERSION; COMPARISON OF PRESENT RESULTS WITH THOSE OF BASOV ET AL



shown in Figures 15 and 16 can be attributed mainly to differences in relaxation times used for the two analyses. Taylor and Bitterman's thorough compilation of transition probabilities (Refs. 7 and 38) is believed to contain the most reliable data currently available in the literature. These data have been very recently up-dated by Anderson in References 25 and 26. (See Appendices A and B of the present Notes). Also, these results clearly demonstrate that population inversions in  $\text{CO}_2\text{-N}_2$  mixtures without a catalyst are difficult to obtain. Indeed, in subsequent sections of these notes, we will see that the presence of  $\text{H}_2\text{O}$  or He is vitally necessary for the attainment of reasonable population inversions.

As a point of interest, Basov's assumption (Ref. 6) of equilibrium conditions at the nozzle throat is reasonable for the nozzle shape he considered; for this nozzle, the subsonic approach to the throat is relatively long and smooth, thus enhancing equilibrium conditions. In fact, the present results, which include nonequilibrium conditions upstream of the throat, indicate that  $[(T_{\text{vib}})_{\text{II}} - T]$  is  $28^\circ\text{K}$  at the throat for Basov's conditions. This should be compared with the  $120^\circ\text{K}$  difference obtained for the shorter nozzle considered in Figure 11, where nonequilibrium effects upstream of the throat are considerable.

##### 5. Coupled and Uncoupled Flows

With regard to calculations of population inversions in an expanding nozzle flow, there has been some question regarding the error induced by uncoupling the gas dynamic flow field from the vibrational relaxation phenomena. For example, the calculation of

population inversions would be greatly simplified if the pressure, temperature and velocity distributions were obtained from a calculation of frozen or equilibrium nozzle flows, and then used to solve independently the vibrational rate equations. The flow variable most severely affected by these uncoupled solutions is translational (static) temperature. Since the relaxation rates depend exponentially on  $T$ , and because  $H_{100}$  tries to equilibrate with  $T$  in the supersonic stream, the theoretical population inversions obtained from such uncoupled solutions may contain an inordinate error.

In order to examine this question, a numerical experiment is performed using the present time-dependent analysis to compute population inversions for the following cases: (1) Coupled, where the finite-rate, vibrational energy relaxation is fully included in the gas dynamic energy equation, (2) uncoupled (equilibrium), where  $p$ ,  $T$  and  $u$  are obtained from an expansion assuming infinite-rate, vibrational equilibrium, and (3) uncoupled (frozen), where  $p$ ,  $T$  and  $u$  are obtained from an expansion assuming a zero vibrational rate, i.e., frozen flow. In case (3), two sets of results are obtained, where the ratio of specific heats  $\gamma$  equals 1.4 and 1.3. The value of 1.4 properly corresponds to a vibrationally frozen expansion of  $CO_2$  and  $H_2$ , whereas the value of 1.3 is of interest only because it is equal to the equilibrium value of the ratio of specific heats for the gas mixture in the reservoir. For all of the above cases, a simple wedge nozzle was assumed, followed by a constant area duct. This geometry and the reservoir conditions are described in Figure 17. Note that this nozzle

has the same area ratio but twice the length of the wedge nozzle previously considered in Figures 11 through 14.

Results from this numerical experiment are shown in Figures 17 through 20. Figure 17 contrasts the translational temperature distributions obtained for the different assumptions of infinite, finite and frozen rates; such a comparison is classical, and is presented in order to help interpret the subsequent results. Also, Figure 17 shows that, for the present conditions, the actual nonequilibrium expansion is closer to equilibrium than frozen. In turn, a comparison of the curves shown in Figure 18 indicates that  $(T_{vib})_I$  is more strongly affected than  $(T_{vib})_{II}$ . Indeed, the upper level appears to be insensitive to the differences in translational temperature between the different cases despite the exponential variation of relaxation time with  $T$ . The reason for the differences in  $(T_{vib})_I$  is the strong tendency of the lower level to equilibrate with  $T$ , which is different for each of the cases.

The differences in  $(T_{vib})_I$  shown in Figure 18 are magnified when  $n_{100}$  is computed, as shown in Figure 19. Also, as expected from the very small differences in  $(T_{vib})_{II}$ , only small differences occur in  $n_{001}$ .

The differences shown in Figure 19 translate into the differences in population inversion shown in Figure 20. Among the simplified, uncoupled cases, Figure 20 illustrates that the  $p, T$  and  $u$  variations obtained from an equilibrium flow calculation provide the closest comparison with the coupled case. However, there is still a noticeable error induced by all the uncoupled cases. With regard to

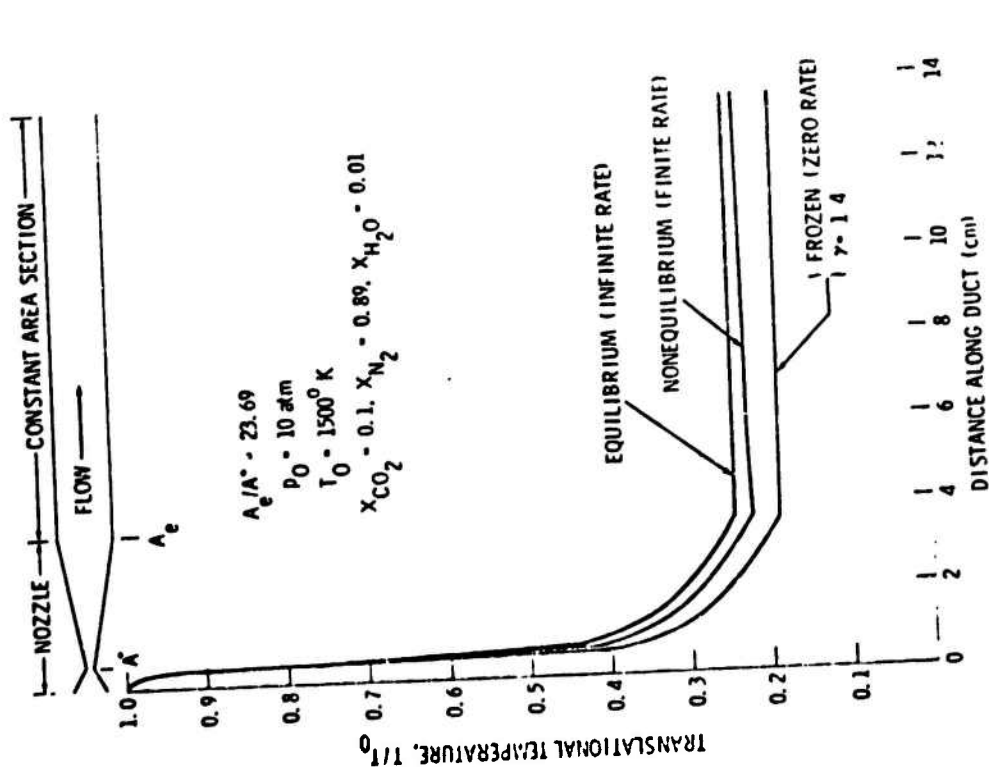


Fig. 17 COMPARISON OF STEADY-STATE TEMPERATURE DISTRIBUTIONS FOR EQUILIBRIUM, FROZEN AND FINITE-RATE NOZZLE FLOW

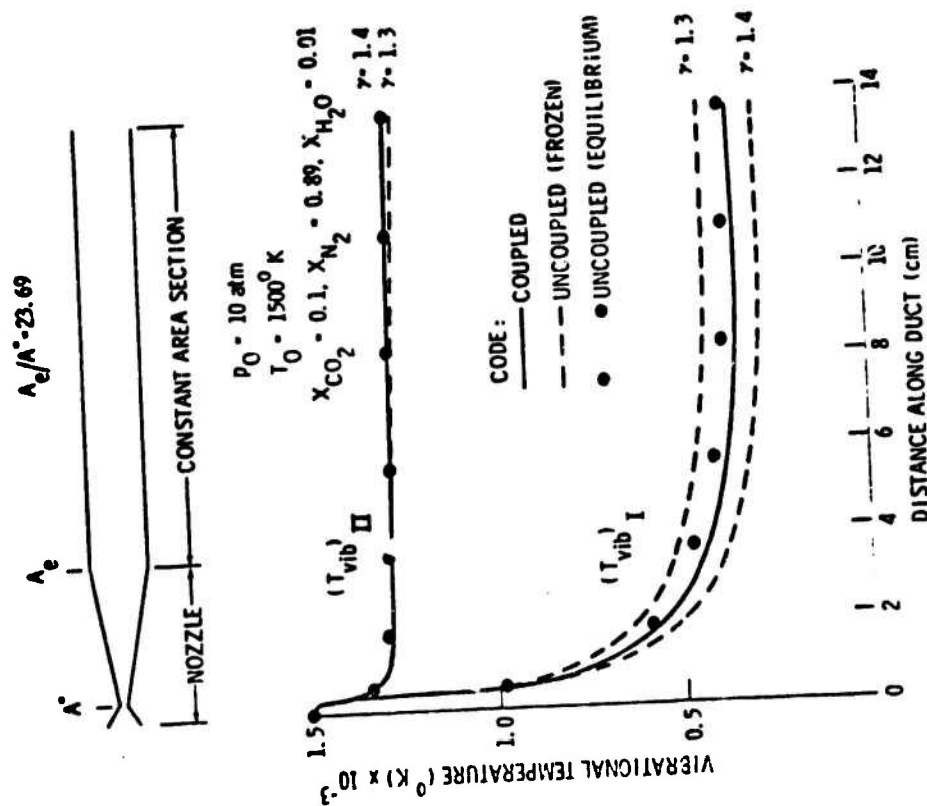


Fig. 18 COMPARISON OF STEADY-STATE VIBRATIONAL TEMPERATURE DISTRIBUTIONS FOR THE COUPLED AND UNCOUPLED CASES

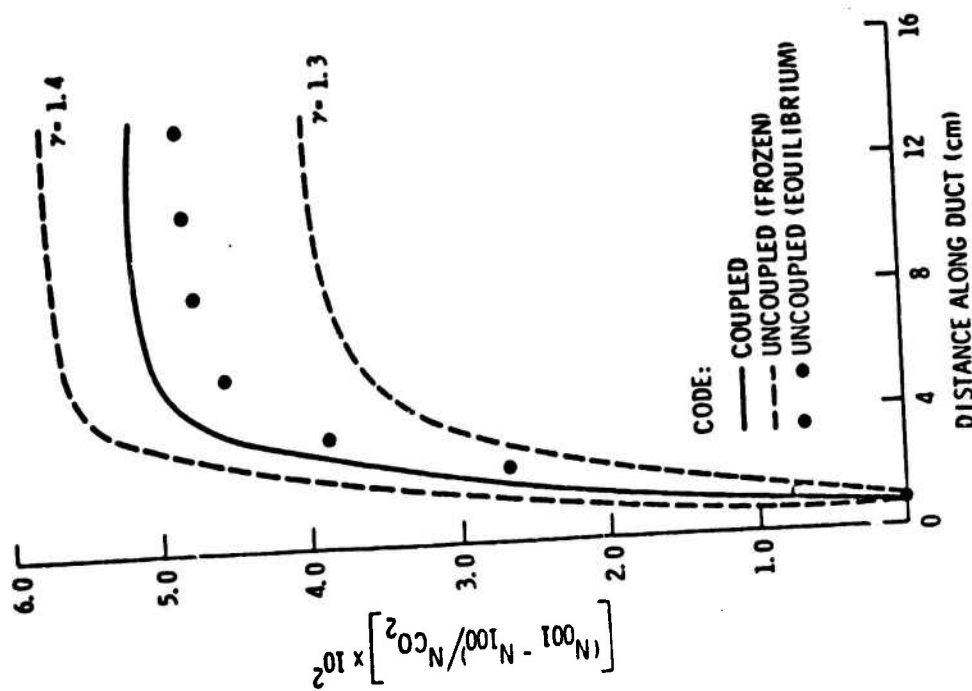


Fig. 20 COMPARISON OF STEADY-STATE POPULATION INVERSIONS FOR THE COUPLED AND UNCOUPLED CASES

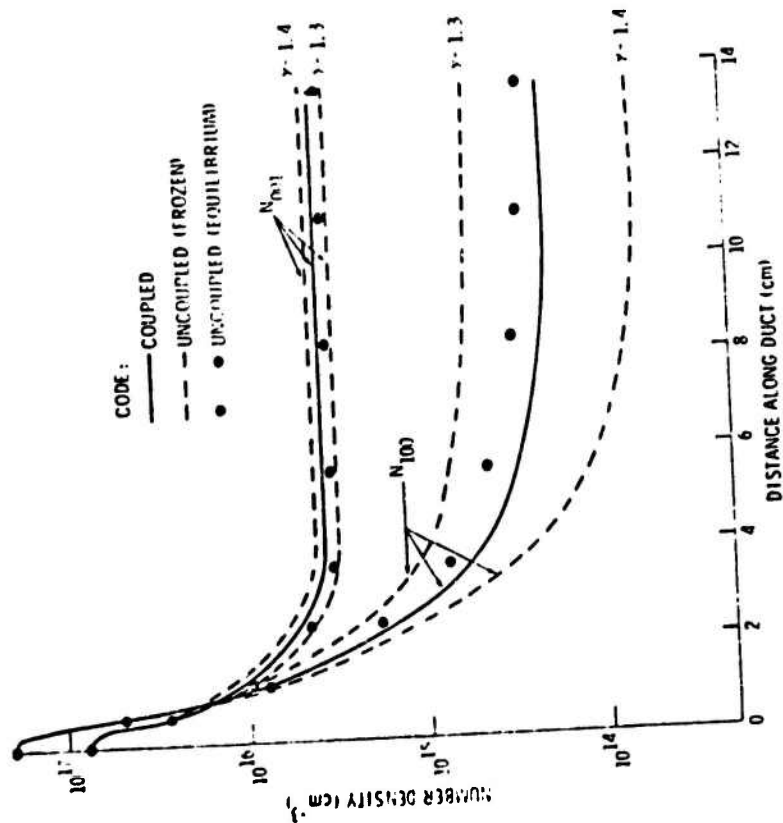


Fig. 19 COMPARISON OF STEADY-STATE NUMBER DENSITY DISTRIBUTIONS FOR THE COUPLED AND UNCOUPLED CASES

the frozen cases. one might be able to simulate the coupled results by "proper" choice of an effective  $\gamma$  between 1.3 and 1.4, however, such a value of  $\gamma$  is not known a priori, and its proper choice would be strictly fortuitous without first knowing the answer.

Reflecting upon the results shown in Figures 17 through 20, the accurate calculation of population inversions in an expanding gas apparently requires an analysis which fully takes into account the coupling between the finite-rate nonequilibrium processes and the gas dynamic flow.

It is interesting to note that, for the same reservoir conditions, the peak population inversion shown in Figure 14 is 23 percent higher than the peak shown in Figure 20 for the coupled case. The larger inversion shown in Figure 14 is due solely to the shorter nozzle length, and is to be expected due to a greater degree of nonequilibrium in the shorter nozzle flow.

#### 6. Recapitulation

The previous sections have described the time-dependent technique for calculating population inversions in an expanding gas, and have given some typical results obtained with an approximate vibrational model. The kinetic rates employed in generating the results shown in Figures 11 through 20 are given in Appendix A of Reference 40, which contains simple correlations of the rates from Taylor and Bitterman<sup>38</sup>. However, these correlations have been improved as discussed in References 25 and 26, and the reader is again urged to consult Appendices A and B of the

present Notes for up-dated kinetic rates.

Another detailed numerical solution for GDL's can be found in Reference 41, where Munjee has incorporated a more detailed kinetic model than used in Reference 8. Munjee's kinetic model is patterned after that of Basov et al<sup>6</sup>; however, unlike Basov, Munjee includes the effect of a catalyst ( $H_2O$  or He) in the master rate equations. Munjee's work serves as the basis for the theoretical results quoted by Christiansen, Tsongas and Buonadonna<sup>13,42</sup>. In addition to these detailed numerical solutions, a useful approximate analysis has been developed by Hoffman and Vlases<sup>27</sup>. Also, recent results using the sudden-freezing approximation have been reported in Reference 28.

#### 7. Power Extraction

In a gasdynamic laser, the energy available for laser power extraction is contained in the vibrational energies of the excited  $N_2$  and  $CO_2(v_3)$  at the exit of the supersonic nozzle; the challenge is to optically extract as much of this available energy as possible before it deactivates and "leaks" into translational and rotational energy due to molecular collisions. Moreover, the extraction process should also produce a good quality, near-diffraction-limited beam. Therefore, the optical design of the laser cavity is of utmost importance. Some considerations dealing with the optical cavity will be discussed in Section III of these Notes, and some of the aerodynamic disturbances which influence cavity design and beam quality will also be treated in

Section III. However, let us now consider power extraction from a purely energy standpoint.

The maximum available laser energy can be calculated as follows. Consider a point in the nozzle of a gasdynamic laser. Using the notation of Reference 8, the translational and rotational temperature at this point is  $T$ , the sum of the vibrational energy contained in the excited  $H_2$  and  $CO_2$  ( $v_3$ ) is  $e_{vib_{II}}$  with an attendant vibrational temperature  $T_{vib_{II}}$ , the sum of the vibrational energy in the  $CO_2(v_1)$  and  $CO_2(v_2)$  modes is  $e_{vib_I}$  with an attendant  $T_{vib_I}$ , and the population densities of the upper and lower laser levels are  $N_{001}$  and  $N_{100}$  respectively. In GDL flows in general,  $T_{vib_{II}} > T_{vib_I} > T$ . When an inversion exists, then by definition  $N_{001} - N_{100} > 0$ . The population densities are given by

$$N_{001} = (N_{CO_2}/Q) e^{-\epsilon_{001}/k T_{vib_{II}}}$$

$$N_{100} = (N_{CO_2}/Q) e^{-\epsilon_{100}/k T_{vib_I}}$$

where  $Q$  is the partition function. We ask the following question: If energy is drained from  $e_{vib_{II}}$ , and  $e_{vib_I}$  is held constant, at what value of  $T_{vib_{II}}$  will the population inversion go to zero? Denote this value of  $T_{vib_{II}}$  by  $(T_{vib_{II}}^0)$ . Then,

$$N_{001} - N_{100} = 0 = (N_{CO_2}/Q) [e^{-\epsilon_{001}/k (T_{vib_{II}}^0)} - e^{-\epsilon_{100}/k T_{vib_I}}]$$



Hence,  $\epsilon_{001}/k(T_{vib_{II}}^{\circ}) = \epsilon_{100}/kT_{vib_I}$

Thus,  $(T_{vib_{II}}^{\circ}) = T_{vib_I} (\epsilon_{001}/\epsilon_{100})$

When  $T_{vib_{II}} > (T_{vib_{II}}^{\circ})$ , an inversion exists and laser power can in principle be extracted. When  $T_{vib_{II}} < (T_{vib_{II}}^{\circ})$ , no inversion is present, and no power can be extracted.

In order to consider the maximum laser energy available, we assume that  $T_{vib_I} = T$ . Then,  $(T_{vib_{II}}^{\circ}) = T(\epsilon_{001}/\epsilon_{100})$ . Using this value of  $(T_{vib_{II}}^{\circ})$ , we define a maximum available laser energy as

$$e_{max} = 0.409 [e_{vib_{II}}(T_{vib_{II}}) - e_{vib_{II}}(T_{vib_{II}}^{\circ})]$$

where the factor 0.409 is the quantum efficiency for the  $CO_2$  laser transition at  $10.6\mu$ .

The quantity  $e_{max}$  is a convenient index to gage the amount of power that might be extracted from a gasdynamic laser. However, in reality the actual power extraction is usually less than  $e_{max}$  due to losses in the laser cavity. Also, all values of  $e_{max}$  given in the present Notes are local values at the nozzle exit, where  $T_{vib_{II}}$  is obtained from the coupled analysis of Reference 8. Therefore, the present values of  $e_{max}$  account for the kinetic deactivation losses in the nozzle. This is in contrast to previous simpler but less realistic definitions of maximum available power<sup>1</sup>, which have been based strictly on the vibrational energy in the reservoir.

Emphasis is again made that  $e_{\max}$  is simply a convenient index that represents an upper limit, and that the actual power extracted may be quite different. An accurate calculation of power extraction must combine a detailed numerical solution of the non-equilibrium supersonic flow in the cavity coupled with a point-by-point numerical integration of the radiative transfer equation

$$dI_r/I_r = G dy$$

in a direction normal to the flow. Here,  $G$  is the actual gain (proportional to the actual population inversion) which takes into account the local depopulation of the  $H_2$  and  $CO_2$  ( $v_3$ ) levels, and the population of the  $CO_2$  ( $v_1$ ) levels due to interaction with the laser radiation.  $G$  is less than  $G_0$ , which is the small-signal gain coefficient discussed previously. This calculation should be at least a "two-dimensional" analysis, where  $I_r$  varies in the flow direction as well as in the beam direction perpendicular to the flow. Such detailed calculations have been performed by Heiche and Harris<sup>43</sup> at the Naval Ordnance Laboratory (NOL), but they are not generally available in the literature. However, for the sake of comparison, the following example is given to compare  $e_{\max}$  with the calculated actual power extracted from a GDL cavity. More details on this example can be found in Reference 22.

Consider a GDL cavity which is 58.5 cm wide in the beam direction (transverse to the flow) and 1.5 cm high. This size is representative of the NOL 3-Megawatt Arc Tunnel after it was converted for GDL experiments, as described in References 11 and 12. Consider also a very hypothetical Master Oscillator Power Amplifier (MOPA) arrangement (see section III of

these Notes) consisting of a  $1.5 \times 10$  cm rectangular beam traversing the cavity with five side-by-side passes beginning at the nozzle exit. Hence, power is extracted over a cavity length of 50 cm. Assume that the input laser beam has a power  $P_{in} = 10$  KW with a Gaussian intensity distribution in the flow direction. Let  $P_{out}$  be the output power after the last pass. The power extracted from the gas is  $P_e = P_{out} - P_{in}$ . With this arrangement, the coupled power extraction -- nonequilibrium gasdynamic analysis of Heiche and Harris<sup>43</sup> yields the results shown in Table I for  $P_e$ .

TABLE I

$x_{H_2O}$	$e_{max}$ (KJ/lb <sub>m</sub> ) at nozzle exit	$P_e/\dot{m}$ (KJ/lb <sub>m</sub> )	Percent max <sup>o</sup> available
0.01	23.4	12.2	52%
0.035	19.8	10.5	53%
0.07	15.7	6.67	43%

$$\dot{m} = 1.5 \text{ lb/sec}$$

For these results, the reservoir temperature and pressure were 1800°K and 37.5 atm respectively, the mole fraction of CO<sub>2</sub> was 0.07, the nozzle area ratio was  $A_e/A^* = 50$ , and the nozzle throat height was  $h^* = 0.3$  mm. Three cases with different H<sub>2</sub>O mole fractions are shown in Table I. These results show that, for a GDL the size of the NOL 3-Megawatt Arc Tunnel,  $P_e$  is on the order of 1/2 the maximum available power at the nozzle exit. This serves to illustrate the difference between

$e_{\max}$  and the actual power extracted.

As a final note on power extraction, several approximate methods<sup>27,44</sup> are available for predicting power output, generally based on the estimation of saturation intensity within the cavity (see section III). However, for accurate results necessary for reasonable comparison between theory and experiment, and for detailed GDL design, a coupled numerical solution such as described above is required.

#### D. COMPARISON BETWEEN THEORY AND EXPERIMENT

The previous discussions have dealt with calculations of GDL performance. Such calculations clearly show that population inversions, laser gain, and laser power extraction can occur in supersonic expansions of  $\text{CO}_2\text{-H}_2\text{-H}_2\text{O}$  or He mixtures. These calculations have been generally confirmed by experiment, and such experiments are the subject of this section. Also, the results shown in this section draw heavily on References 11 and 45.

##### 1. Kinetic Rate Data

The vibrational relaxation times used to obtain the theory curves in this section are correlations of the data compiled in reference 38, with the single exception of the water rate,  $(\tau_c)_{\text{CO}_2\text{-H}_2\text{O}}$ . Based on recent calculation by Sharma<sup>46</sup> the present model assumes that  $(\tau_{cp})_{\text{CO}_2\text{-H}_2\text{O}}$  is constant for  $T \leq 600^\circ\text{K}$ . This approximation is not good for  $T < 200^\circ\text{K}$ , but such low temperatures are usually not encountered in the flows of interest here.

##### 2. Nonequilibrium Gas Dynamics

In the analysis of reference 8, the kinetic rate equations are fully coupled with the governing flow equations of continuity,

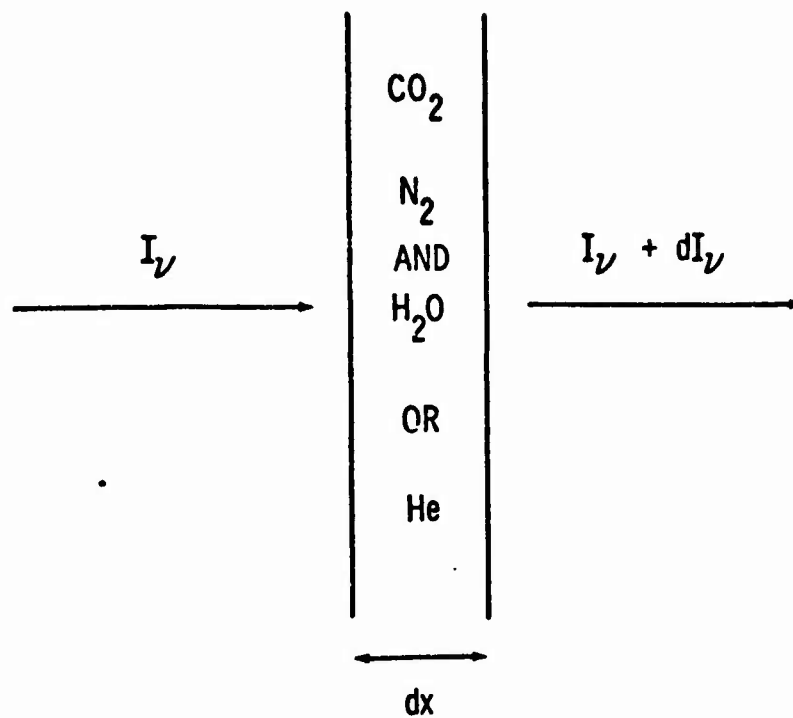
momentum and energy. Nonequilibrium conditions are included both upstream and downstream of the nozzle throat. The governing equations, along with their time-dependent numerical solution have been described in Section C of these Notes. Hence, no further elaboration will be given here.

### 3. Small-Signal Gain

The fundamental experimental measurement discussed in this Section is the small-signal gain coefficient,  $G_0$ , defined as  $dI_v/I_v = G_0 dx$ . Here,  $I_v$  is the intensity of a low power  $\text{CO}_2$  diagnostic laser beam at  $10.6 \mu\text{m}$  incident on an element of gas of thickness  $(dx)$  in the supersonic flow, as shown schematically in Fig. 21. In principle, the intensity increase,  $dI_v$ , yields a measurement of  $G_0$ . The intensity,  $I_v$ , must be small enough such that the radiation field does not disturb the population inversion, i.e., such that  $(N_{001} - N_{100})$  is collision dominated. In this case,  $G_0$  is directly proportional to the population inversion. A detailed discussion and derivation of the small-signal gain equation is given in Section C. With the appropriate rotational constants, a close approximation of eq. (20) for the P(20) transition of the 10.6 band is

$$G_0 = \frac{\lambda^2}{4\pi \tau_{21} \nu_c} (N_{001} - N_{100}) \left( \frac{45.6}{T} \right) e^{-234/T} \quad (40)$$

where  $\lambda = 10.6 \times 10^{-6} \text{m}$ ,  $\tau_{21}$  is the spontaneous radiative lifetime = 5.38 sec,  $\nu_c$  is the collision frequency, and  $T$  is in  $^\circ\text{K}$ . Equation (40) assumes pressure line broadening only; Doppler broadening is negligible



$$\frac{dI_\nu}{I_\nu} = G_0 dx$$

$$G_0 \propto (N_{001} - N_{100})$$

Fig. 21 DEFINITION OF SMALL-SIGNAL GAIN COEFFICIENT

for the pressures of interest at the nozzle exit ( 50 torr). The quantities in Eq. (40) are not limited to a specific set of units; however, they must be consistent, such as the SI system. The numerical constants in the last two factors have units of °K.

Thus, theoretical vibrational population inversions ( $N_{001}-N_{100}$ ) are obtained from the analysis of reference 8; in turn, these are used in Eq. (40) to give theoretical predictions of  $G_0$  for the P(20) transitions of the  $10.6\mu$  band. For other P(J) transitions in the same band, Eq. (40) must be appropriately ratioed, assuming rotational equilibrium. The purpose of the remainder of this section is to compare the theoretically predicted  $G_0$  with experimental measurements.

#### 4. NOL 3-Megawatt Arc Tunnel

The NOL 3-Megawatt Arc Tunnel is an arc heated high temperature supersonic wind tunnel facility<sup>12</sup>. The artist's conception of Figure 22 shows the major conventional components of the wind tunnel. Electrical power is delivered from an AC power supply to the 4 ring, 3 phase AC arc heater. Nitrogen (or air) is heated to the desired pressure and temperature by the arc. In its conventional wind tunnel configuration, the high temperature gas passes through the supersonic nozzle into the test cell, where aerodynamic and heat transfer data are usually obtained. The gas then passes through the diffuser, an after-cooler, and to a vacuum pumping plant.

The arc heater<sup>47</sup> is of the 4-ring 3 phase AC type developed at NOL (See Figure 23). Water cooled copper electrodes and liners are placed within the steel pressure shell. The gas to be heated

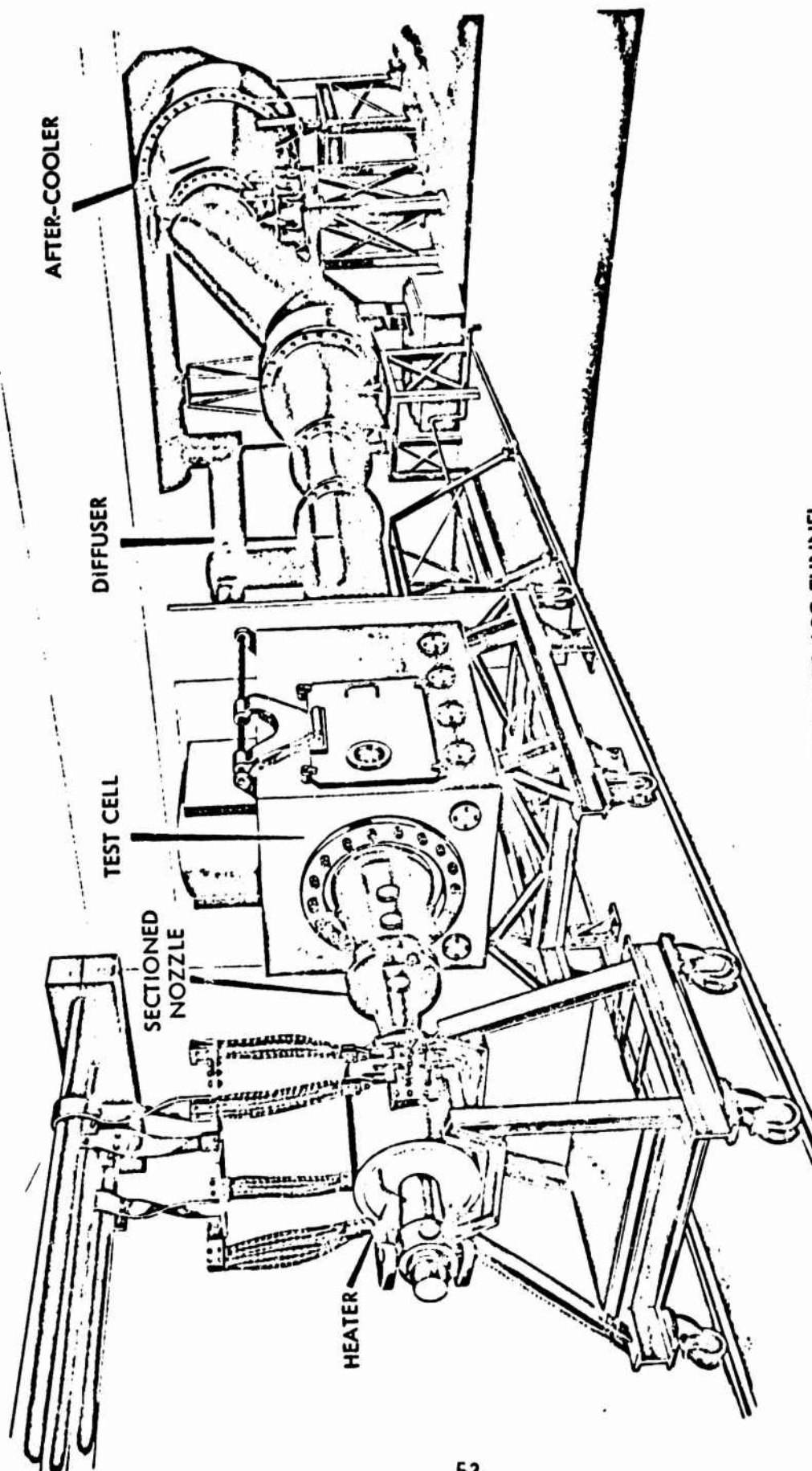


Fig. 22 THREE MEGAWATT ARC TUNNEL

Reproduced from  
best available copy.



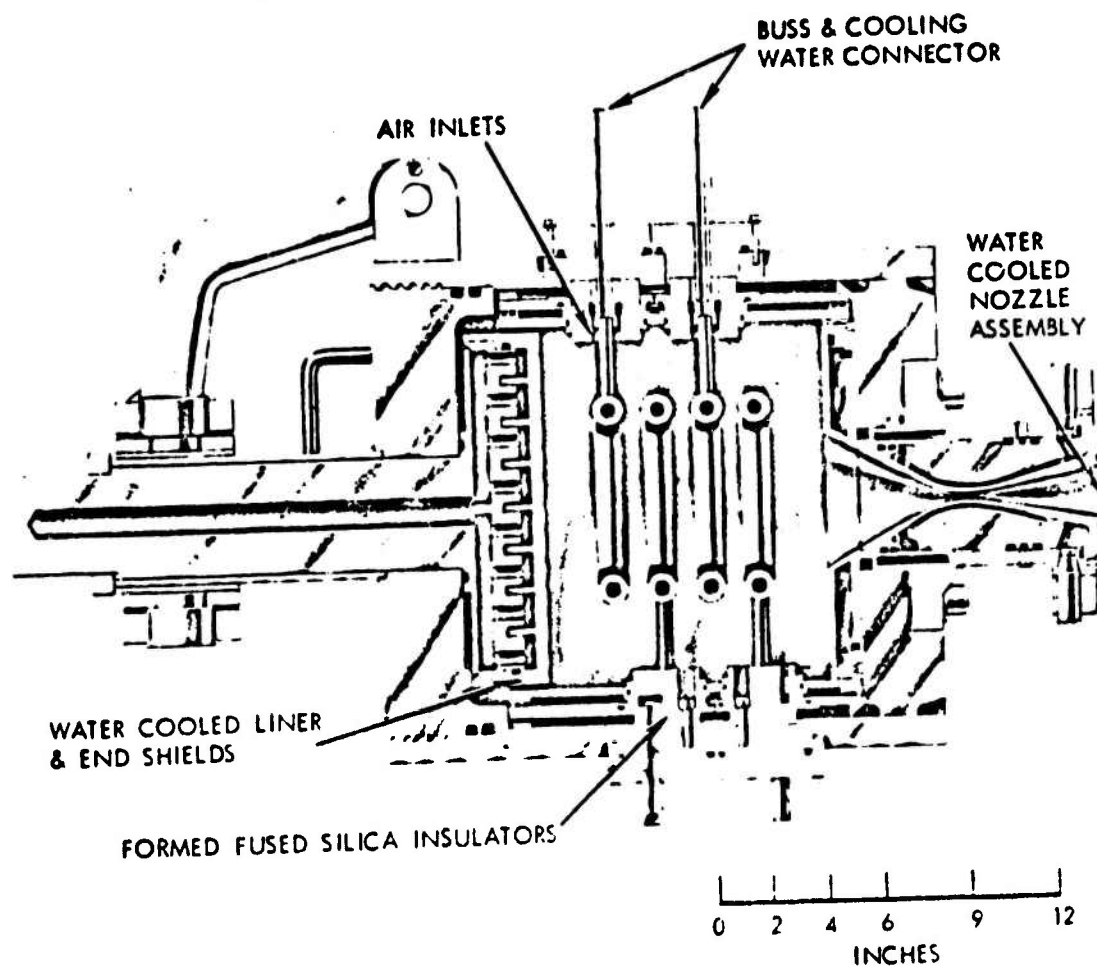


Fig. 23 CROSS-SECTION OF MK IV ARC HEATER

is injected into the chamber through a series of holes around one leg of each electrode. The gas is heated by the two arc columns which (due to their self-induced magnetic field) rotate around the electrodes. The arc heater is capable of operation over a range of temperatures from 1500°K to 6000°K and pressure of 10 to 70 atmospheres. Extensive operating experience at pressures of 10 to 35 atmospheres give heater efficiencies of 25 to 60 percent depending upon the temperature and mass flow required.

For the small-signal gain measurements, the conventional arrangement shown in Figure 22 is modified. Specifically, a mixing chamber, supersonic rapid expansion nozzle and constant area duct are substituted for the conventional wind tunnel nozzle. This modified arrangement is shown in the schematic of Figure 24 and the photo of Figure 25. In the mixing chamber,  $\text{CO}_2$  and liquid  $\text{H}_2\text{O}$  are injected and mixed with the hot  $\text{H}_2$  from the arc heater. The hot gas mixture passes through the supersonic rapid expansion nozzle, where the population inversion is created. The two-dimensional, contoured, minimum length nozzle has a throat height of 1 mm, an inviscid-core area ratio of 20, and a length transverse to the flow of 585 mm. The flow passes through an essentially constant area duct which is provided with a series of 7 viewing ports along its length. The duct is slightly divergent to account for viscous effects. The output beam (10.6  $\mu\text{m}$ , P(20) transition) from a homemade diagnostic  $\text{CO}_2$  gas laser (see Figure 26) is directed into the duct through an IRTRAN window, reflected from a gold-coated mirror on the opposite side of the duct, and passed back out the window

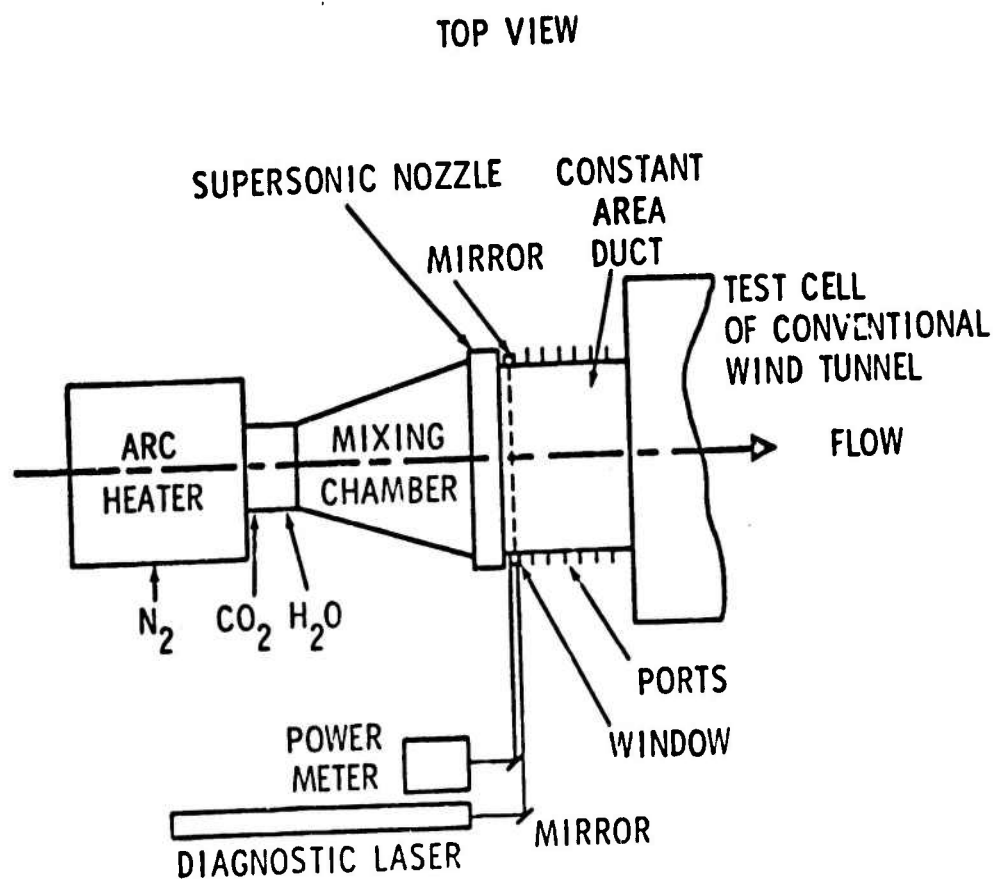


Fig. 24 TOP VIEW SCHEMATIC OF THE NOL 3-MEGAWATT ARC TUNNEL MODIFIED FOR THE PRESENT EXPERIMENTS

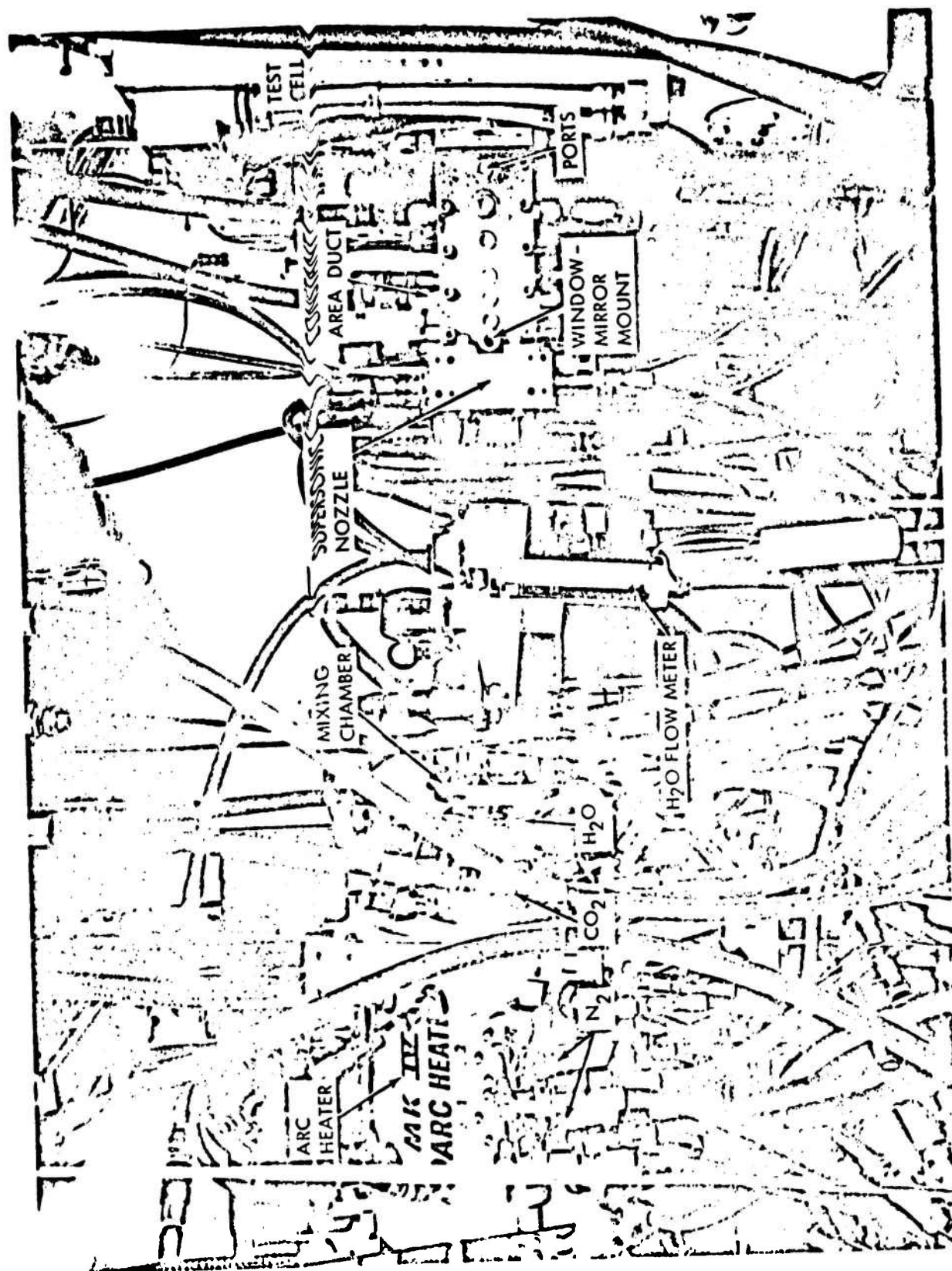


Fig. 25 PHOTOGRAPH OF ARC TUNNEL MODIFICATIONS FOR SMALL-SIGNAL GAIN MEASUREMENTS

Reproduced from  
best available copy.

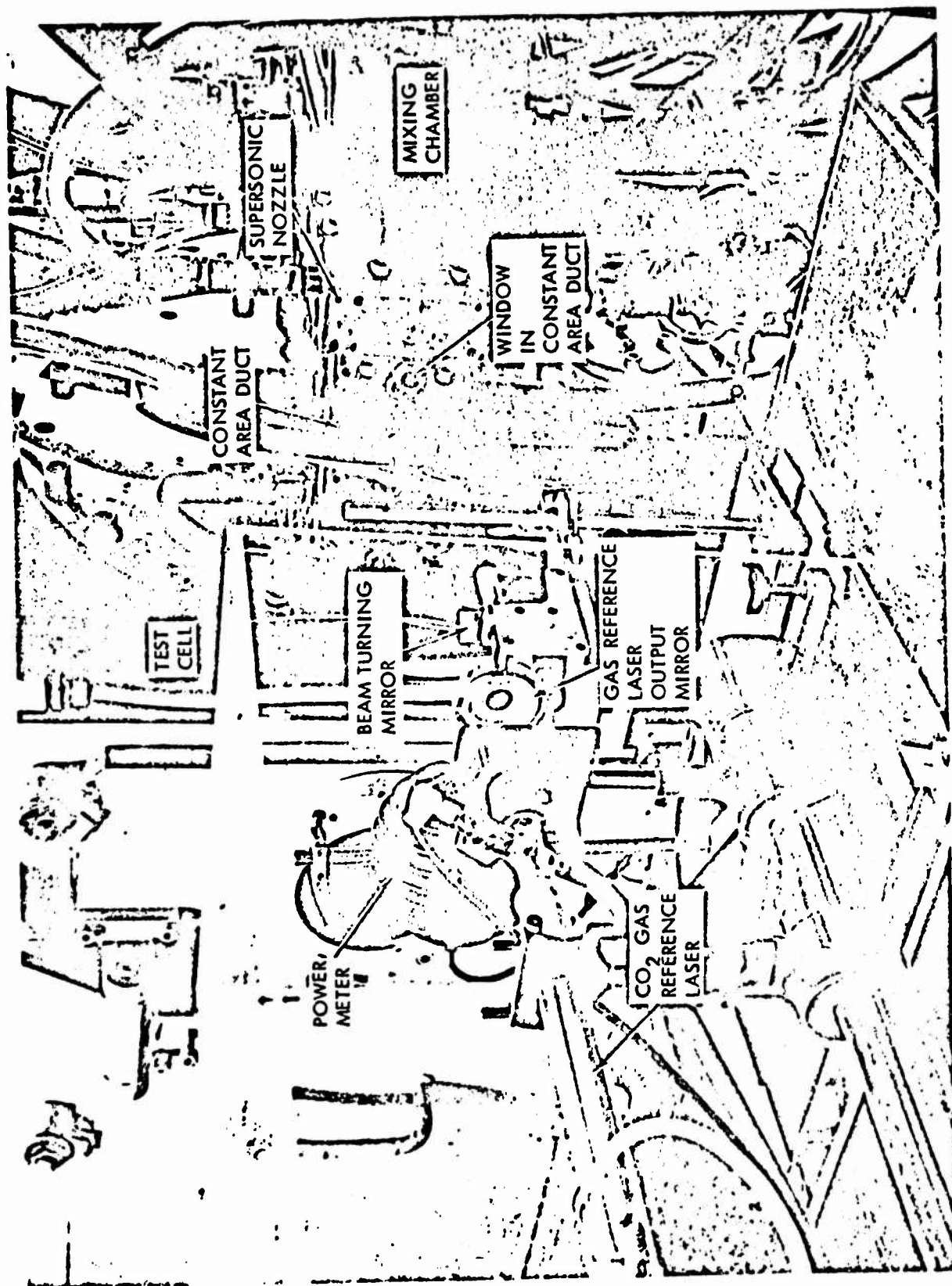


Fig. 26 PHOTOGRAPH OF OPTICAL ARRANGEMENT FOR MEASURING SMALL-SIGNAL GAIN

Reproduced from  
best available copy.

into a broadband cw laser power meter (Coherent Radiation Labs Model 201). The small signal gain along the duct may be measured by moving the window and mirrors so that the diagnostic laser beam passes through the desired point location.

The reservoir temperature of the gas mixture entering the supersonic nozzle is determined by use of a one-dimensional mass flow relationship from a sonic throat condition. The measured arc heater pressure and mass flows of the individual gases ( $N_2$ ,  $CO_2$ , and  $H_2O$ ) are used with specific heat ratios, compressibility factors, and gas constants for the mixture to calculate the nozzle reservoir temperature. The procedure is similar to that normally used in high temperature wind tunnel systems<sup>48</sup>.

The spectral output of the diagnostic  $CO_2$  gas laser was measured with the aid of a Jarrell-Ash model (82000) spectrometer and a liquid nitrogen cooled detector. The laser was found to operate predominately on the P(20) transition; the P(18) and P(16) transitions also occurred, but were weak enough to be ignored in the small-signal gain measurements and in the analytical calculations.

The sequence of events leading to a small-signal gain measurement is as follows. First, the diagnostic laser and optical system are aligned to give the maximum power incident on the power meter. Then, the arc heater is turned on, heating pure  $H_2$  at a temperature somewhat above the final reservoir temperature. When steady flow conditions are reached in the heater, cold  $CO_2$  and liquid  $H_2O$  are injected into the mixing chamber (see Figures 24 and 25). The power meter continuously records the power level of the beam after it has

doubly traversed the duct. The beam power  $W_1$  measured during the steady flow of the  $N_2$ - $CO_2$ - $H_2O$  mixture and the power  $W_0$  measured during the preliminary flow of pure  $N_2$  yield  $G_0$  from the relationship  $W_1/W_0 = \exp(G_0 L)$  where  $L$  is the geometric path length inside the duct.

#### 5. NOL 12.7 cm Shock Tunnel

The arc tunnel discussed above is one means of providing a reservoir of hot, vibrationally excited gas for subsequent expansion through a nozzle. Another means is to utilize the shock-heated gas behind a reflected shock wave in a shock tube. In the present experiments, a conventional pressure driven shock tube is used to provide reservoir conditions behind a reflected shock wave in a mixture of  $CO_2$ - $N_2$ -He. A nonequilibrium population inversion is created when this shock-heated mixture expands through a nozzle mounted at the end of the tube. The flow then passes through a slightly diverging cavity where measurements of  $G_0$  are made, and finally exhausts into an evacuated dump tank. Some features of the experimental apparatus are given below, and a schematic of the shock tube arrangement is given in Figure 28.

The shock tube is 12.7 cm in diameter and utilizes a single diaphragm to separate the driver and driven sections. The driven section terminates with an end wall plate and a .077 mm thick brass diaphragm to separate the nozzle from the driven section prior to performing an experiment. During operation of the shock tube, the incident shock wave reflects from the end plate, produces stagnation conditions for operation of the nozzle, and ruptures the secondary

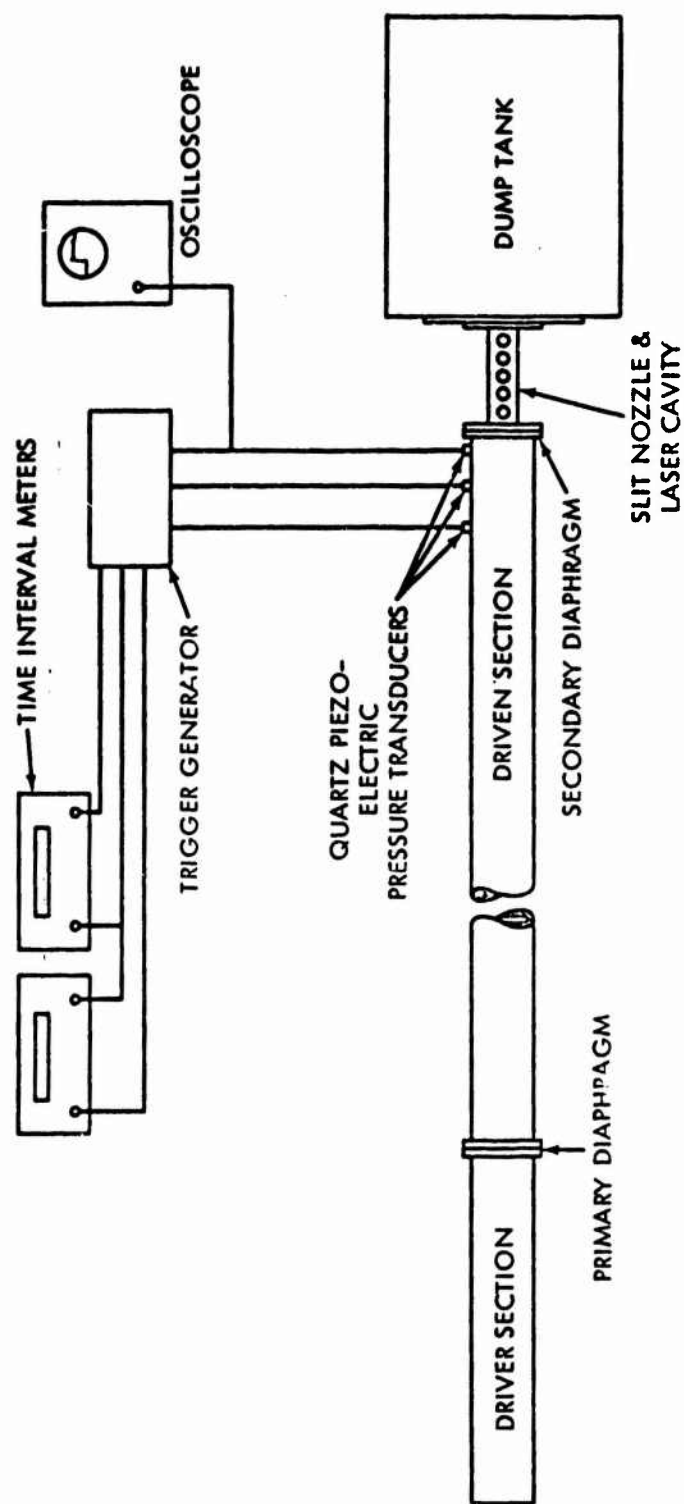


Fig. 28 SCHEMATIC OF THE 12.7 CM SHOCK TUBE GDL FACILITY



diaphragm. Uniform flow is maintained through the nozzle for about 1 millisecond. The nozzle is a minimum length, two-dimensional, contoured slit nozzle with a 1 mm throat height and an inviscid core area ratio of 20. The nozzle width is 12.7 cm. A detailed drawing of the shock tube end wall, nozzle, and cavity is shown in Figure 29.

The shock tube was driven with cold helium in these experiments. A 5.88%  $\text{CO}_2$  - 55%  $\text{N}_2$  - 39.12% he mixture commercially obtained from the Matheson Company is used as the test gas. This gas mixture is supplied with an accuracy of  $\pm 2\%$  of each component. The total impurities, as stated by Matheson, are less than 200 ppm and the  $\text{H}_2$  and  $\text{H}_2\text{O}$  content were each stated as less than 50 ppm. Prior to filling the shock tube with the test gas mixture, it is evacuated to less than  $10^{-3}$  torr.

Experiments were performed for stagnation pressures of 19.47 to 23.56 atmospheres and a range of stagnation temperatures from 1175 to 2240 degrees Kelvin. The stagnation conditions are calculated from normal shock relationships assuming local thermodynamic equilibrium using the method of reference 49 and the measured shock wave speed. Figure 28 shows the instrumentation for the measurement of the shock wave speed. Three quartz piezoelectric pressure transducers (manufactured by PCB Piezotronics, Inc.) and electronic counters are used to measure shock wave transit times. Pressure is measured using the transducer nearest the end wall.

Small-signal gain measurements are made downstream of the nozzle in the laser cavity. Five ports are spaced along the length of the cavity to enable longitudinal  $G_0$  profiles to be made.  $G_0$  is

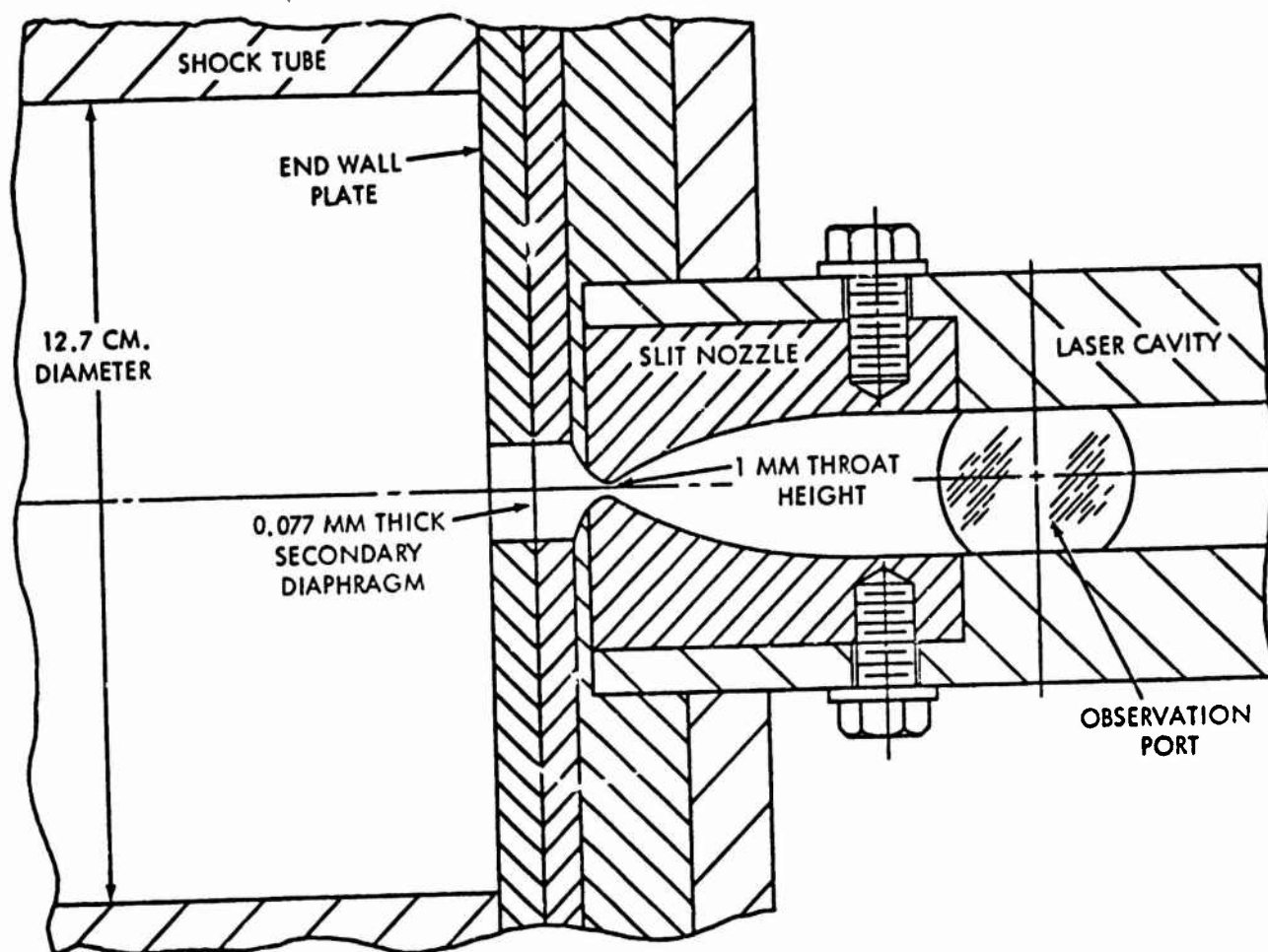


Fig. 29 SLIT NOZZLE - LASER CAVITY ARRANGEMENT

measured by directing the beam of a low power diagnostic laser through the cavity and measuring the increase in power between no flow and flow conditions. A schematic of the instrumentation for measurements of small-signal gain is shown in Figure 30. The diagnostic laser is a Sylvania Model 948 CO<sub>2</sub> laser. The beam is first mechanically chopped to establish a reference level and then sampled (by means of beam splitters) to determine wavelength and amplitude stability. One sampled beam is directed to a focusing mirror which reflects it to a grating blazed at 10 micrometers. This beam is dispersed by the grating and projected on to an OptEngineering thermal imaging screen which displays the individual line or lines present and their corresponding mode structures. The second sampled beam is monitored by detector #1 to determine the amplitude stability of the diagnostic laser. The main probe beam passes through the windows (Irtran 2, antireflection coated) of the cavity and is then diffused by reflection from a rough surfaced aluminum flat to ensure coverage of the active area of the detector #2. A narrow-band-pass filter is inserted in the beam path to prevent extraneous radiation from invalidating the gain measurement. Detectors #1 and #2 are gold-doped germanium photoconductive cells operated at 77°K.

Figure 31 shows a typical oscilloscope trace of the probe beam as detected during an experiment. The lower trace is a 10X amplification of the upper trace. An upstream pressure transducer triggered the oscilloscope. The flat initial portion of the oscilloscope trace is representative of a no-flow condition in the cavity. The increase in signal indicates the start of flow in the cavity. (The upward

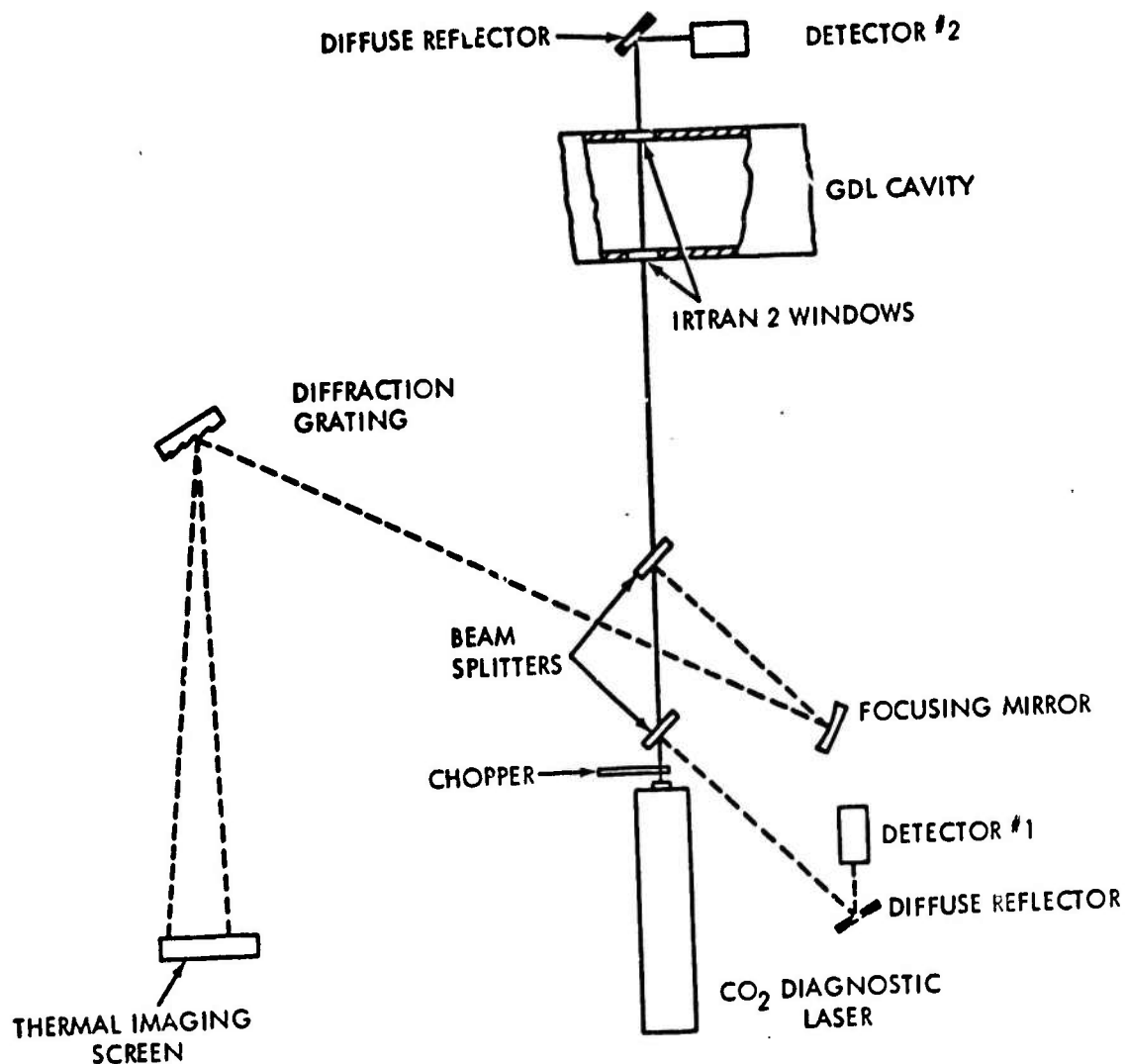


Fig. 30 SCHEMATIC OF INSTRUMENTATION FOR THE MEASUREMENT OF SMALL-SIGNAL GAIN IN THE SHOCK TUNNEL

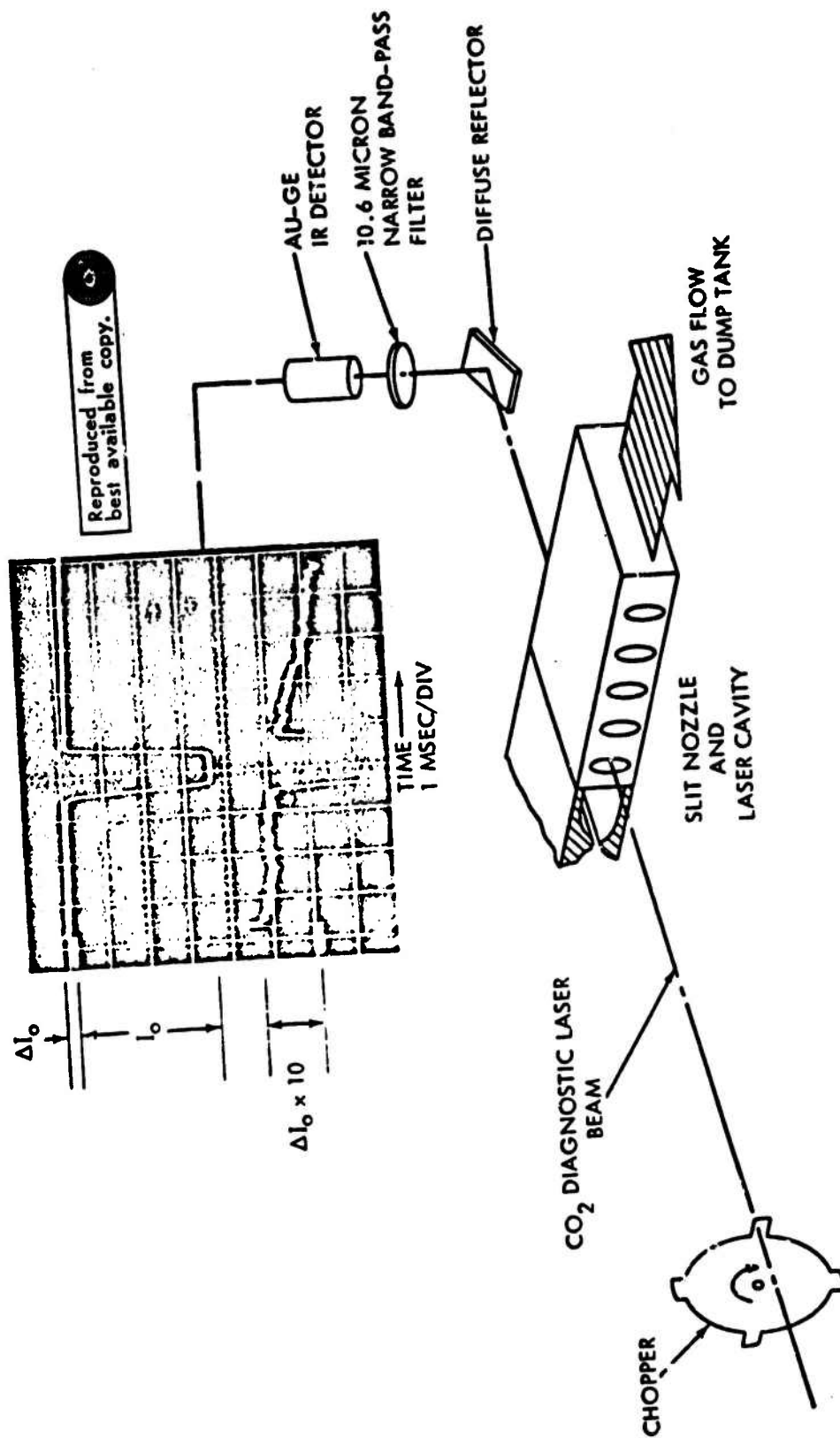


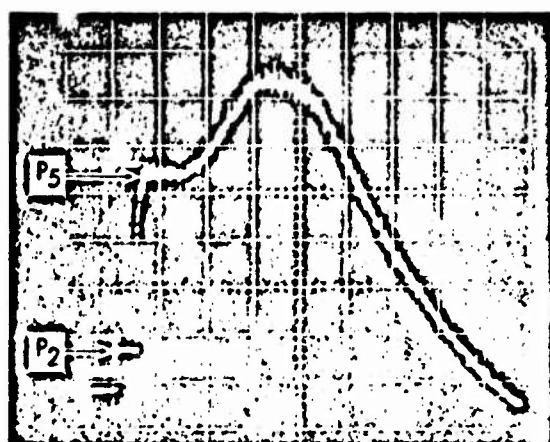
Fig. 31 TYPICAL OSCILLOGRAPH TRACE FROM THE SHOCK TUNNEL GAIN MEASUREMENTS

deflection is indicative of gain.). The rectangular pulse is the chopped signal. The reference is indicated by  $I_0$  and the increase in intensity by  $\Delta I$ . The value of  $G_0$  is given by  $(I_0 + \Delta I)/I_0 = \exp(G_0 L)$ , where  $L$  is the geometric path length (in this case, 12.7 cm for a single tranverse of the cavity). The gain measurements were made on the P(28) and P(30) lines. These lines (rather than the usual P(20) line) were used because the diagnostic laser was more stable at these transitions due to mirror misalignment within the laser.

Typical pressure records near the end-wall are shown in Figure 32. The initial abrupt pressure increase occurs when the incident shock wave passes over the pressure transducer. The second large pressure increase occurs as the reflected shock wave sweeps over the gauge. A pressure plateau persists for approximately 1 millisecond and is subsequently destroyed by wave interactions. Two types of wave interactions are shown in Figure 32. Figure 32a is a pressure trace of conditions where the reflected head of the expansion wave, generated by the rupture of the primary diaphragm, eventually interacts with the reflected shock wave. The expansion wave lowers the pressure and cools the gas and thus terminates the test after about a millisecond running time. By comparison, Figure 32b represents the interaction of the reflected shock wave with the contact surface and the subsequent generation of shock waves which are transmitted back into the stagnation region. These weaker shock waves cause the additional pressure and temperature increase in the nozzle reservoir region which occurs after about 1 millisecond of useful test time.



a.



b.

Fig. 32 TYPICAL OSCILLOGRAPH TRACES OF PRESSURE BEHIND THE REFLECTED SHOCK WAVE

Eventually the pressure rapidly decays, which is indicative of the arrival of the expansion wave.

#### 6. Arc Tunnel Experiments

Considering  $\text{CO}_2\text{-N}_2\text{-H}_2\text{O}$  mixtures, small-signal gain measurements have been obtained in the NOL 3-Megawatt Arc Tunnel as a function of distance from the nozzle throat. A measured  $G_0$  profile is shown in Fig. 33, where it is compared with the theoretically predicted profile obtained from the analysis of reference (8). Very good agreement is obtained. The slight drop of the experimental data below the theoretical curve at large downstream distances is to be expected; the real flow is influenced by boundary layer growth and weak oblique shock patterns in the constant area section whereas the theoretical analysis assumes an inviscid, shock-free flow. The existence of a weak shock pattern has been experimentally observed<sup>50,51</sup>. In fact, a detailed experimental investigation of the fluid dynamics of short, minimum length nozzles is described in reference 51.

Referring to Fig. 33, the initially rapid increase in  $G_0$  as a function of distance is due to the rapid depopulation of the (100)  $\text{CO}_2$  level by  $\text{H}_2\text{O}$ . The (001) level is also being depopulated, but at a slower rate. The peak gain is reached when  $N_{100}$  essentially equilibrates with  $T$ . Downstream of the peak,  $G_0$  decreases due to the continuous deactivation of the (001) level. The different rates of relaxation for the (001) and (100) levels are clearly evident in Fig. 34, where theoretical results for the two vibrational temperatures and the translational temperature are shown as functions of distance along the duct.



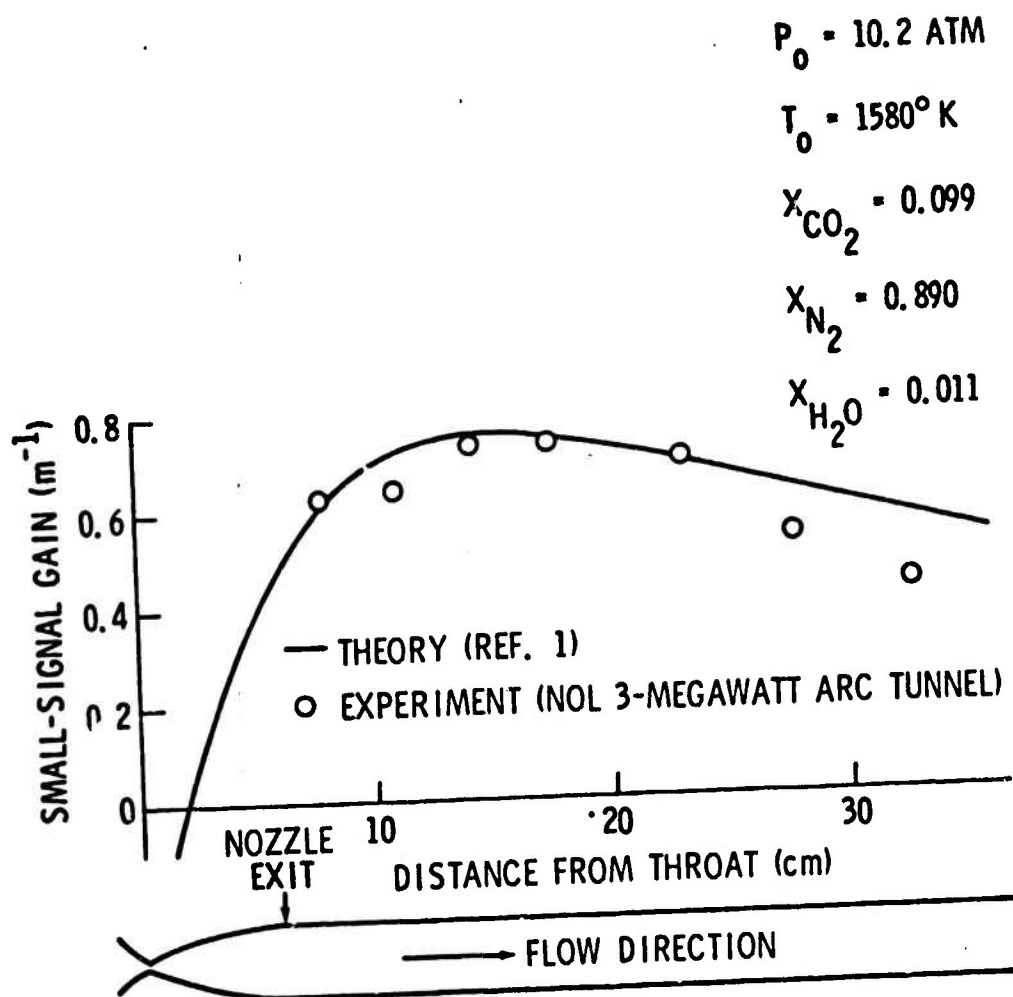


Fig. 33 COMPARISON BETWEEN THEORETICAL AND EXPERIMENTAL SMALL-SIGNAL GAIN PROFILES

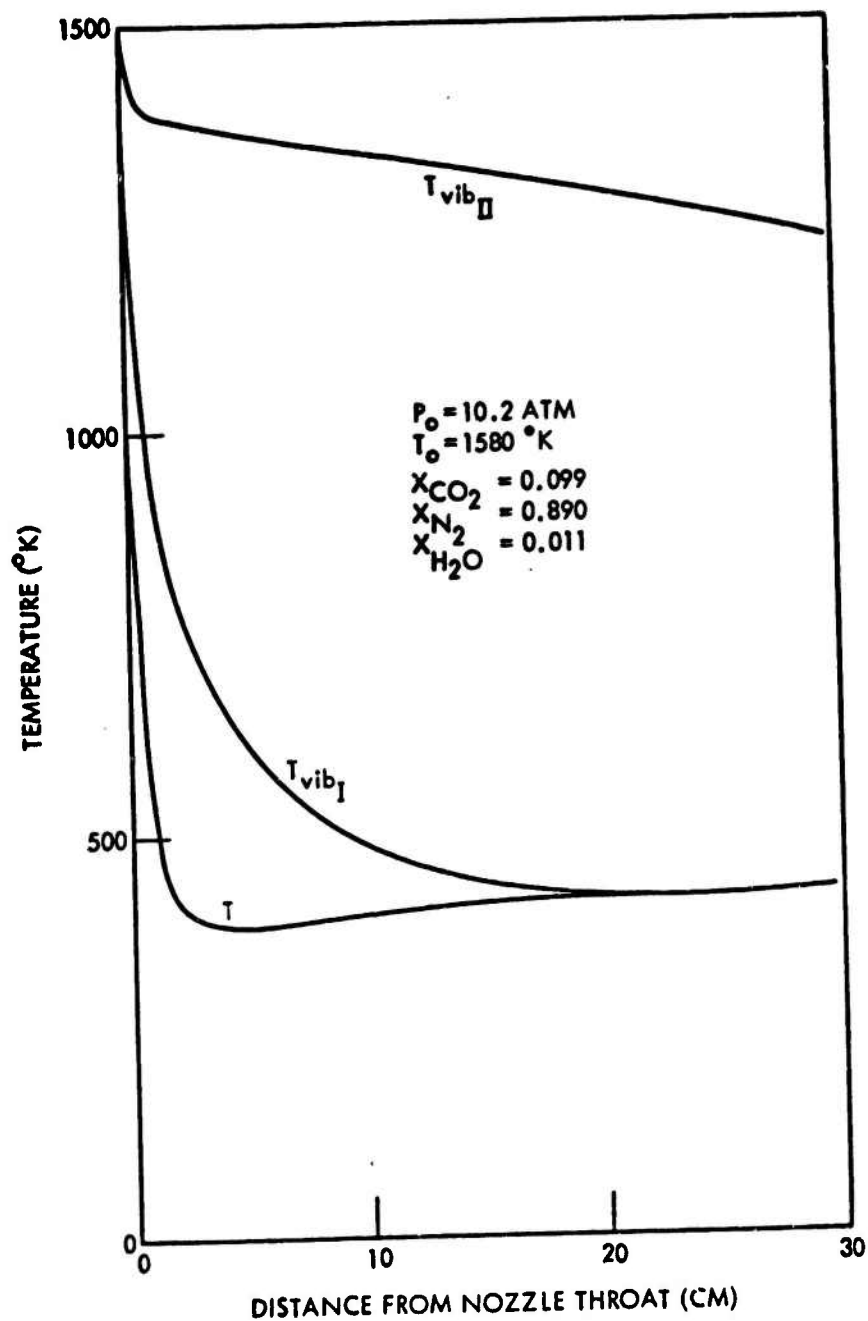


Fig. 34 THEORETICAL VIBRATIONAL AND TRANSLATIONAL TEMPERATURE DISTRIBUTIONS FOR THE CASE SHOWN IN FIG. 14

In addition, the  $G_0$  measured at a fixed station (1.9 cm downstream of the nozzle exit) is shown in Fig. 35 as a function of reservoir temperature. Again, the measurements are compared with theoretical predictions based on reference (8) and again reasonable agreement is obtained.

Examining Fig. 35, at lower temperatures  $G_0$  increases rapidly with  $T_0$  simply because the total vibrational energy in the reservoir increases. However, the relaxation rates also increase with temperature. Moreover, for a nozzle of fixed area ratio, the exit static temperature increases as  $T_0$  increases, hence resulting in larger values for  $N_{100}$  (which is close to equilibration with  $T$ ). For these reasons,  $G_0$  will peak and begin to decrease if  $T_0$  is made large enough. This behavior is clearly evident in Fig. 35. The magnitude and location of the peak depends on nozzle shape and size,  $p_0$  and mixture ratio.

All of the previous measurements have been made along the centerline of the flow. The minimum length, two-dimensional nozzle employed for these measurements is contoured to provide uniform flow at the nozzle exit. Because the flow field is two-dimensional, the fluid elements traveling along different streamlines experience different flow gradients; thus the nonequilibrium history of each streamline is different. This prompts a question regarding the uniformity of  $G_0$  vertically across the nozzle exit. In order to investigate this question, measurements of  $G_0$  were made off the centerline in a direction normal to the flow at a station 1.9 cm downstream of the nozzle exit. These measurements are shown in Fig. 36,

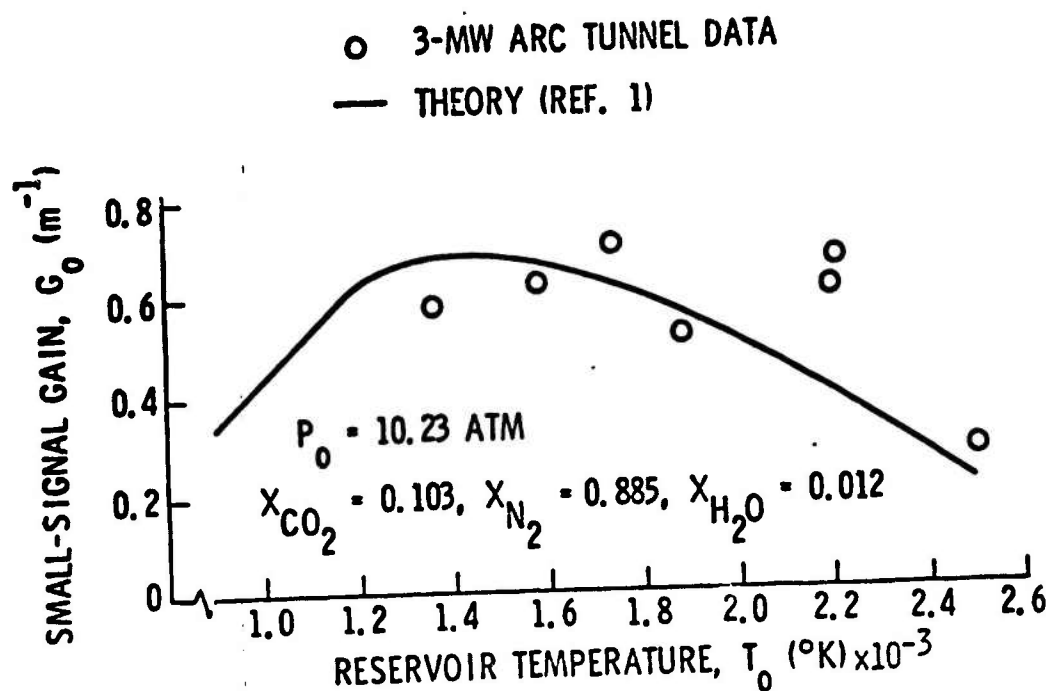


Fig. 35 VARIATION OF SMALL-SIGNAL GAIN WITH RESERVOIR TEMPERATURE: COMPARISON BETWEEN THEORY AND EXPERIMENT

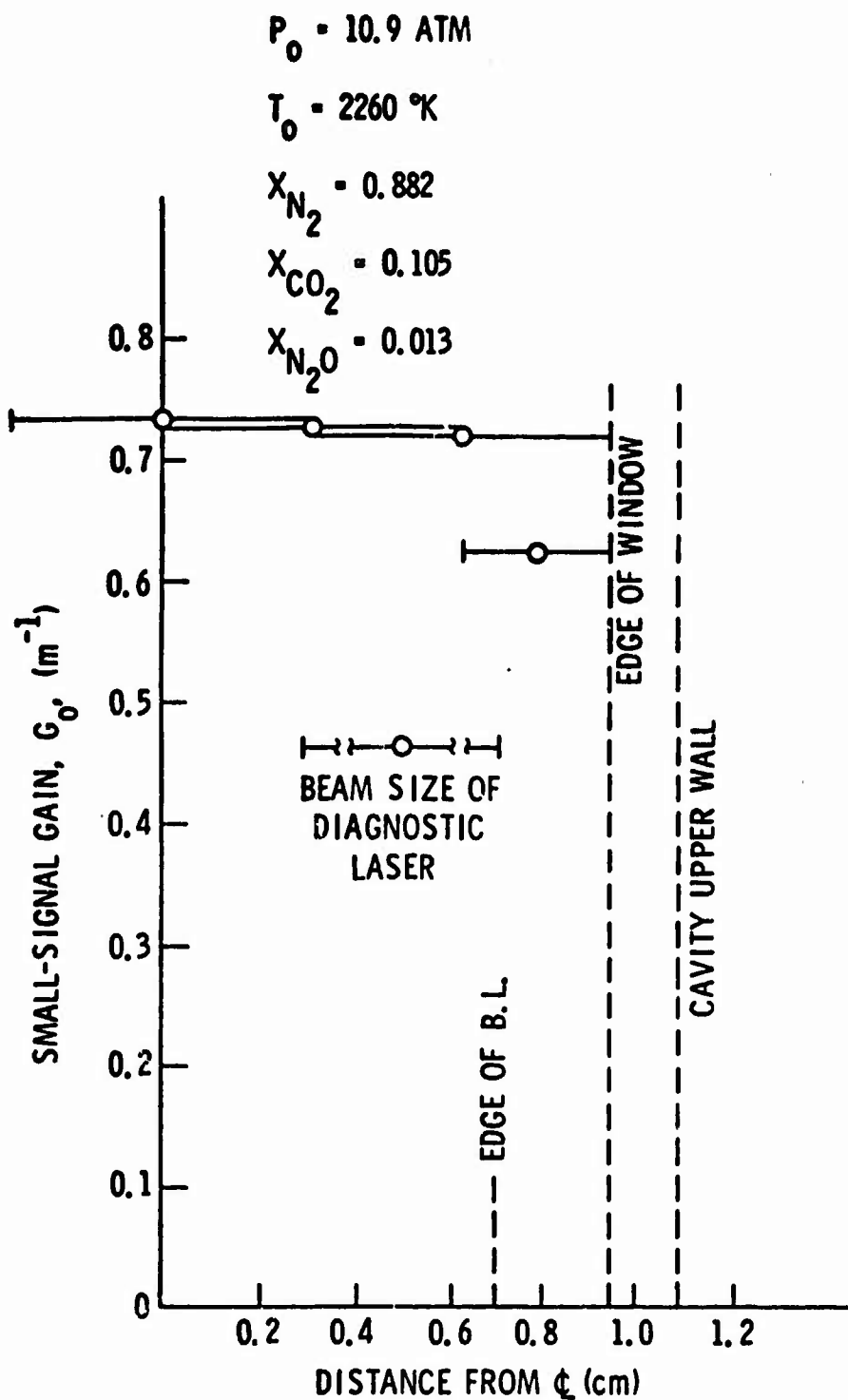


Fig. 36 VARIATION OF SMALL-SIGNAL GAIN TRANSVERSE TO THE FLOW AT A STATION 1.9 CM DOWNSTREAM OF THE NOZZLE EXIT

and demonstrate a remarkably uniform  $G_0$  distribution across the entire inviscid flow region. These off-centerline gain measurements are believed to be the first of their kind, and indicate that two-dimensional effects are not serious for such internal nonequilibrium nozzle flows.

#### 7. Shock Tunnel Experiments

Small-signal gain measurements have also been made in  $\text{CO}_2$ - $\text{N}_2$ -He mixtures in the NOL 12.7 cm Shock Tunnel. The results are shown in Fig. 37, where  $G_0$  at a fixed station (1.27 cm downstream of the nozzle exit) is plotted as a function of  $T_0$ . Also shown in Fig. 37 are theoretical predictions for the P(28) and P(30) transitions of the  $10.6 \mu$  band. These are the transitions on which the diagnostic laser was operating for the present shock tunnel experiments, as discussed earlier. Again, the theory based on reference (8) yields reasonable agreement with experiment, with the exception of the higher temperature range where the measured data fall slightly below theory. It is interesting to note that the equilibrium reservoir conditions for the present measurements indicate 1 percent dissociation for  $\text{CO}_2$  at  $T_0 = 2000^\circ\text{K}$ , growing to 5 percent at  $T_0 = 2250^\circ\text{K}$ . The theoretical results shown in Fig. 37 assume a nonreacting, constant composition mixture and hence do not account for the partial dissociation of  $\text{CO}_2$ . This contributes in part to the over-prediction of  $G_0$  at temperatures above  $2000^\circ\text{K}$ .

Small-signal gain measurements for  $\text{CO}_2$ - $\text{H}_2$ -He mixtures have also been made in a shock tunnel by Christiansen and Tsongas<sup>13</sup> at the University of Washington. Some of these data are shown in Fig. 38, where  $G_0$  is plotted over a wide range of  $p_0$ . The measurements were

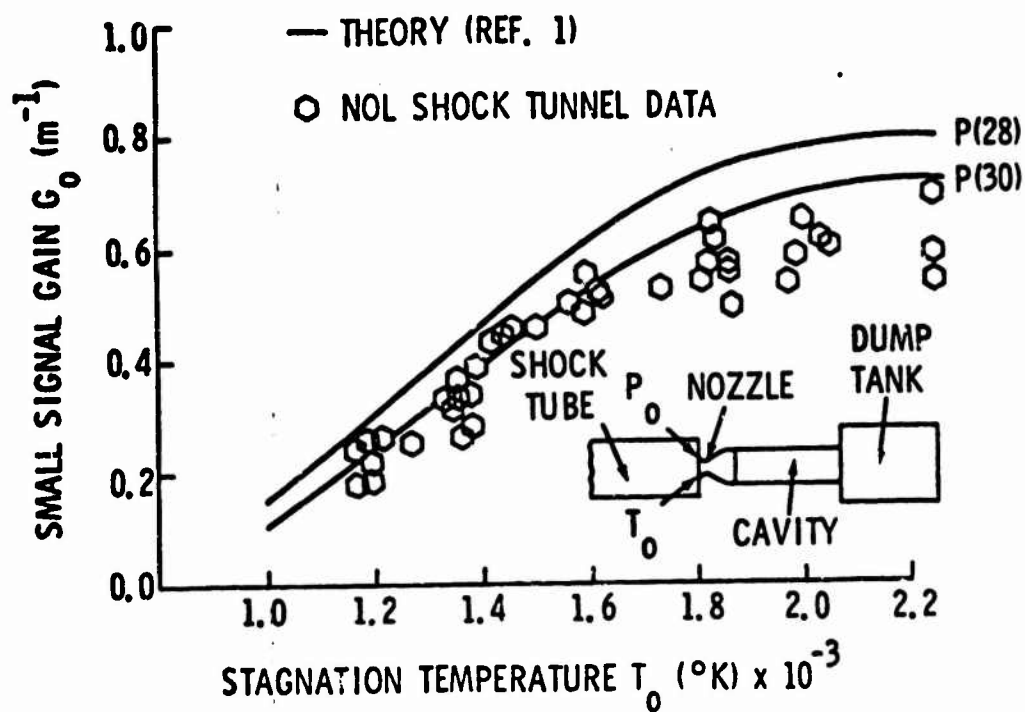


Fig. 37 VARIATION OF SMALL-SIGNAL GAIN WITH RESERVOIR TEMPERATURE: COMPARISON BETWEEN THEORY AND EXPERIMENT AT A STATION 1.27 CM DOWNSTREAM OF THE NOZZLE EXIT,  $P_0 = 20 \text{ ATM}$ ,  $X_{\text{CO}_2} = 0.0588$ ,  $X_{\text{He}} = 0.3912$ ,  $X_{\text{N}_2} = 0.55$

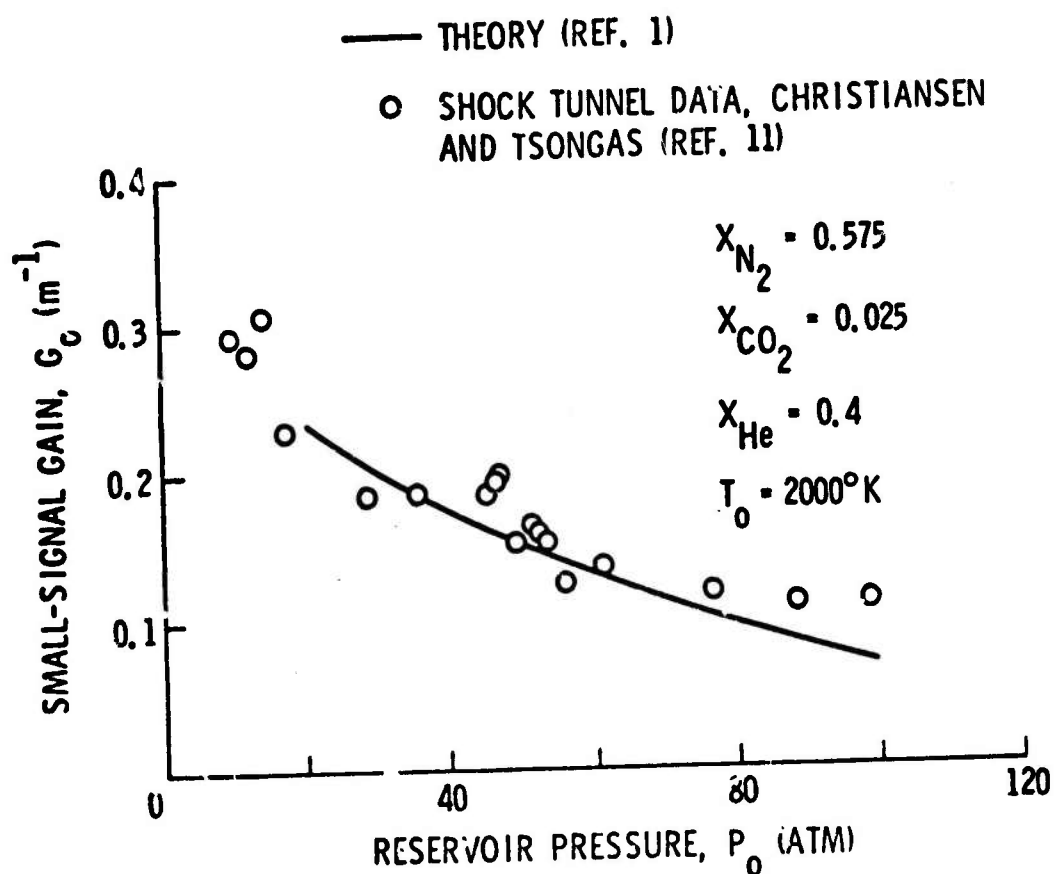


Fig. 38 VARIATION OF SMALL-SIGNAL GAIN WITH RESERVOIR PRESSURE: COMPARISON BETWEEN THEORY AND EXPERIMENT.



made at the exit of a wedge nozzle with throat height = 2 mm, total included angle =  $30^\circ$ , and  $A_e/A^* = 10$ . Also shown in Fig. 38 are the corresponding theoretical predictions from the analysis of reference (8). Reasonable agreement is obtained between theory and experiment.

#### 8. Other Experiments

A complete set of GDL Arc Tunnel experiments have been reported by Lee et al<sup>10</sup>. They give comparisons between theory and experiment for small-signal gain and laser power for  $\text{CO}_2\text{-N}_2\text{-He}$  and  $\text{H}_2\text{O}$  mixtures. The nozzle arrangement was an array of 24 Mach 4 nozzles of 1 mm throat height, in contrast to the single slit nozzles described in the NOL experiments. Some of their results for small signal gain are shown in Figures 39-44, and some power data are shown in Figure 45. In these figures, which are taken directly from Reference 10, the theoretical gain is obtained from the method of Anderson<sup>8</sup>. Fairly reasonable agreement is obtained. The theoretical curves (the solid curves) for power in Figure 45 were obtained from an approximate analysis based on Rigrod<sup>44</sup> for various values of mirror absorptivity. The actual mirror absorptivity in these experiments is not known, and Figure 45 illustrates the tenuous nature of power extraction analyses.

Another set of arc-tunnel GDL experiments were performed by Howgate, Roberts and Barr<sup>52</sup>, and were compared with their detailed numerical calculations of laser power output. Discrepancies between theory and experiment ranged from 7% to 100%, and again illustrates the difficulties involved in accurately predicting power extraction

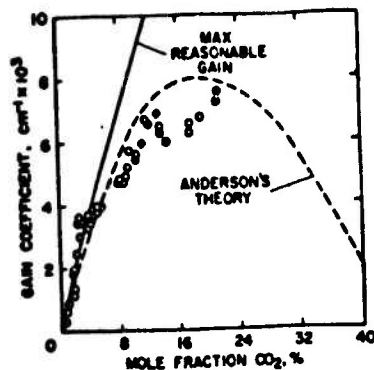


Fig. 39 Effect on  $\text{CO}_2$  concentration on gain.  $\text{He:N}_2 = 0.65$ ,  
 $T = 1250 \text{ K}$ ,  $P = 9 \text{ atm}$ .

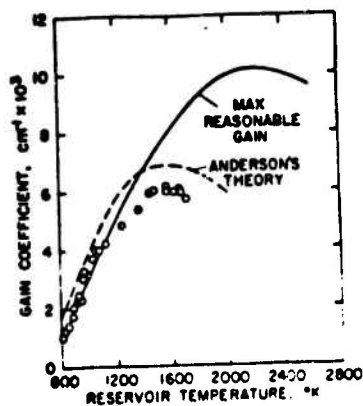


Fig. 40 Effect of temperature on gain.  $6.5\% \text{ CO}_2 - 39.5\% \text{ He} - 54\% \text{ N}_2$ ,  
 $P = 9 \text{ atm}$ .

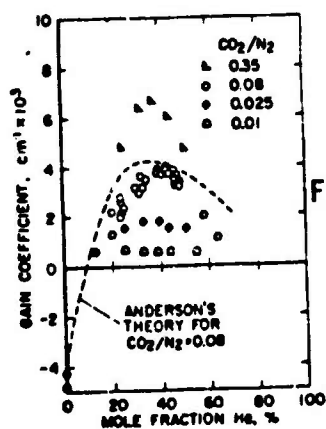


Fig. 41 Effect of helium concentration on gain.  $T = 1250 \text{ K}$ ,  
 $P = 9 \text{ atm}$ .

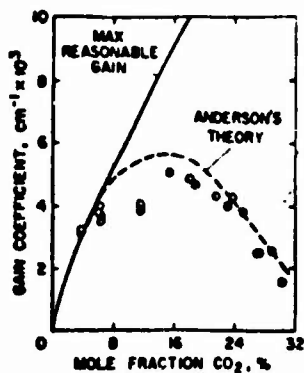


Fig. 42 Effect of  $\text{CO}_2$  concentration on gain. 2.4",  $\text{H}_2\text{O}$ ,  $T = 1175 \text{ K}$ ,  $P = 9 \text{ atm}$ .

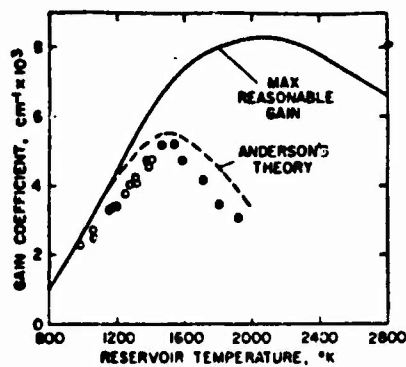


Fig. 43 Effect of temperature on gain. 2.4",  $\text{H}_2\text{O}$ , 6.3",  $\text{CO}_2$ , 91.3",  $\text{N}_2$ ,  $P = 9 \text{ atm}$ .

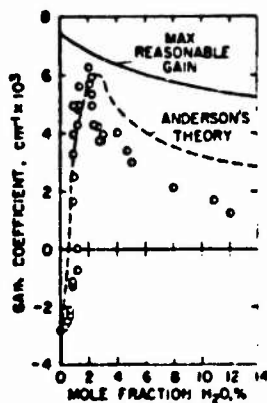


Fig. 44 Effect of  $\text{H}_2\text{O}$  concentration on gain. 6.3",  $\text{CO}_2$ ,  $T = 1540 \text{ K}$ ,  $P = 9 \text{ atm}$ .

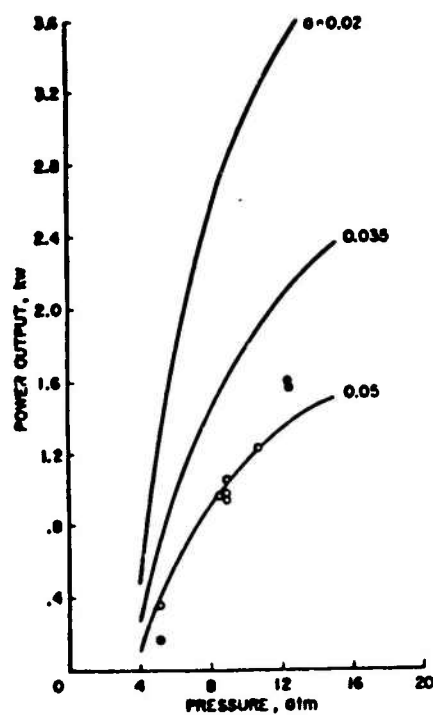


Fig. 45 Effect of pressure on power;  $T = 1350^\circ\text{K}$ ,  $13^\circ$ ,  $\text{CO}_2$ -45%,  
He-42%,  $\text{N}_2$ .

in a GDL cavity.

Finally, with regard to conventional GDL arc-tunnel experiments, McLeary<sup>53</sup> reports "approximate" agreement between his theoretical calculations, and the arc-tunnel results presented by Anderson and Winkler<sup>12</sup>.

Other shock tunnel experiments are reported by Klosterman and Hoffman<sup>2</sup>, Christiansen and Tsongas<sup>13</sup>, Hertzberg et al<sup>14</sup>, Vamos<sup>15</sup>, Tennant et al<sup>16</sup>, Kuehn and Monson<sup>17</sup>, Biriukov et al<sup>54</sup>, Sato and Sekiguihi<sup>55</sup>, and Gembarzhevskiy et al<sup>56</sup>. Throughout all of these, comparison between theory and experiment ranged from poor to very good.

At this point, the reader is reminded that a conventional gasdynamic laser operates with an equilibrium mixture of  $\text{CO}_2$ ,  $\text{H}_2$  and  $\text{H}_2\text{O}$  or He in the reservoir, independently of the way in which this hot, high pressure mixture is obtained. It can be formed in an electric arc or by means of shock heating, as previously described, or it can also be formed by chemical combustion as initially reported by Gerry<sup>1</sup>. Several combustion-driven GDL's have been reported by Gerry<sup>1</sup>, Tulip and Sequin<sup>18</sup>, Yatsiv et al<sup>19</sup>, Meinzer<sup>20</sup>, and Gabai et al<sup>57</sup>. In each of these, comparisons are made with theory, and again various degrees of agreement are obtained. Of particular interest are the extensive parametric tests of Meinzer<sup>20</sup>, including the effect of  $\text{H}_2\text{O}$  on GDL gain all the way to 50%  $\text{H}_2\text{O}$  content. Meinzer<sup>20</sup> compares his experimental data with results obtained from the analysis of Anderson<sup>8</sup>, showing some reasonable agreement.

A final remark is in order concerning the comparison of theory with experiment. Anderson<sup>25,26</sup> has recently reported that, based on the current discrepancies in the existing rate data, an uncertainty of 25-30% can be expected in any calculation of gasdynamic laser performance. These thoughts are given in detail in Appendix A of the present notes. Also, in addition to uncertainties in the kinetic rates, any comparison between theory and experiment is subject to error due to shock wave and viscous flow effects in the laser cavity; such effects are generally not included in the existing theoretical analyses.

#### E. INVERSIONS BEHIND NORMAL SHOCK WAVES

Basov and Oraevskii<sup>3</sup> suggested that population inversions in molecular systems could be obtained by rapid heating of the system, as well as by rapid cooling as in the case of the conventional gasdynamic laser. One of the most rapid ways of heating a gas is by means of a shock wave. Therefore, let us examine the purely vibrational relaxation process behind a normal shock wave in CO<sub>2</sub>-N<sub>2</sub>-He mixtures, and assess what inversions, if any, occur in the nonequilibrium flow. This problem has been examined by Anderson and Madden in References 58-59.

Consider the gasdynamic flow model shown in Figure 46. We make the standard assumptions of a stationary, discontinuous shock front with frozen conditions immediately behind the front. Hence, at this location  $\rho_2$ ,  $T_2$ , and  $u_2$  are obtained from the standard calorically perfect gas equations for normal shocks, and  $e_{vib_1}$  and

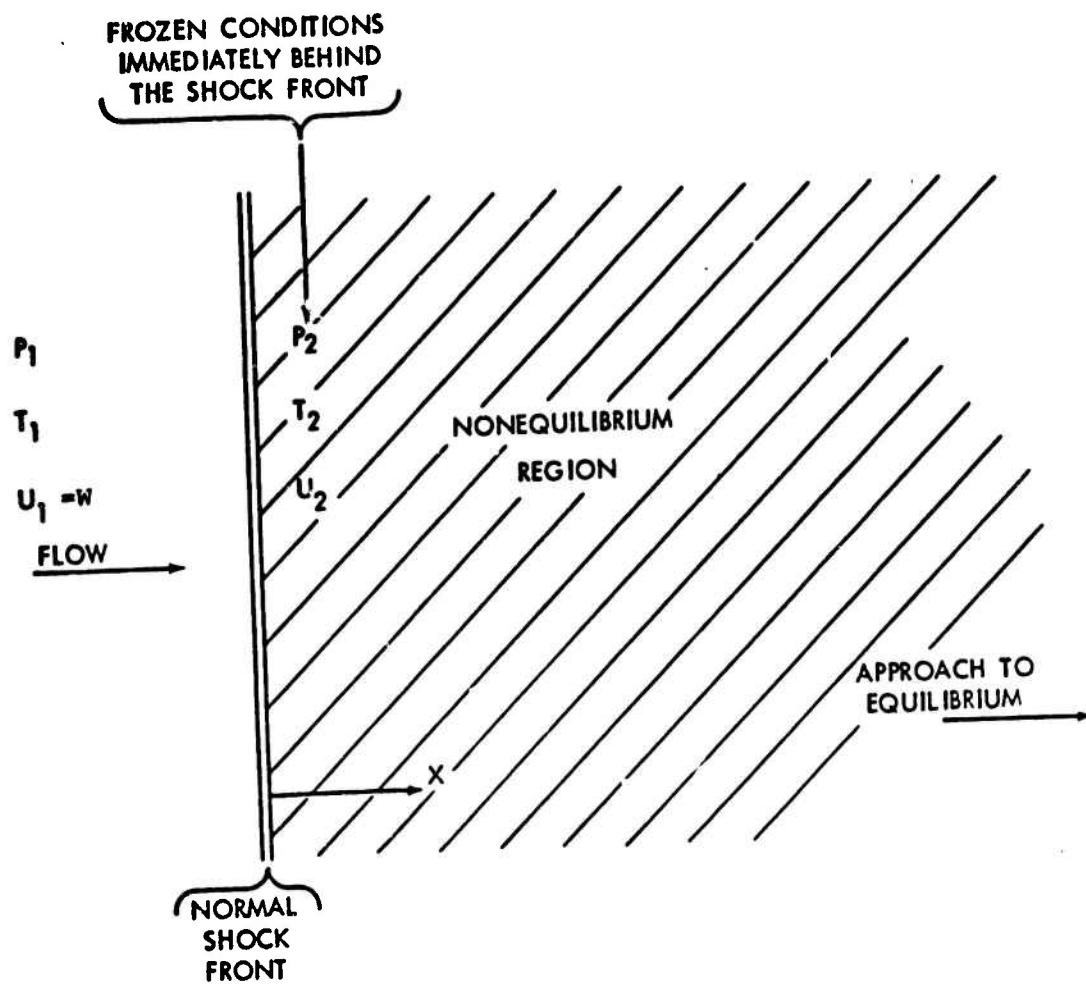


Fig. 46 GAS DYNAMIC FLOW MODEL

$e_{vib_{II}}$  are equal to their respective upstream values. In turn, these quantities are the boundary conditions for the downstream nonequilibrium flow, which is solved by forward numerical integration of the governing steady flow conservation equations as functions of distance behind the shock front. These equations are:

Continuity:  $u \frac{dp}{dx} + p \frac{du}{dx} = 0$  (41)

Momentum:  $(RT/p) \frac{dp}{dx} + R \frac{dT}{dx} + u \frac{du}{dx} = 0$  (42)

Energy:  $RT \frac{du}{dx} + u R \alpha \frac{dT}{dx} + u \frac{d}{dx} (e_{vib_I} + e_{vib_{II}}) = 0$  (43)

Rate:  $\frac{de_{vib_I}}{dx} = \frac{\dot{w}_I}{u}$  and  $\frac{de_{vib_{II}}}{dx} = \frac{\dot{w}_{II}}{u}$  (44)

where  $\alpha = \frac{3}{2}x_{He} + \frac{5}{2}(x_{CO_2} + x_{N_2})$ ,  $p = \rho RT$ , and the notation is standard. The solution is terminated when equilibrium values of the normal shock properties are closely approached; equilibrium normal shock properties for  $CO_2$ - $H_2$ -He mixtures are known in advance from Ref. 49. A detailed discussion of the numerical aspects of the present study can be found in Ref. 59.

Numerical results for a typical case are shown in Figs. 47 and 48. Figure 47 illustrates temperature variations in the nonequilibrium region behind the shock front, and clearly shows the rapid equilibration of  $T_{vib_I}$  with the translational temperature  $T$ , whereas in contrast,  $T_{vib_{II}}$  relaxes more slowly. At a distance of 4 mm downstream of the shock front, all three temperatures have equilibrated within one percent of the final equilibrium temperature, which has been taken from the results of Ref. 59. The results shown in Fig. 49 reflect a molecular collisional process



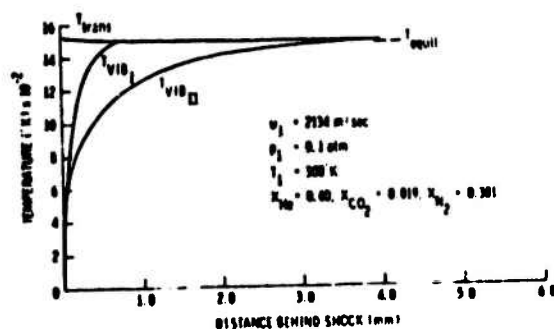


Fig. 47 Variation of translational and vibrational temperature behind the shock front.

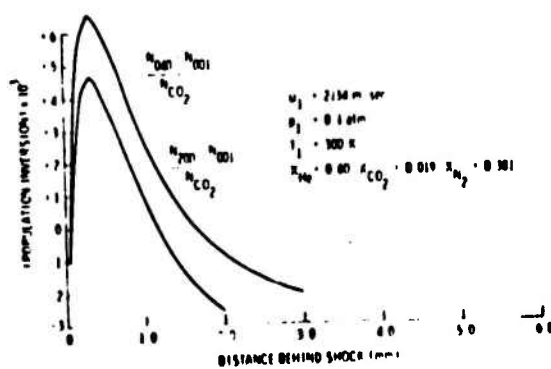


Fig. 48 Variation of population inversions behind the shock front.

which indeed leads to population inversions behind the shock front, as shown in Fig. 48. These inversions occur between the  $(04^00)$  and  $(001)$  levels and to a lesser degree between the  $(200)$  and  $(001)$  levels in  $\text{CO}_2$ . Examining Fig. 48, near the shock front the inversions rapidly increase due to the rapid population of the excited levels of mode I while at the same time the excitation of mode II is lagging far behind. However, the inversion soon peaks and begins to decrease farther downstream as the lower  $(001)$  level is substantially populated. Note that, for the given upstream conditions, the inversions persist over a length from 1-2 mm behind the shock front. The vibrational kinetics obey binary scaling; hence, the spatial extent of the population inversions can be increased or decreased by a proportional decrease or increase in  $p_1$ , keeping  $T_1$  and  $u_1$  the same. Many additional results obtained from the present study are discussed in Ref. 59.

How do the laser properties of this nonequilibrium shock flow compare with those obtained by rapid expansions? First, the conventional, rapid expansion gas dynamic laser creates a population inversion between the  $(001)$  and  $(100)$  levels in  $\text{CO}_2$  which subsequently lases at  $\lambda = 10.6$  . In contrast, the inversions shown in Fig. 48 between the  $(04^00)$  and  $(001)$  levels, and between the  $(200)$  and  $(001)$  levels, would correspond to laser transitions at  $50\mu$  and  $22\mu$ , respectively. An important parameter for gas lasers is small signal gain,  $G_0$ , defined as  $dI/I = G_0 dz$  where  $I$  is the incident radiation intensity on a slab of laser gas of thickness  $dz$ , and  $dI$  is the increase in beam intensity after traversing the length  $dz$ . As shown in Appendix A of Ref. (32),

$G_0 = (\lambda^2 / \tau_{21}) IN = (M^2 / \lambda) IN$ , where  $\tau_{21}$  is the spontaneous radiative lifetime for a transition between the upper and lower laser levels,  $M$  is the corresponding quantum mechanical matrix element, and  $IN$  is the population inversion. For  $CO_2$ , computed values of  $M$  for the  $50\mu$ ,  $22\mu$ , and  $10.6\mu$  transitions are in the ratio  $0.21 \times 10^{-2} : 0.21 \times 10^{-2} : 0.34 \times 10^{-1}$ , respectively.<sup>60</sup> Also, the shock induced population inversions shown in Fig. 48 are approximately one order of magnitude smaller than typical inversions created in rapid expansion through supersonic nozzles. In light of the above numbers, a comparison of  $G_0$  at  $50\mu$  and  $22\mu$  behind a shock wave with  $G_0$  at  $10.6\mu$  in a rapid expansion leads to  $(G_0)_{50\mu} / (G_0)_{10.6\mu} \approx 10^{-4}$  and  $(G_0)_{22\mu} / (G_0)_{10.6\mu} \approx 2 \times 10^{-4}$ . Clearly, the nonequilibrium region behind a normal shock wave in  $CO_2$ - $N_2$ -He mixtures produces a low-gain medium. A more detailed discussion and comparison of these and other laser properties are contained in Ref. 59.

This study indicates that population inversions occur behind a normal shock front due strictly to translation-vibration and vibration-vibration molecular energy exchanges in  $CO_2$ - $N_2$ -He mixtures. However, the laser properties of this shock-induced nonequilibrium flow are clearly not as promising as those of gas dynamic lasers operating on the principle of rapid expansion.

## II. GASDYNAMIC LASERS: STATE-OF-THE ART

### A. INTRODUCTION

High energy gas lasers are a modern reality. Moreover, the technology of these lasers is growing vigorously in at least three directions, namely, gasdynamic, electric discharge and chemical lasers.

The basic physical process common to all these lasers is the competition between stimulated emission and absorption of monochromatic radiation, where the radiation (photon) energy corresponds to the difference between two distinct energy levels of an atomic or molecular system. It has been shown in Section I-B that stimulated emission will win over absorption if a population inversion exists between the two energy levels, i.e., if  $(N_2 - N_1) > 0$ , and therefore laser energy can in principle be extracted from the gas. In electric discharge lasers, the upper energy level is preferentially populated by collisions with electrons energized by an electric field; in chemical lasers, the products of highly energetic chemical reactions are formed directly in vibrationally or electronically excited states with the upper levels preferentially populated; in gasdynamic lasers, an initially hot gas in thermodynamic equilibrium is rapidly expanded through a supersonic nozzle, and an inversion is formed by differential relaxation processes in the nonequilibrium nozzle flow. Of these three types of lasers, the gasdynamic laser has produced the highest continuous wave power to date<sup>1,2</sup>.

The results embodied in References 1,2,6,8,9-14,16-20,52-57 represent (for the most part) a "first generation" of GDL technology, where mixtures of  $\text{CO}_2\text{-N}_2\text{-H}_2\text{O}$  or He are utilized at typical conditions of  $p_0 \approx 20$  atm,  $T_0 \approx 1200^\circ\text{K}$ ,  $h^* \approx 1$  mm,  $A_e/A^* \approx 20$ , and water mole fraction

$x_{H_2O}=0.01$ . (An exception is the high pressure work of Hertzberg<sup>14</sup> and Christiansen<sup>13</sup> which deals with  $p_0$  in hundreds of atmospheres.) In light of this previous work, the purpose of the present section is twofold: (1) To survey some recent advances which contribute to the "second generation" of GDL technology, and (2) To present experimental and theoretical results which typify these advances. In particular, this second generation of GDL's is characterized by higher reservoir temperatures and pressures, smaller nozzle throat heights, larger area ratios, and larger  $H_2O$  contents. Moreover, in some cases new gases and lasing transitions are being employed, such as the interesting work of McKenzie<sup>61</sup> with  $CO-N_2-Ar$  mixtures.

As a final introductory note, in the following sections all theoretical values for small-signal gain and maximum available energy are obtained from the time-dependent nonequilibrium nozzle analysis discussed in Reference 8, and are calculated with the computer code described in Reference 62. As discussed in Section I-C, this analysis fully couples the vibrational kinetic rate equations with the governing quasi-one-dimensional flow equations of continuity, momentum and energy. Nonequilibrium conditions are included both upstream and downstream of the nozzle throat. A simplified vibrational model is used which approximates the detailed molecular energy transfer. The experimental results of References 9-11 show that the model and analysis of Reference 8 yield reasonable agreement with experimental data for gasdynamic laser gain. Also in the present discussion, the maximum available energy,  $e_{max}$ , is always the local

value at the nozzle exit; hence,  $e_{\max}$ , takes into account the vibrational relaxation in the nozzle. In this manner, the present  $e_{\max}$  is different from that defined in Reference 1, where the maximum available energy is based on reservoir conditions. The precise definition and calculation of  $e_{\max}$  is given in Section I-C of the present notes.

#### B. INCREASED H<sub>2</sub>O CONTENT

For CO<sub>2</sub>-N<sub>2</sub> gasdynamic lasers, the presence of H<sub>2</sub>O or He is extremely beneficial for the rapid deactivation of the lower laser level; indeed, such a "catalyst" is necessary for the production of high gain and efficient extraction of laser power. The typical GDL described in Reference 1 is combustion driven, therefore H<sub>2</sub>O rather than He is the meaningful catalyst for such devices. Experience gained with the first generation of GDL technology indicated that gain is a very sensitive function of H<sub>2</sub>O content; along with the beneficial deactivation of the lower level, there is also the competing detrimental deactivation of the upper level due to H<sub>2</sub>O. Hence, with the first generation of GDL's, an optimum amount of H<sub>2</sub>O in the gas mixture was found to be on the order of 1 percent, i.e.,  $x_{\text{H}_2\text{O}} = 0.01$ . For H<sub>2</sub>O contents much larger than this, the collisional deactivation of the upper laser level is overwhelming. Such effects are shown by the lower curves in Figures 49 and 50. In Figures 49 and 50, theoretical values for peak small-signal gain and maximum available energy, respectively, are given as a function of  $x_{\text{H}_2\text{O}}$ . (In the spirit of the SI system of units,  $e_{\max}$  is given in kJoules/kgm; however, the

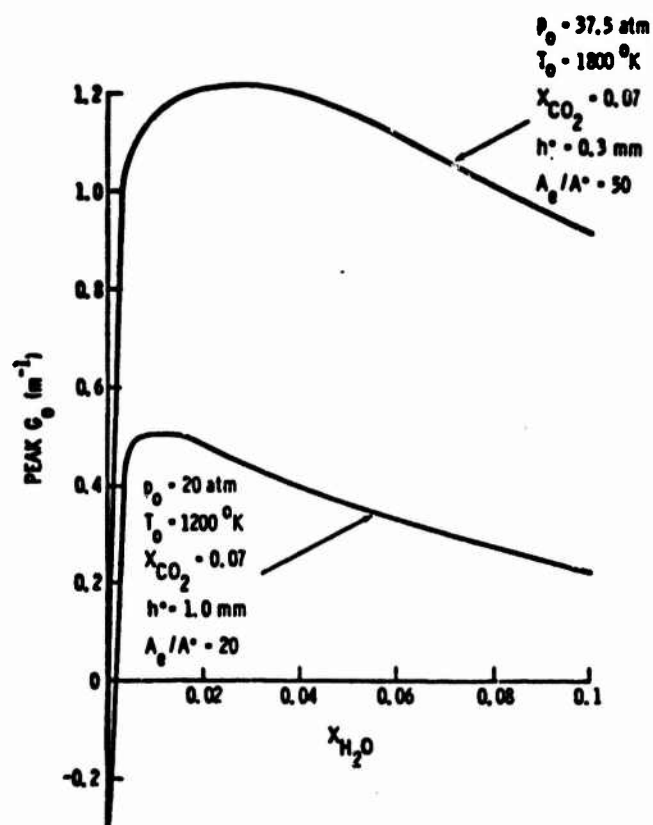


Fig. 49

Peak gain as a function of  $\text{H}_2\text{O}$  content for first and second generation GDL's.

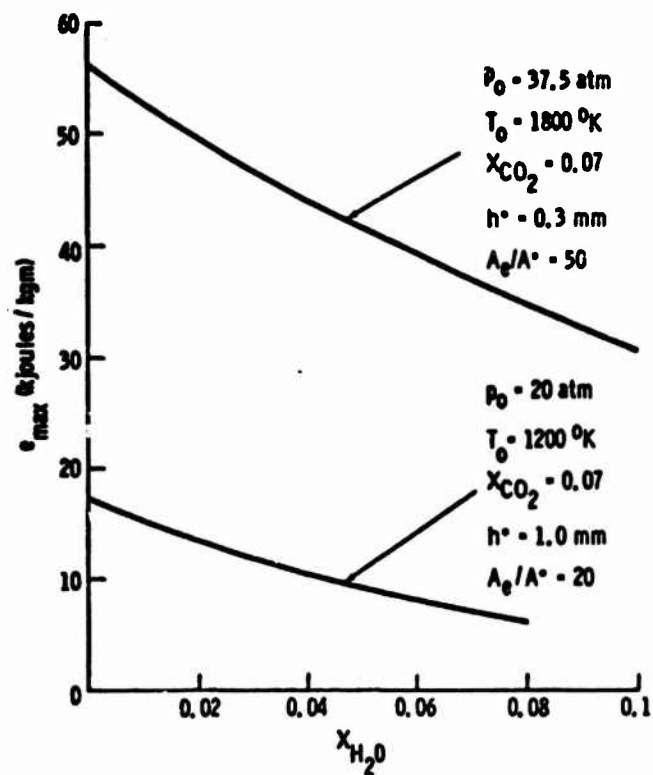


Fig. 50  
Maximum available laser energy as a  
function of  $H_2O$  content for first  
and second generation GDL's.



more common GDL unit is kJoules/lb<sub>m</sub>, where 1 kJoules/lb<sub>m</sub> = 0.454 kJoules/kgm.) The lower curves in both these figures typify the first generation technology, for which the maximum peak gain is clearly seen to occur around  $X_{H_2O} = 0.01$ .

The low value of  $X_{H_2O} = 0.01$  for optimum gain places a severe constraint on candidate fuels for GDL's; most conventional fuel-oxidizer combinations which produce CO<sub>2</sub> and N<sub>2</sub> also produce H<sub>2</sub>O far in excess of 1 percent. (See Reference 63.) Therefore, recent efforts have been made to study the effects of higher H<sub>2</sub>O content on GDL's, say, in the range from 1 to 10 percent. In this vein, Yatsiv et al<sup>19</sup> and Tulip and Seguin<sup>18</sup> have operated GDL's with attendant H<sub>2</sub>O contents up to 8 percent. (Tulip and Seguin have very recently used gasoline in a GDL.) Also, some earlier gain measurements made in the NOL 3-Megawatt Arc Tunnel<sup>12</sup> covered a H<sub>2</sub>O range from 0 to 6 percent. These experiments have shown that small-signal gain does indeed persist at high H<sub>2</sub>O content. This is also clearly shown by the lower curve of Figure 49, where  $G_0$  persists for H<sub>2</sub>O content at least as high as 10 percent, albeit substantially reduced from its optimum value which occurs around 1 percent. Of more consequence for first generation GDL's, however, is the drastic reduction of  $e_{max}$  shown in the lower curve of Figure 50 for higher H<sub>2</sub>O content. Therefore, we are led to the conclusion that, for the  $h^*$ ,  $T_0$ ,  $p_0$  and  $A_e/A^*$  characteristic of first generation technology, GDL's can operate with high H<sub>2</sub>O content, but with severe penalties in efficiency. I.e., the percentage loss in  $G_0$  and  $e_{max}$  is very large as  $X_{H_2O}$  is increased from 0.01 to 0.1.

On the other hand, high values of  $x_{H_2O}$  appear to be much more compatible with second generation technology (lower  $h^*$ , higher  $T_0$ ,  $p_0$  and  $A_e/A^*$ ). This is clearly shown by the upper curves of Figures 49 and 50, which typify this newer technology. For  $A_e/A^* = 50$ ,  $h^* = 0.3\text{mm}$ , and  $T_0 = 1800^\circ\text{K}$ , the theoretical results shown in Figure 49 imply that peak gain is maximum for  $x_{H_2O} = 0.025$ , and that this maximum is fairly flat for  $x_{H_2O}$  from 0.01 to 0.06. Indeed, a more detailed study of the theoretical results reveals that, for the stronger expansions associated with the second generation nozzles, the lower laser level as well as the upper level tends to freeze inside the nozzle. Hence, more  $H_2O$  is necessary to promote rapid equilibration of the lower level with the translational energy of the gas. This effect is shown in Figure 51, which illustrates the variations of the upper and lower laser level vibrational temperatures,  $T_{001}$  and  $T_{100}$ , respectively, as a function of distance for several different values of  $x_{H_2O}$ . Note that for  $x_{H_2O} = 0.01$ , the lower level is far from equilibrated, and that values on the order of  $x_{H_2O} = 0.04$  are needed to promote rapid equilibration. Therefore, we are led to conclude that second generation GDL's are more amenable to higher  $H_2O$  content, and that a wider range of fuels for GDL's is now a possibility.

The gain profiles are markedly different between high and low  $H_2O$  content. This is shown in Figure 52, where  $G_0$  is given as a function of distance downstream of the nozzle exit. In comparison to the case for  $x_{H_2O} = 0.01$ , note in Figure 52 that the peak  $G_0$  for  $x_{H_2O} = 0.04$  occurs nearer the nozzle exit, and that gain drops off

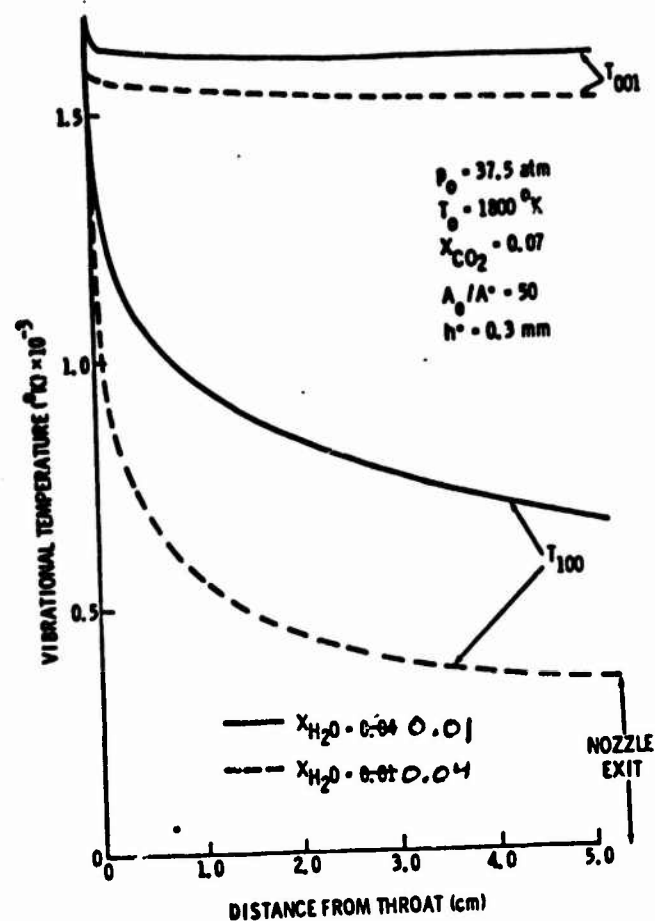


Fig. 51  
 Vibrational temperature distributions  
 inside the nozzle for two different  
 values of  $x_{\text{H}_2\text{O}}$ .

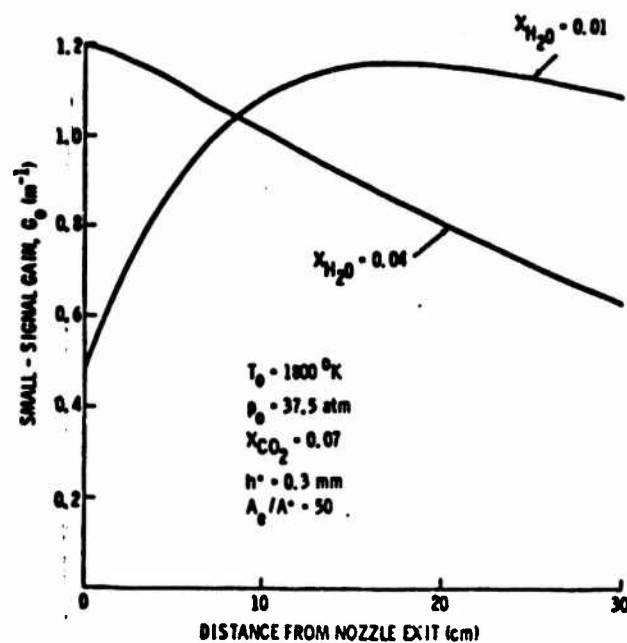


Fig. 52

Gain distributions downstream of the nozzle exit for two different values of  $X_{\text{H}_2\text{O}}$ .

more rapidly with distance. This implies a constraint on the laser cavity design for mixtures with high  $H_2O$  content, namely, that power has to be extracted in shorter distances. However, such rapid power extraction appears feasible, for example, with an unstable resonator, as described by Gerry<sup>1</sup>, and as discussed in a subsequent section of these Notes.

The results shown in Figures 49-52 are theoretical, and may be a bit optimistic. The kinetic rates embodied in these results are obtained from Taylor and Bitterman<sup>38</sup>, with the lower laser level deactivation rate due to  $H_2O$  modified to account for the calculations of Sharma<sup>46</sup>. (See Section I-D of the present Notes.) They do not include the up-dated rates described in References 25 and 26, and reproduced in Appendices A and B of the present Notes. The effect of the newer rates on such calculations, along with a comparison with the experimental data of Vamos<sup>15</sup>, is shown in Figures 53 and 54. Vamos has conducted a systematic series of shock tunnel tests covering 1st generation (Figure 53) GDL's (20:1 nozzle area ratio), as well as 2nd generation (Figure 54) GDL's (50:1 nozzle area ratio). In both Figures 53 and 54, the theoretical and experimental results for small-signal gain show that  $G_0$  persists at high  $H_2O$  content. Therefore, even though the results of Figures 49-52 may be slightly optimistic, the trends and conclusions shown are still valid.

### C. INCREASED TEMPERATURE

The obvious advantage of increasing the reservoir temperature,  $T_0$ , of GDL's is that the reservoir vibrational energy per unit mass

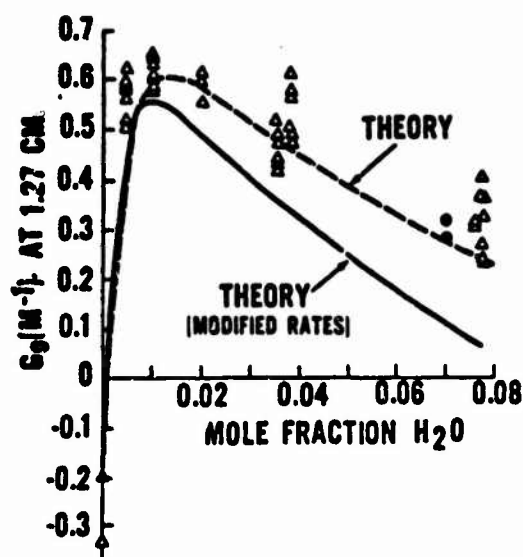


Fig. 53 Effect of water vapor on small-signal gain. Location 1.27 cm downstream of nozzle exit. Gas mixture  $\text{CO}_2/\text{N}_2/\text{H}_2\text{O}$ : 7/89.5/3.5 mole percent, 20:1 area ratio nozzle, 1 mm throat height, stagnation conditions 1800°K and 20 atm.

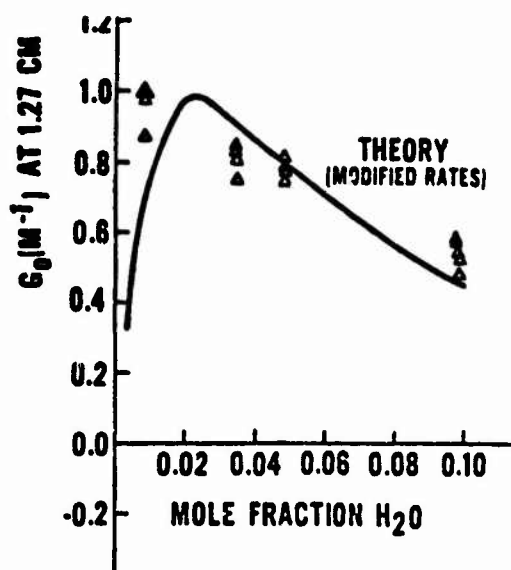


Fig. 54 Variation of small-signal gain with water vapor content. Location 1.27 cm downstream of nozzle exit. Seven mole percent  $\text{CO}_2$ , stagnation conditions 1800°K and 37.5 atm. Water production by addition of  $\text{H}_2$  and  $\text{O}_2$ .

increases. On the other hand, a disadvantage of increasing  $T_0$  is that collisional deactivation becomes more rapid, and therefore not all of the increased reservoir vibrational energy is realized at the nozzle exit. Another disadvantage is increased heating of GDL components. However, increasing  $T_0$  is certainly a viable means of increasing output power per unit mass flow, and high temperatures are therefore a major characteristic of second generation GDL's. Because the nozzle exit temperature should be low ( $T_{\text{exit}}=300^\circ\text{K}$ ) in order to keep the lower laser level population low, then increasing  $T_0$  automatically implies increasing  $A_e/A^*$ . For GDL's that exhaust to the atmosphere with a fixed diffuser efficiency, this also automatically implies increasing  $p_0$ . Therefore, in light of the above discussion, the reasons are clear for choosing the conditions which contrast the first and second generation technology in both Figures 49 and 50.

The purpose of this section is to discuss the results of a numerical experiment which indicate the advantages of increasing  $T_0$ . These results are shown in Figure 55, where  $G_0$  and  $e_{\text{max}}$  are plotted versus  $T_0$ . For each numerical point shown,  $A_e/A^*$  is different; the area ratio is increased as  $T_0$  increases in order to maintain  $T_{\text{exit}}=300^\circ\text{K}$ . For the sake of consistency, the reservoir pressure is held fixed at 30 atm for these points, i.e., the GDL is assumed to exhaust to a variable back pressure generally less than 1 atm.

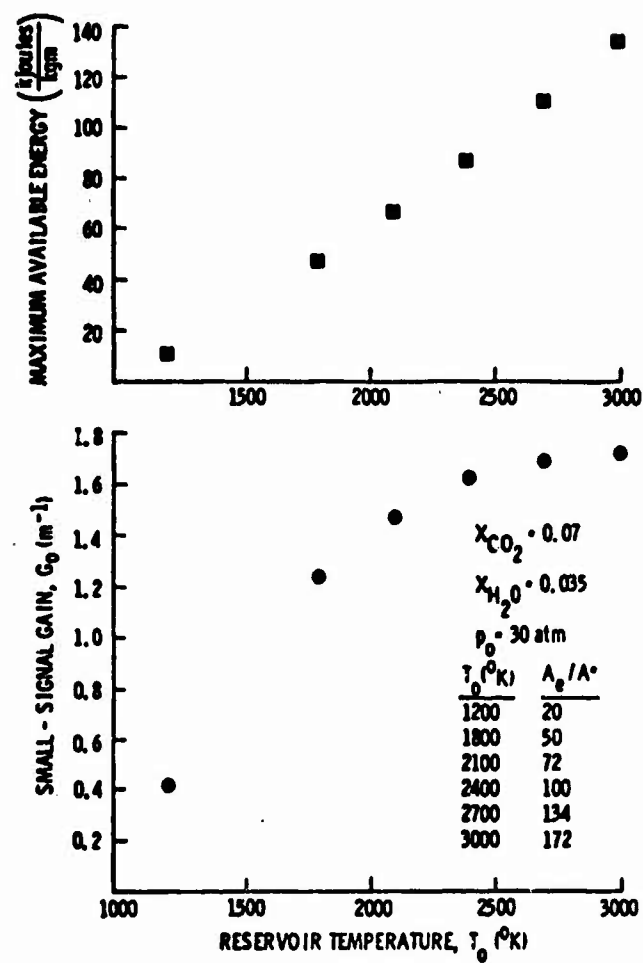


Fig. 55  
Effects of increasing  $T_0$  on peak gain  
and maximum available energy.



Examining Figure 55, the improvements brought about by increasing  $T_0$  from 1200 to 1800°K are clearly seen; peak  $G_0$  is dramatically enhanced, and  $e_{\max}$  increases by a factor of five. This is typical of the improvements incurred with second generation technology.

Now, let us postulate a third generation technology where  $T_0$  is further increased to 2400°K and  $A_e/A^* = 100$ . Here, the improvements are not so striking;  $G_0$  is beginning to plateau due to increased collisional deactivation, and the increase in  $e_{\max}$  is less than a factor of two between  $T_0 = 1800$  and 2400°K. Also, recall that all the points shown in Figure 55 are for  $p_0 = \text{constant} = 30$  atm. If our postulated third generation GDL exhausts to 1 atm, then  $p_0$  would have to be higher than 30 atm to overcome the increased total pressure losses associated with higher Mach number flows. An increase in  $p_0$ , by itself, causes increased collisional deactivation in the flow, and therefore the actual improvements of third generation GDL's will be less than those shown in Figure 55. On the other hand, for GDL's that exhaust to pressures less than 1 atm, the full advantages shown in Figure 55 might be realized.

In light of the above discussion, the following conclusions are made. By increasing  $T_0$  much above 1800°K, only moderate improvements (factors of 2 or 3) are possible. However, these improvements can be important. Therefore, a third generation, very high temperature GDL may be worth further consideration. In the process, many important questions will have to be answered; for example, are there appropriate

fuels that yield a 3000°K combustion temperature, and how difficult will it be to maintain the critical elements of GDL hardware at these temperatures?

#### D. BINARY SCALING

Gerry<sup>1</sup> and Greenberg et al<sup>50</sup> have pointed out that current GDL's can be scaled according to the parameter  $p_0 h^*$ . This is anticipated because two-body collisional deactivation dominates the kinetics. The purpose of this section is to examine in more detail the implications of binary scaling on GDL flows.

Figures 56 and 57 contain numerical results for peak  $G_0$  and  $e_{\max}$ , respectively, plotted versus  $p_0 h^*$  for a set of GDL nozzle flows with the same mixture ratio, nozzle contour,  $T_0$  and  $A_e/A^* = 20$ . Figures 58 and 59 contain similar results, except that  $A_e/A^* = 50$ . In each figure, only  $p_0$  and  $h^*$  are varied as shown. Clearly, the peak  $G_0$  and  $e_{\max}$  are unique functions of the  $p_0 h^*$  product, thus explicitly demonstrating the binary scaling. In addition, several trends are important to note, as follows.

(1) The variation of  $G_0$  and  $e_{\max}$  with  $p_0 h^*$  is not linear, i.e., halving the  $p_0 h^*$  does not necessarily double the gain or  $e_{\max}$ . This is particularly true for  $G_0$  at low values of  $p_0 h^* < 1$  atm-cm, as seen in Figures 56 and 58.

(2) Figures 56 and 58 show that  $p_0 h^* = 1$  atm-cm is a reasonable value of the binary scaling parameter for high gain. This value has been stated earlier by Greenberg<sup>50</sup>. In the same vein, Gerry<sup>1</sup> has pointed out a criterion for adequate freezing of the

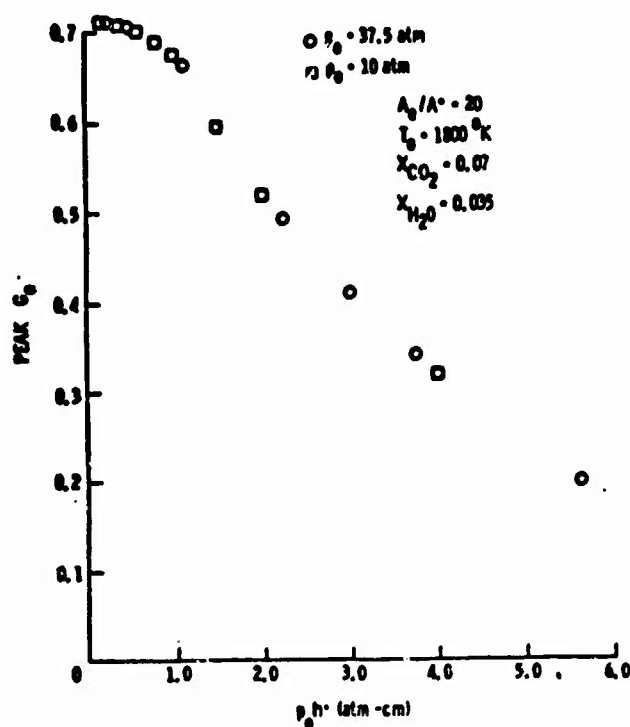


Fig. 56  
Binary scaling of gain for a low area ratio nozzle.

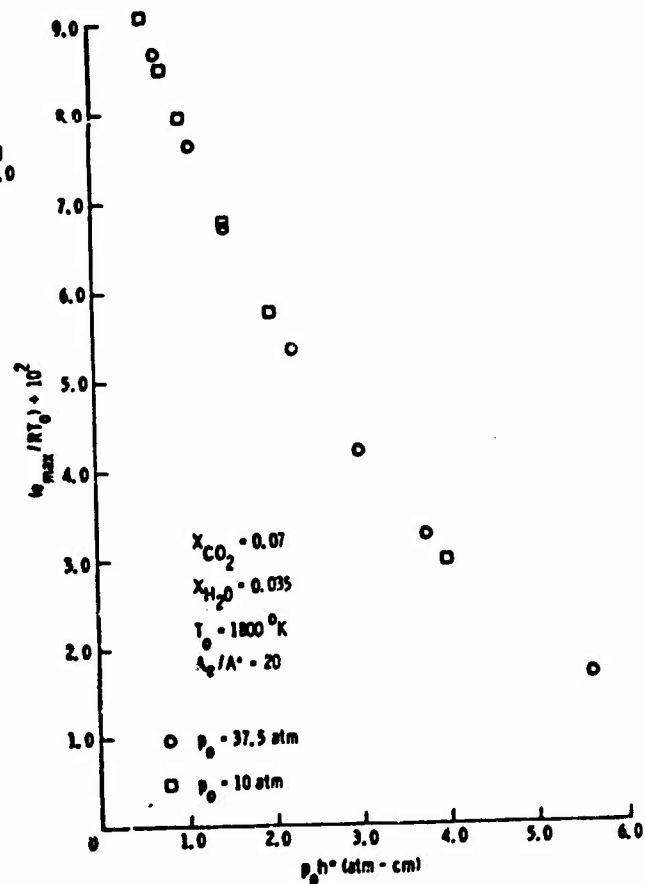


Fig. 57  
Binary scaling of maximum available energy for a low area ratio nozzle.

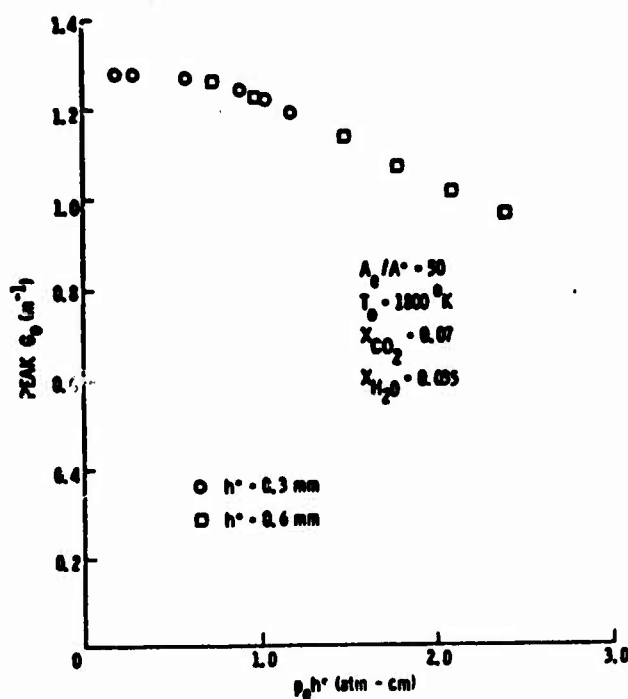


Fig. 58.  
Binary scaling of gain for a high area ratio nozzle.

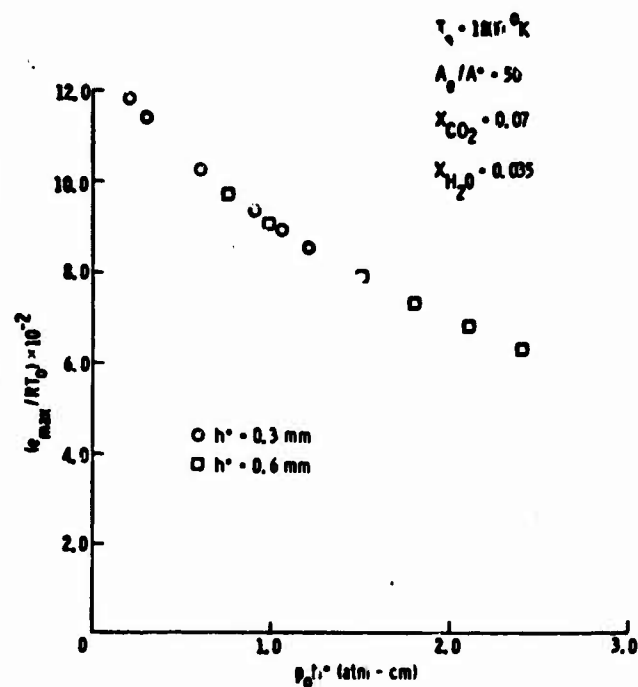


Fig. 59  
Binary scaling of maximum available energy for a high area ratio nozzle.

nozzle flow, namely, that  $p_0 h^* < 2(p\gamma_{eff})_{T^*} u^*$ . This criterion is simply a statement that, in the throat region, the flow residence time,  $h^*/u^*$ , should be less than the effective relaxation time,  $(p\gamma_{eff})_{T^*}/p^* \approx (p\gamma_{eff})_{T^*}/0.5p_0$ . For the flow conditions in Figures 56-59,  $2(p\gamma_{eff})_{T^*} u^* \approx 1.25$  atm-cm; hence, a value of  $p_0 h^* \approx 1$  atm-cm satisfies the above criterion.

(3) Major increases in  $G_0$  can not be obtained by reducing  $p_0 h^*$  below 1 atm-cm. This is clearly seen in Figures 56 and 58, where  $G_0$  essentially reaches a plateau for  $p_0 h^* < 1$  atm-cm. The basic reason for this behavior is that, for low values of  $p_0 h^*$ , both the upper and lower laser levels tend to freeze in the nozzle expansion. In fact, in the theoretical limit of  $p_0 = 0$ , hence  $p_0 h^* = 0$ , both the upper and lower laser levels would freeze at their equilibrium reservoir values, no population inversion would exist anywhere in the flow, the gain would be negative and  $e_{max}$  would be zero. These trends are illustrated in Figure 60, which gives the vibrational and translational temperatures for  $p_0 h^* = 0.21$  atm-cm (solid lines) and 1.2 atm-cm (dashed lines) as a function of distance from the nozzle exit. First, consider the solid lines. For  $p_0 h^* = 0.21$  atm-cm, the tendency for  $T_{100}$  to "hang up" is quite evident. Indeed, a downstream distance of more than 30 cm is required before  $T_{100}$  equilibrates with  $T$ . At 30 cm, the peak gain of  $1.28 \text{ m}^{-1}$  is finally achieved. In comparison, consider the dotted lines for  $p_0 h^* = 1.2$  atm-cm. The upper level vibrational temperature,  $T_{001}$ , is less than the previous case; by itself, this will reduce  $G_0$ . However,  $T_{100}$  has relaxed quite rapidly and is

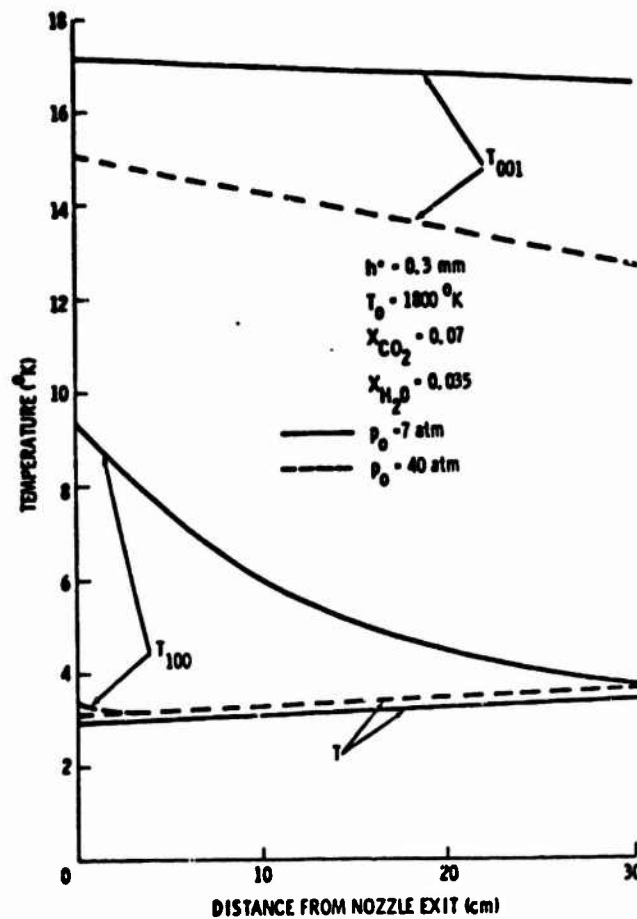


Fig. 60

Temperature distributions downstream of the nozzle exit for two different values of  $p_0$ ;  $A_e/A^* = 50$ .

essentially equilibrated near the nozzle exit; this will favor the gain. For this case, a peak  $G_0$  of  $1.2 \text{ m}^{-1}$  is achieved near the nozzle exit.

With these trends in mind, there appears to be little benefit in striving for exceptionally small values of  $p_0 h^*$  in gasdynamic lasers. Indeed, it appears to be sufficient to satisfy the criterion,  $p_0 h^* < 2(p\tau_{\text{eff}})_T u^*$ .

#### E. CARBON MONOXIDE GDL

In our discussion of modern advance in gasdynamic lasers, we would be remiss not to mention specifically the pioneering work of McKenzie<sup>61</sup> with carbon monoxide. All previous sections of these Notes have dealt exclusively with  $\text{CO}_2\text{-H}_2\text{-H}_2\text{O}$  or  $\text{CO}_2\text{-H}_2\text{-He}$  mixtures, with the lasing transition at  $10.6\mu$ . However, this is by no means the only possibility for gasdynamic lasers. McKenzie has reported independent experimental and theoretical results for population inversions and laser power extraction in rapidly expanding  $\text{CO-H}_2\text{-Ar}$  mixtures. The details are clearly explained in Reference 61, and hence no elaboration will be given here. However, the following important points are emphasized. The molecular kinetics of  $\text{CO-H}_2\text{-Ar}$  mixtures rely upon the freezing of vibrational energy in  $\text{H}_2$  and  $\text{CO}$ , both of which have unusually long relaxation times. Furthermore, vibrational energy is pumped from  $\text{H}_2(v=1)$  to  $\text{CO}(v=1)$ , similar to the conventional  $\text{CO}_2\text{-H}_2$  system. However, the similarity stops there, because the vibrational energy is rapidly distributed upward to the higher lying levels of  $\text{CO}$  due

to rapid vibration-vibration (V-V) transfer. The anharmonicity of these upper levels promotes the rapid V-V transfers, as discussed by Treanor et al<sup>64</sup>. The net result is a non-Boltzmann distribution of molecules among the upper CO vibrational levels. This distribution may lead to a vibrational population inversion in the usual sense (more particles in an upper vibrational level than a lower level); or more likely it will result in a partial inversion for a given rotation-vibration transition, even though a total vibrational inversion does not exist. Moreover, the CO gasdynamic laser generally emits simultaneously at a number of wavelengths in the  $5\mu$  range. All these points may add up to an order of magnitude improvement of CO over conventional  $\text{CO}_2\text{-H}_2$  GDL systems in terms of power output per unit enthalpy flux of the flow<sup>61</sup>.

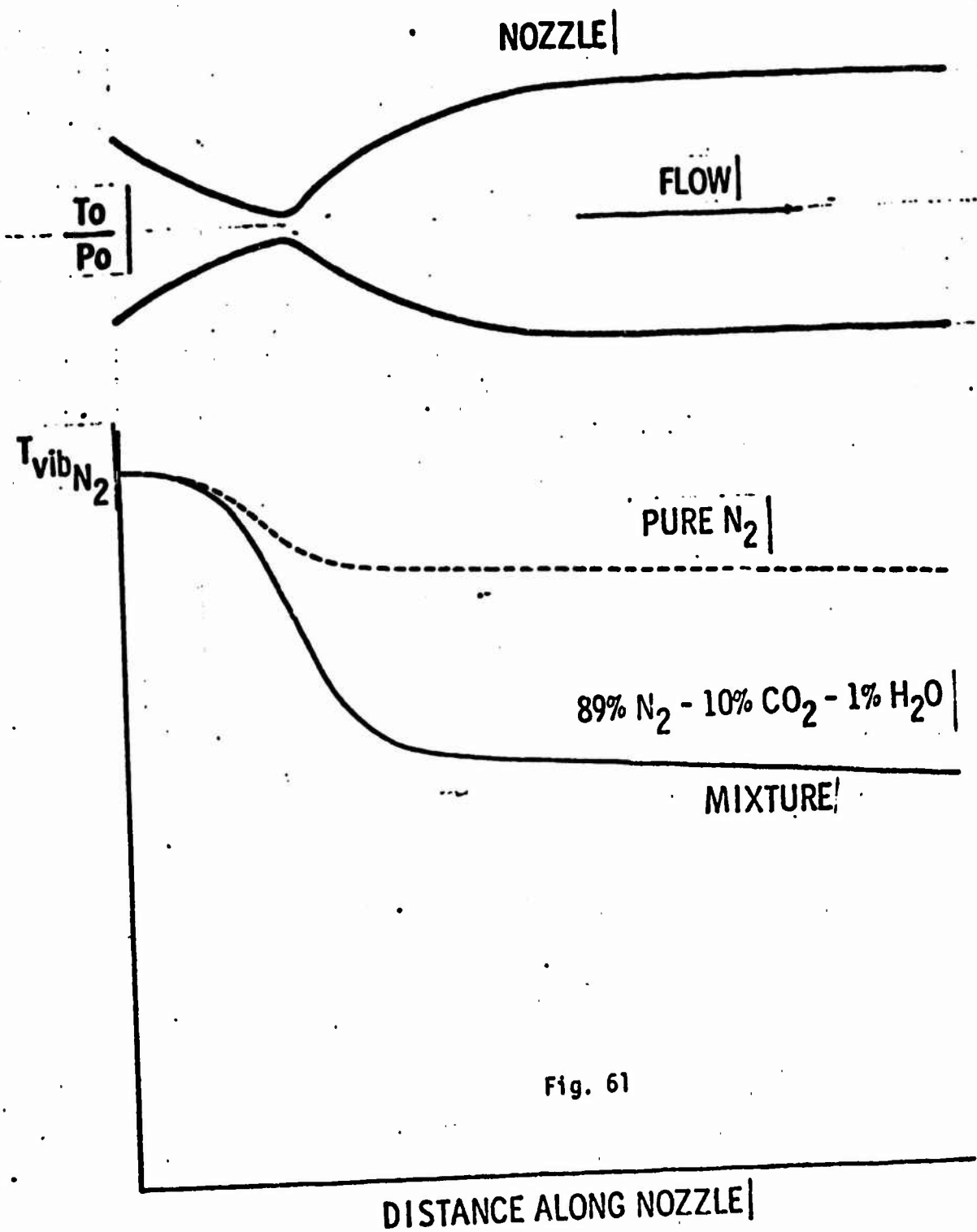
The CO gasdynamic laser suffers from one practical disadvantage -- the requirement for high Mach number flows. The population inversions in CO are enhanced by very low translational temperatures of the gas, on the order of 60°K. In order to achieve such a low temperature, the flow must be expanded in supersonic nozzles with area ratios (exit to throat area) on the order of 1000 -- a factor of 20 larger than conventional GDL's. To an aerodynamicist, this implies high Mach number flows with large total pressure losses. Since many practical applications of GDL's involve exhausting the gas to the atmosphere, then either extremely high reservoir pressures are required, or a dramatic breakthrough in supersonic diffuser technology is necessary. This amounts to a serious limitation on the practical use of such lasers.



## F. DOWNSTREAM MIXING GASDYNAMIC LASERS

How do we squeeze the most out of the gasdynamic laser concept? The answer to this question may rest in some recent work on downstream mixing GDL's, which represents the frontier of gasdynamic laser research today.

Consider a conventional  $\text{CO}_2\text{-H}_2\text{-H}_2\text{O}$  or He GDL as discussed in these Notes. Emphasis is made that the primary reservoir of energy for laser extraction is in the vibrationally excited  $\text{N}_2$ , even though the laser emission itself occurs via the  $\text{CO}_2$  molecules. Of course, one purpose of the supersonic nozzle expansion is to freeze as much of this vibrational energy as possible. Pure  $\text{N}_2$  has an extremely long relaxation time; hence it readily freezes in a rapid expansion. However, in a conventional GDL where both  $\text{CO}_2$  and  $\text{H}_2\text{O}$  (or He) are present in addition to  $\text{N}_2$  in the nozzle expansion, such molecules act as a contaminant to the  $\text{N}_2$ . As a result, the  $\text{CO}_2\text{-H}_2\text{-H}_2\text{O}$  or He mixture relaxes faster than pure  $\text{N}_2$ , giving lower vibrational temperatures, hence lower available laser power. This is shown schematically in Figure 61. In addition to this consideration, to obtain maximum laser power, the reservoir temperature,  $T_0$ , should be made as high as possible. The higher the temperature, the more vibrational energy is present in the gas and subsequently more laser power can be obtained. However, in conventional GDL's,  $T_0$  is limited to values around  $2300^\circ\text{K}$ ; above this temperature,  $\text{CO}_2$  begins to chemically dissociate, and laser performance begins to deteriorate. This is in contrast to the dissociation of  $\text{H}_2$ , which occurs above  $4000^\circ\text{K}$ .



In light of the above, the reader can clearly see two major advantages in constructing a gasdynamic laser which expands pure  $N_2$  through a supersonic nozzle, and then mixes  $CO_2$  and  $H_2O$  or He downstream of the nozzle exit. Here:

- (1) Reservoir temperatures can exceed  $4000^\circ K$ , and
- (2) More efficient freezing of the  $N_2$  vibrational energy is obtained.

Such a device is called a downstream mixing gasdynamic laser, and is shown schematically in Figure 62. If the ideal situation of instantaneous mixing is assumed, then for the conditions shown in Figure 62, a non-equilibrium calculation using the method of Reference 62 indicates a maximum available power of over  $300 \text{ KJ/lb}_m$ . This is an order of magnitude improvement over the existing 2<sup>nd</sup> generation GDL's discussed in Section II above. In fact, this number is compared with other laser concepts in Figure 63, which clearly indicates why there is current interest in such a device.

However, there are obvious problems. Mixing does not occur instantaneously, and throughout the finite mixing region of a real flow, vibrational deactivation will constantly decrease the available power. The question is: Does enough deactivation occur during mixing to negate the whole concept? Work is being done to answer this question, as described below. There are other problems. For example, can the nozzles be made of materials that can withstand such high temperatures in the small nozzle throats? How can we produce  $N_2$  at  $4000^\circ K$  on a continued, practical basis? Also, recall that high Mach number nozzles

# DOWNSTREAM MIXING GASDYNAMIC LASER

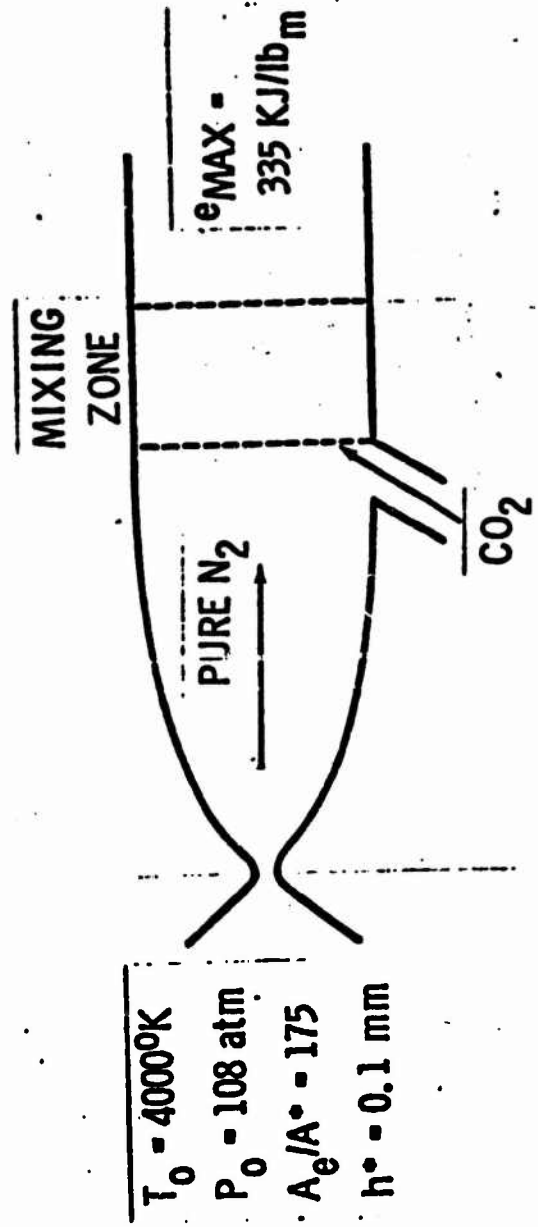


Fig. 62

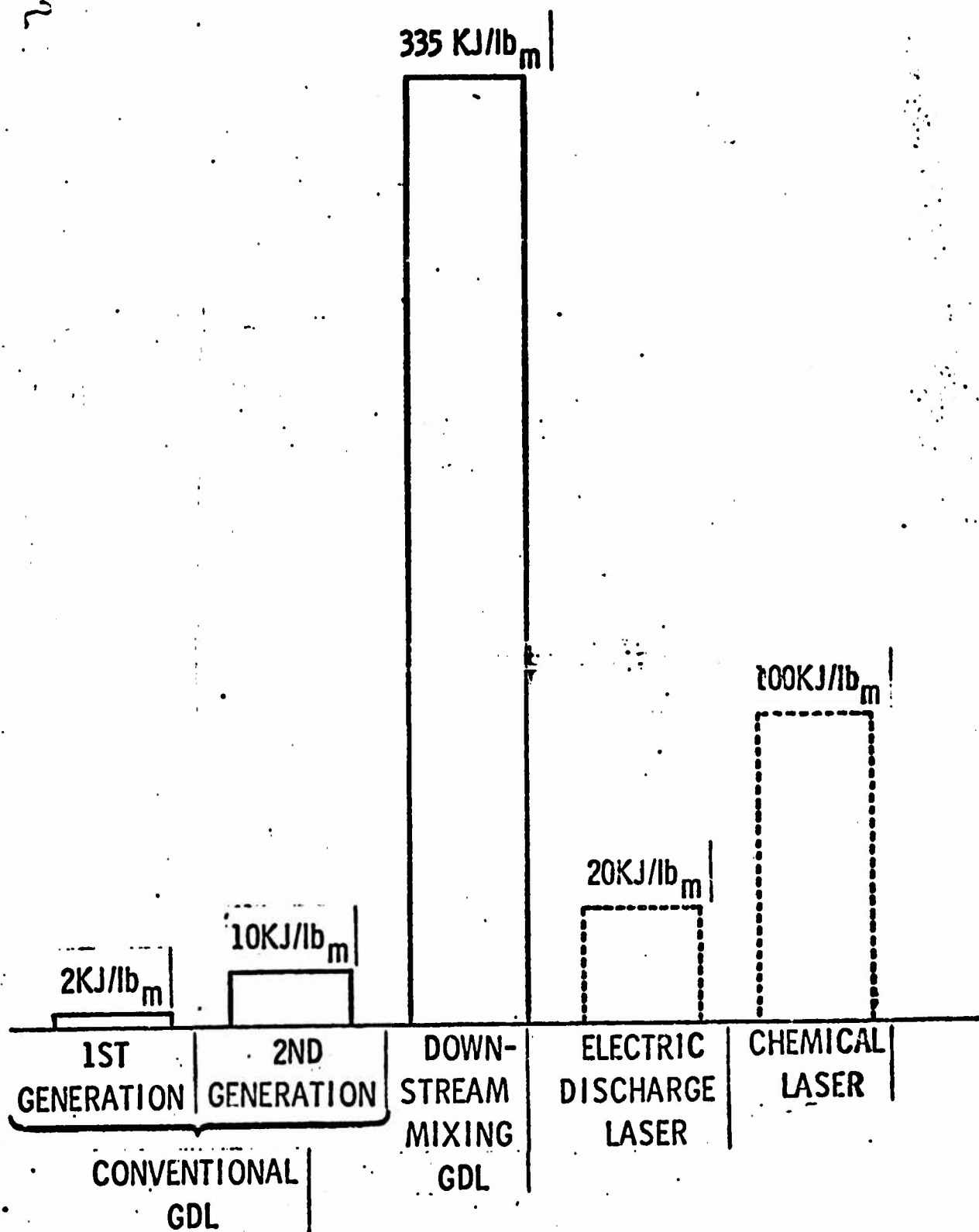


Fig. 63

are required to insure that the gas translational temperature (hence the lower laser level population) in the cavity will be low. Hence, can diffusers be developed that will allow exhausting the flow to the atmosphere? Can the flows be mixed without inducing strong shock waves or major turbulence in the laser cavity that degrade beam quality?

The advantage of high power output obtained in a downstream mixing GDL encourages work on this concept, even in the face of the above problems. Some early experimental work has been performed by Bronfin et al<sup>65</sup> using arc-heated  $H_2$  with  $CO_2$ -He injected vertically into the supersonic flow in the cavity. Their results were the first to demonstrate the potential of the downstream mixing concept. However, this work was not pursued, presumably due to concern about shock waves, hence poor beam quality, in the cavity. More recently, downstream mixing GDL experiments using tangential mixing have been reported by Milewski et al<sup>66</sup> in a shock tube. (Note: Reference 68 contains more recent data than Reference 67.) Also, Howgate et al<sup>52</sup> report some similar measurements with  $CO_2$  injected both at the nozzle exit and upstream of the throat. However, the most complete investigation by far has been conducted by the team of Borghi and Charpenel<sup>69</sup>, who have performed detailed vibrational nonequilibrium flow field calculations of tangential downstream mixing using a finite-difference solution of the turbulent boundary layer equations, and of Taran, Charpenel and Borghi<sup>70</sup>, who report a systematic series of arc-tunnel experiments complementing the theoretical predictions. Some

of the results of Taran et al<sup>70</sup> are shown in Figures 64-68. They examined mixing downstream of the nozzle exit (Figure 64) as well as mixing in the throat region (Figure 65). Theoretical results for gain profiles are shown in Figure 66 for mixing downstream of the exit, and in Figure 67 for mixing in the throat region. Clearly, mixing in the throat region shows higher gains by an order of magnitude. This should not be construed as a general result; rather, it is due to the investigator's choice of mixing a high Mach number stream of  $N_2$  with a low Mach number stream of  $CO_2$ , as shown in Figure 64. As a result, a considerable amount of the high total temperature of the  $N_2$  stream was recovered in the cavity, leading to high static temperatures (800-1000°K), hence low gains. This choice of mixing high and low Mach number streams was made to enhance the mixing process. Such a high temperature recovery was not obtained in the scheme shown in Figure 65. These theoretical results were reasonably confirmed by arc-tunnel results, exemplified by the experimental data shown in Figure 68. The reader is urged to study References 69 and 70 for a full exposition of these studies. They represent the frontier of the state-of-the-art. In fact, for the reader's convenience, Reference 70 is reproduced as Appendix C of the present Notes.

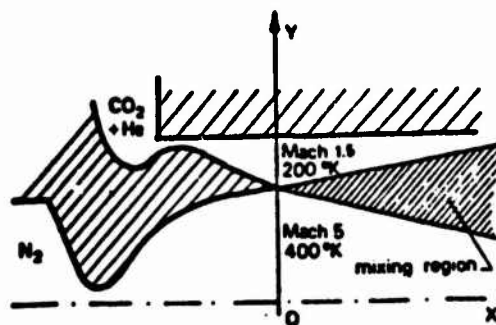


Fig. 64 - Diagram of a supersonic mixing nozzle with  $\text{CO}_2$  injection after expansion of  $\text{N}_2$ .

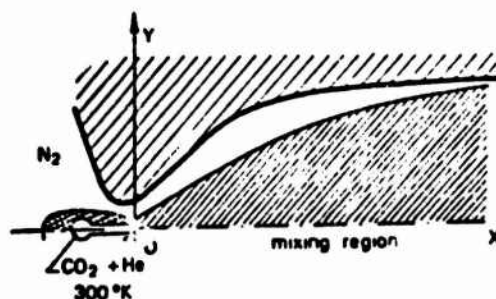


Fig. 65 - Diagram of a nozzle with injection at the throat.



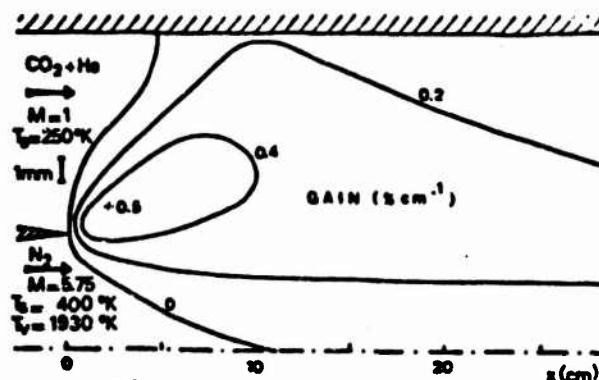


Fig. 66 - Gain distribution for supersonic mixing of a Mach 5.75, 400°K. static temperature and 1930°K vibrational temperature  $N_2$  flow with a 10%  $CO_2$ , 90% He flow at Mach 1 and 250°K. Gain was calculated for the P 30 line (optimum gain is slightly larger for lines P 22 - P 26).

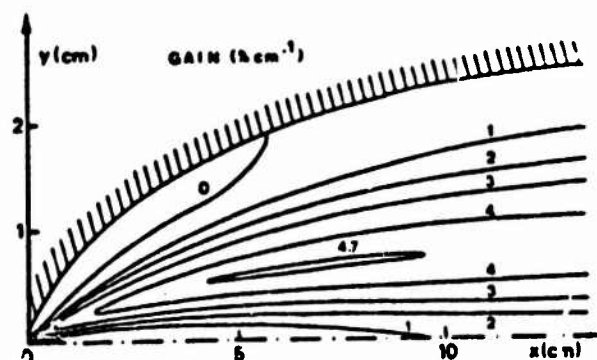


Fig. 67 - Gain distribution on the P 16 line for mixing at the throat. The stagnation conditions for  $N_2$  are 2500°K and 15 atm. The 30%  $CO_2$ , 70% He mixture is at room temperature; the half slot height of the injector is 0.3 mm. The throat height for the  $N_2$  (between the injector and one nozzle wall is 0.7 mm). Flow proportions are 44%  $N_2$ , 39% He, 17%  $CO_2$ .

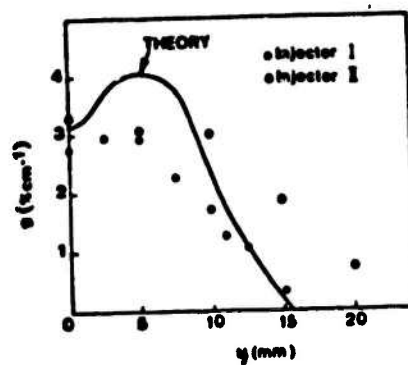


Fig 68 - Gain distributions across the nozzle,  
at  $x = 15$  cm downstream from the  
throat.

### III OPTICAL CAVITY CONSIDERATIONS AND FLUID DYNAMIC PROBLEMS

#### A. INTRODUCTION

To this point we have discussed the many facets of GDL's which bear on population inversion, small-signal gain and maximum available power. To a lesser extent, some of the aspects of power extraction were considered in Section IC. However, power extraction is more than just solving the radiative transfer equation,  $dI/I = G dy$  between mirrors in the cavity, coupled with the nonequilibrium supersonic flow. It is also a matter of considering the optical design of the cavity, taking into account the actual path of the light rays (geometric optics), mirror losses (such as absorption), diffraction (physical optics), and the density inhomogeneities of the flowing gas which cause phase distortions in the laser beam. In essence, the basic philosophy of optical cavity design is stated by Clark<sup>71</sup>: "Achieve the maximum output power in a beam with minimum divergence, limited only by diffraction." Such considerations are the subject of this section.

Also, emphasis is made that the optical phase distribution across the output beam from a laser cavity should be constant (uniphase), and that the beam divergence angle should be as small as Nature allows (limited only by diffraction through the output aperture). For these conditions, the laser beam can be focused to a spot of minimum diameter. Any deviation from these conditions will reduce the beam intensity in the far field.

## B. CAVITY TYPES

### 1. Amplifiers

The first generation of GDL's have extracted power by using the cavity as an amplifier, such as shown in Figure 69. Here, an independent beam from a CO<sub>2</sub> laser (usually a "conventional" electric discharge laser) is fed into the GDL cavity through an input aperture. This CO<sub>2</sub> laser is called the Master Oscillator (MO). The beam is then reflected back and forth inside the GDL cavity for several passes, being amplified by the laser medium on each pass. On the last pass, the beam leaves the cavity either through small holes in the output mirror or through some type of window. At present, extracting the last pass through a solid window is impractical because current window materials can not tolerate the high heating loads imposed by the high power beam. This leads to the use of aerodynamic windows, to be discussed later. Referring again to Figure 69, the cavity is acting as a power amplifier (PA), and the whole arrangement of oscillator and cavity is called the Master Oscillator Power Amplifier (MOPA). The number and arrangement of passes through the cavity depend on the designer's intentions; several possible geometries are shown in Figure 69, which is taken from Reference 71.

There are three major advantages of the MOPA for extracting power:

- (a) The input beam from the Master Oscillator, assuming it is properly designed, is already in constant phase. Hence, if the

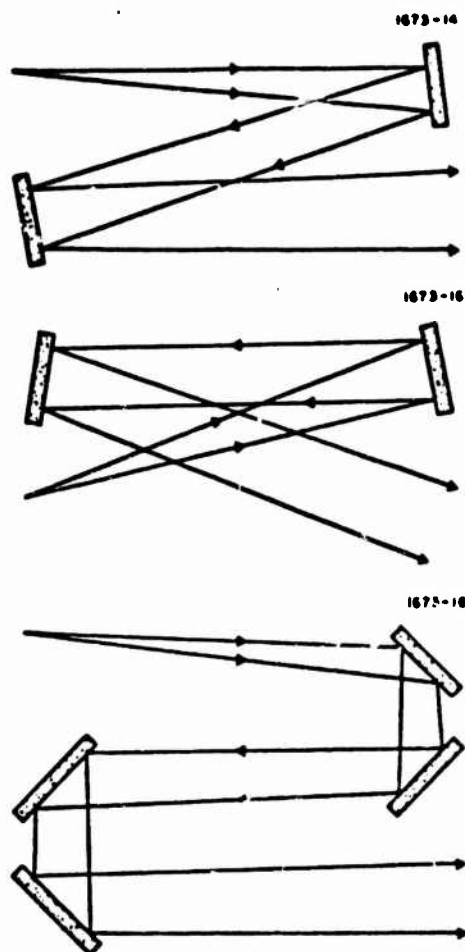


Fig. 69 Typical amplifier folding geometries.

amplifier medium in the cavity is homogeneous, then the output beam should be of constant phase also.

(b) The power level of the output beam of a MOPA can be readily increased or decreased simply by controlling the input beam from the MO. This adds a certain flexibility to GDL operation.

(c) The timewise (temporal) variation of the output beam can also be controlled in a similar manner.

Referring again to Figure 69, a disadvantage of the MOPA is that most of the power available in the supersonic gas in the cavity is extracted only during the last beam pass; the role of the other passes is simply to build up the intensity so that the last pass reaches saturation intensity. At saturation intensity, the beam is extracting energy from the  $\text{CO}_2$  molecules just as fast as the  $\text{H}_2$  can pump energy into the upper laser level (001) of  $\text{CO}_2$ . In the meantime, during the earlier beam passes that occur upstream of the last, saturating pass, available laser energy in the gas is being lost due to collisional deactivation of the molecules. Hence, a MOPA arrangement is in general an inefficient way of extracting the available laser energy.

## 2. Resonators

A resonator is a self-contained extraction device, where the laser radiation is initially triggered by random spontaneous emission and then rapidly increased by stimulated emission in a direction perpendicular to mirrors on both sides of the cavity. Three types of resonators are shown in Figure 70, taken from Reference 71. Resonators have the advantage of rapidly building up saturation intensity within

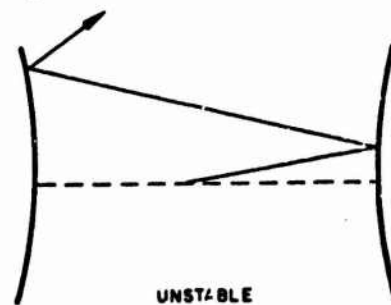
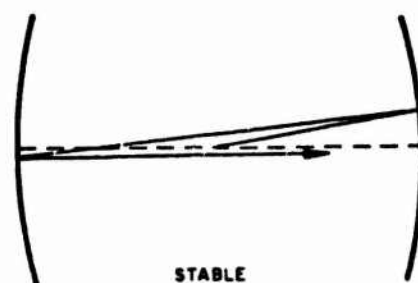
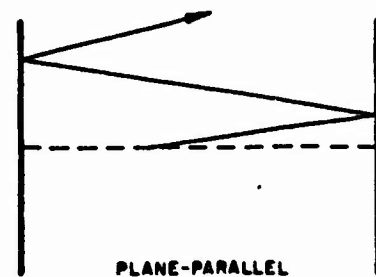


Fig. 70 Types of Laser Resonators.

the cavity, hence being more efficient in general than the MOPA discussed above. They have the disadvantage of allowing no intensity control, and the optical alignment is more difficult than MOPA's. However, their efficient operation, which is related to their ability to extract energy in a short flow length, makes such resonators of extreme interest in GDL design.

There are basically three types of resonators, and they all have been used at one time or another on a GDL. These types are shown in Figure 70. The major distinction between them is that light rays which are slightly off-axis tend to "walk out" of the plane-parallel and unstable resonators, but are contained by the stable resonator.

Diffraction plays a very important role in determining what type of intensity pattern exists in the output laser beam which emerges from the output mirror. As stated by Clark<sup>71</sup>, to produce a phase coherent beam, all parts of the laser cavity should share energy through diffraction. In this way, the optical phases of all the emitting molecules are locked together through cross-coupling within the cavity, and a laser beam of the lowest order transverse mode will be produced. Some cavities do this job better than others. For example, a number of laser transverse modes can oscillate within a cavity, each producing a different intensity pattern in the output beam. The intensity patterns associated with twelve of these modes are shown in Figure 71, which is taken from Reference 72. The best quality laser beam is one



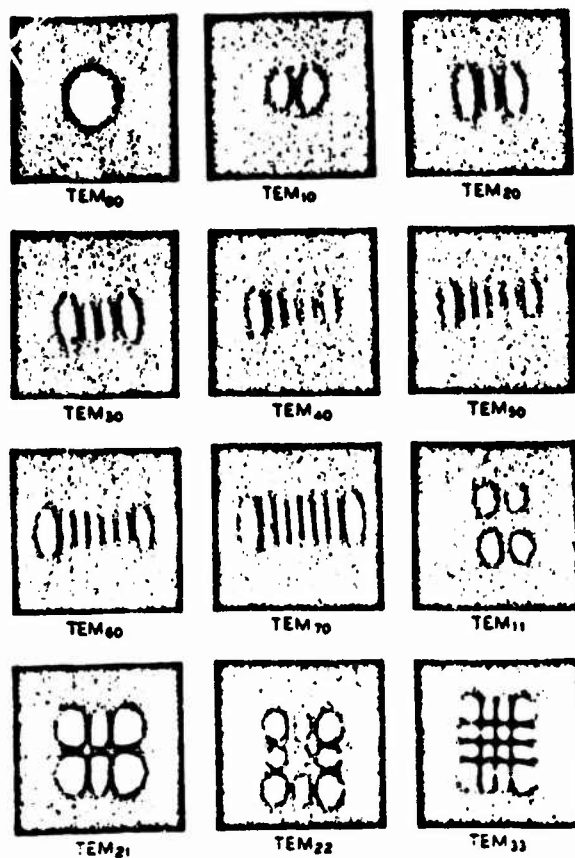


Fig. 71 Mode patterns of a gas laser oscillator (rectangular symmetry).

where a single mode is operating, with that mode being the lowest order  $TEM_{00}$  mode. (TEM means transverse electromagnetic mode.) This mode produces the single spot seen in the upper left corner of Figure 71. Unfortunately, it is very difficult to obtain single mode operation; indeed, most GDL's have in the past operated multi-mode.

What is the problem that causes multi-mode operation? First, consider a stable resonator, and define the Fresnel number,  $N_F$ , as  $N_F = r^2/d\lambda$ , where  $r$  = mirror radius,  $d$  = distance between mirrors and  $\lambda$  is the laser wavelength. Stable resonators with high and low Fresnel numbers are shown in Figure 72. Diffraction effects in the long cavity (the low Fresnel number cavity) are stronger; this can be seen by inspection of Figure 72 where a slightly off-axis ray effectively has a long enough distance between mirrors to cross-couple with large regions of the cavity.

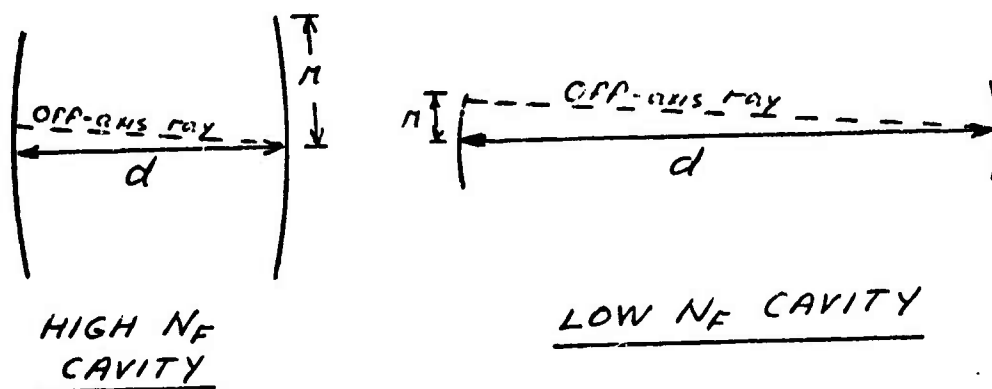


Fig. 72

Hence, a low Fresnel number cavity has a good chance of operating with the lowest order mode. On the other hand, again looking at

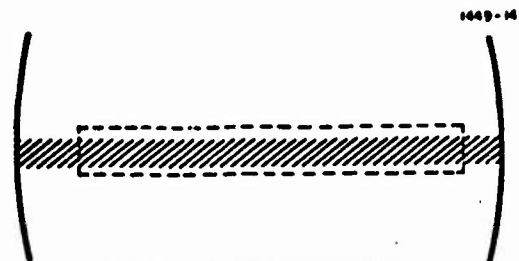
Figure 72, the opposite is true of a high Fresnel number cavity. This is also seen in Figure 73, taken from Reference 71. For a large  $N_F$ , the stable resonator can set up several independent modes of operation, with little cross-coupling by diffraction. Unfortunately, to handle the large mass flows characteristic of GDL's, the cavity has to be a fairly high Fresnel number cavity. A partial solution is to use an unstable resonator as shown in Figure 73. Even though  $N_F$  may be large, the rays of an unstable resonator spread out within the cavity, and provide the desirable strong cross-coupling. Hence, in an unstable resonator, it is more difficult for the higher order transverse modes to oscillate. For more details, the reader is urged to consult Reference 71.

#### B. CAUSES OF BEAM DISTORTION IN GDL's

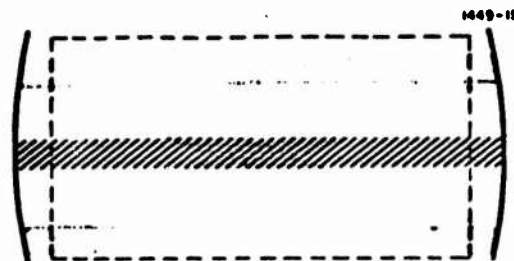
All of the above discussion has assumed that the laser medium (the supersonic flow in the cavity) is homogeneous. If the medium is not homogeneous, then additional sources of phase distortion are present. These additional sources are examined in the present section.

##### 1. Shock Waves

There are two principal sources of shock waves in the GDL cavity, and these are shown in Figure 74, taken from Reference 73. The nozzle of a GDL is really a bank of small nozzles in a row -- small nozzles to promote vibrational freezing in the expansion. This is shown in the top sketch of Figure 74, which looks down on the top view of a GDL. Here we see the minimum length contour of such nozzles,



(a) STABLE RESONATOR,  $N_F = 1$



(b) STABLE RESONATOR,  $N_F \gg 1$



(c) UNSTABLE RESONATOR,  $N_F \gg 1$

Fig. 73 Transverse mode selection for various resonator configurations.

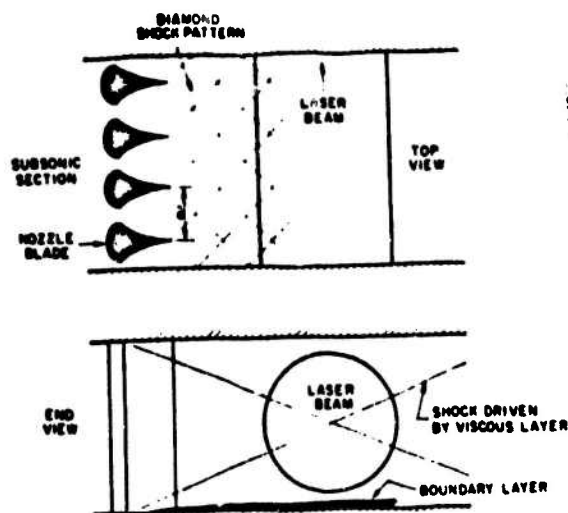


Fig. 74 GDL

as well as a diamond shock pattern coming from the nozzle tips. Flow is from left to right, and the laser beam is transverse to the flow as shown. The flow at the exit of each nozzle is not exactly parallel; this is due to truncation of the nozzles to obtain structural strength at the tips, and due to the boundary layer growth along the nozzle walls as well as the wake growth downstream of the tips. Hence, a diamond shock pattern is always a characteristic of such multi-nozzles, and was observed long before the advent of gasdynamic lasers<sup>74</sup>. A detailed survey of these disturbances, as well as other fluid dynamic aspects of gasdynamic lasers, can be found in the recent, excellent survey by Russell in Reference 75.

This diamond shock pattern is generally weak. Moreover, if the laser beam cuts across these shocks in the direction shown in the top of Figure 74, then the optical path will essentially be the same for each ray and phase distortion will be minimized. Hence,

the shocks emanating from the nozzle tips are not a major problem.

This is not the case for the shocks that come from the top and bottom walls of the nozzle array. Such shocks are shown in the bottom sketch of Figure 74. Here we are looking at a side view of the GDL, where the nozzle entrance, throat and exit are shown as the vertical lines. Flow is still from left to right. Consider the expansion in the nozzles. The pressure, density and temperature drop so rapidly in the nozzle throat region that the boundary layer displacement thickness on the flat top and bottom walls experiences an almost discontinuous increase. This appears as a compression corner to the flow, and triggers the two oblique shocks emanating from the top and bottom walls shown in Figure 74. Here, the rays of the laser beam are parallel to the plane of the shocks, and the optical length of the rays can vary substantially across the beam, depending on the density of the different regions of the shock pattern. As a result, these top and bottom shocks can cause substantial phase distortion.

There are two solutions to this problem. One is gasdynamic, and is discussed by Simons<sup>73</sup>. It involves the simple aspect of contouring the top and bottom walls in the nozzle throat region in such a fashion as to cancel the displacement thickness growth. This is illustrated in Figure 75, taken from Reference 73. However, precise contouring of the top and bottom walls is a serious fabrication complication for the construction of GDL's. A compromise is discussed by Director<sup>76</sup>, who shows experimentally that the oblique shock waves can be sufficiently mitigated by simply diverging the top and bottom

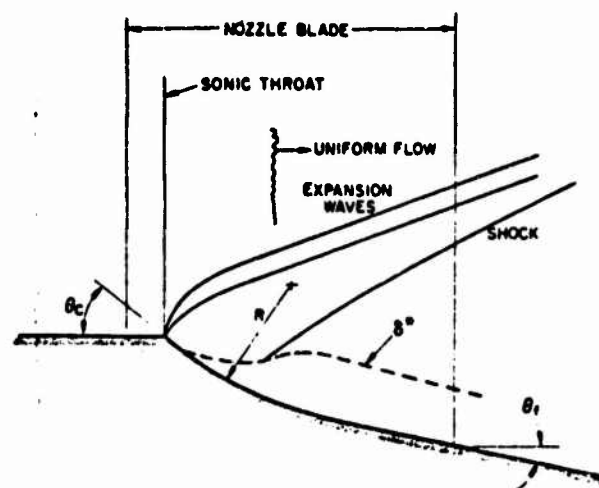


Fig. 75 GDL Wall Contour

walls by a constant small angle on the order of a degree or so.

The other solution is optical. Hoffman and Jones<sup>77</sup> have suggested the phase cancellation optical configuration shown in Figure 76.

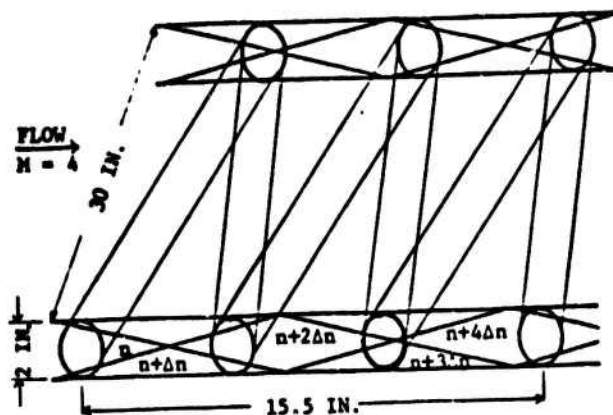


Fig. 76 Phase Cancellation Optical Configuration

This is characterized by a symmetric beam path arrangement wherein each ray cuts the shock waves an equal number of times and each pass traverses the flow at the same angle. Such an arrangement applies, of course, to the MOPA type of optical cavity design; it is not really applicable to resonators. This phase cancellation idea has led to an order of magnitude improvement in beam quality<sup>77</sup>, and is illustrated in Figure 77, obtained from Reference 75.

As a result of both the above solutions, the serious beam quality problems originally encountered with the cavity shock waves have gradually been minimized. In fact, in a properly designed "clean flow"



nozzle and cavity, random turbulence in the flow may be the limiting factor on beam quality instead of the shock waves.

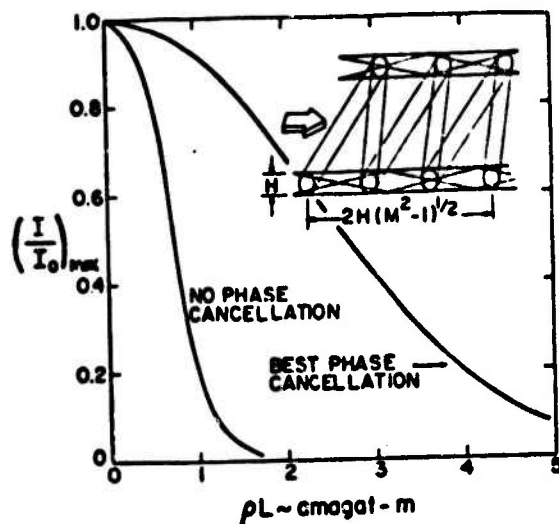


Fig. 77 Peak far field intensity at  $10.6\mu$  calculated from  $0.7\mu$  interferograms (from Reference 31).

## 2. Turbulence

There is not much that can be said about turbulence at the present time, and its quantitative effect on phase distortion. Given the extent and spectrum of the turbulence of the flow in the cavity, the analysis of Sutton<sup>78</sup> allows a calculation of its effect on the beam in the far field. However, a prediction of the turbulence level generated within the boundary layers and wakes, and that which propagates downstream from the reservoir and subsonic portions of the nozzles, is difficult to obtain. However, we can categorically state that random turbulence will always create a temporal phase change distortion in the beam, and that such turbulence can be the fundamental limiting

factor in obtaining the best beam quality .

### 3. Non-uniform Gain Profiles

Recall that small-signal gain in a GDL varies with distance as shown in Figure 33, and as sketched in Figure 78 for cases with and without power extraction. Clearly, gain varies through the cavity and across the laser beam. Such a non-uniform gain profile ultimately leads to a non-uniform intensity variation across the output beam. This is shown in Figure 79, obtained from Reference 71. Here, the intensity distribution of the input beam in a MOPA (a Gaussian profile) is compared with the corresponding output intensity distribution. Note that the upstream edge of the output beam (where gain is high) peaks to a very high value. These results clearly show the non-uniformity of the output beam as caused by a non-uniform gain profile.

The results shown in Figure 79 were computed based on geometric optics. However, in the region of peak intensity on the upstream side, diffraction is important. Figure 80, also obtained from Reference 71, shows the same case, except a more complicated, physical optics calculation is used to obtain the output intensity distribution. The effect of diffraction is to smooth out the sharpness of the peak as predicted from geometric optics in Figure 79. However, Figure 80 still shows a very non-uniform intensity distribution across the beam.

The amount of power contained in a focused beam in the far field does not seem to be materially reduced by a non-uniform distribution in the near field. However, the peak levels of the non-uniform intensity distribution may cause local overheating of the cavity output mirror

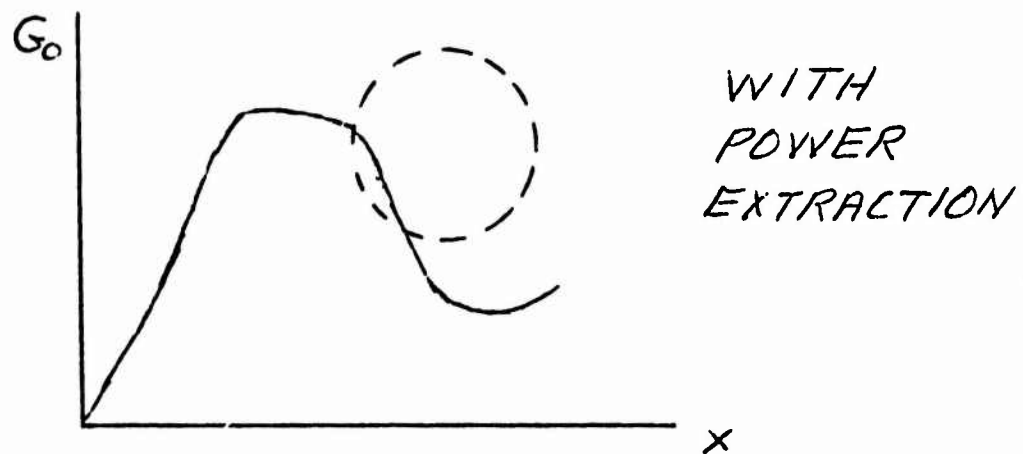
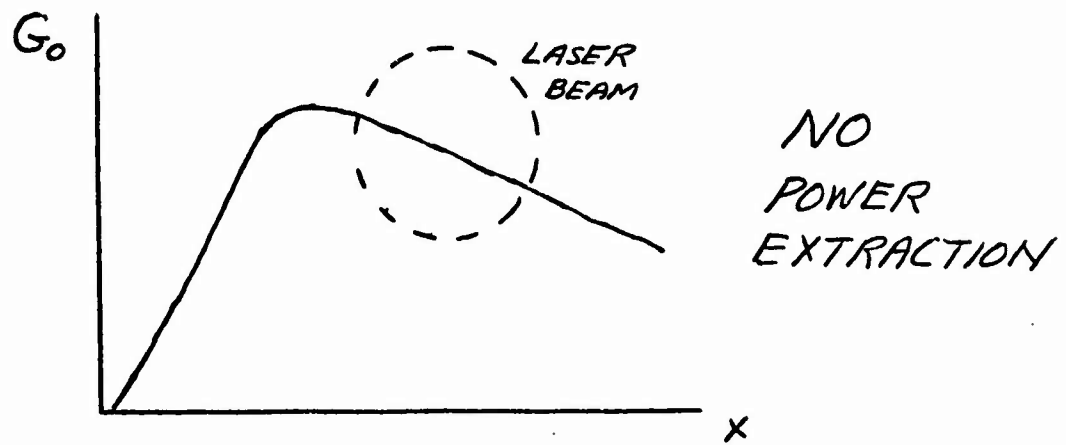


Fig. 78

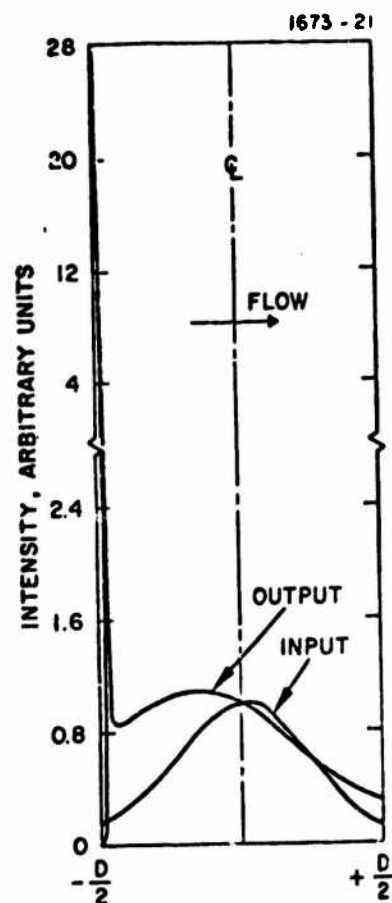


Fig. 79 Geometrical optics calculation of gain saturation induced distortion in a GDL amplifier.

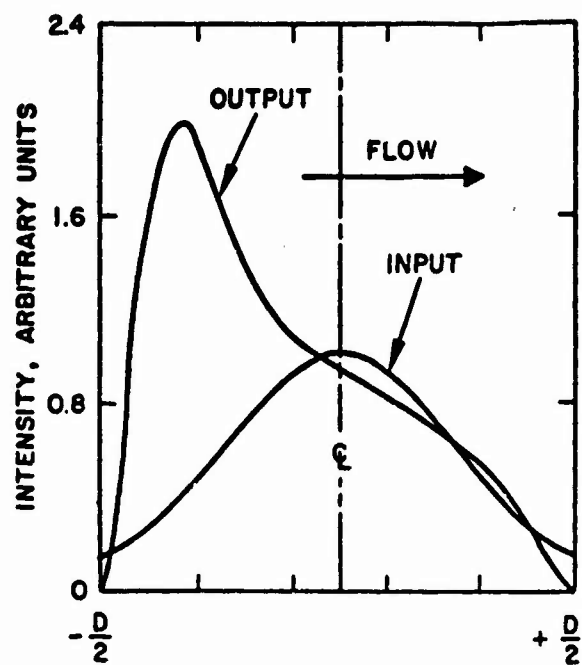


Fig. 80 Physical optics of gain saturation induced distortion in the GDL amplifier of Fig. 27.

or window, which could cause major problems. Therefore, such non-uniform peaks as shown in Figure 80 must be accounted for in mirror and window design.

### C. AERODYNAMIC WINDOWS

The preceding paragraph suggests that problems may arise with mirrors and windows in high power lasers. In fact, how do we physically extract the high intensity laser beam from the cavity, and allow it to pass to the surrounding atmosphere? One technique was mentioned in Sections IC and D, namely, to have a number of holes in the output mirror through which a portion of the radiation can pass. This is effective in extracting raw power, but causes major problems with beam quality. Incidentally, air leaks from the outside into the cavity through these holes can have a deleterious effect on the supersonic flow in the cavity and diffuser. An alternative technique is to simply extract the beam through a solid window. However, a certain amount of the laser energy is always absorbed by the window material, and for high energy lasers, the window heating causes a rapid deterioration of its transparency. In fact, at present there are no existing solid windows for practical use on high energy lasers.

A third technique, and the one which is most viable for present high energy lasers of all types -- electrical, chemical and gasdynamic, is to extract the beam through an aerodynamic window. To understand the principle of such windows, recall that expansion and shock waves in supersonic flows can support substantial pressure differences. This is illustrated in Figure 81. In a GDL, the cavity pressure is generally 0.1 atm, and the outside ambient pressure is 1 atm.

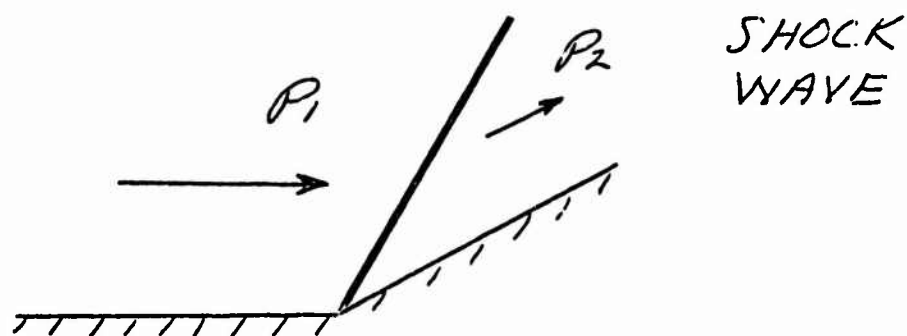
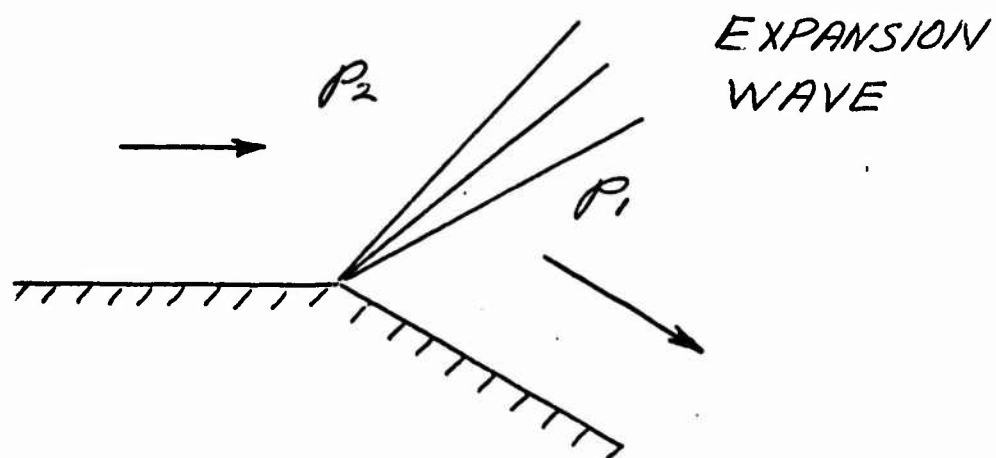


Fig. 81

Referring to Figure 81, expansion and compression waves can clearly act as a boundary between such pressure ratios, where  $p_1$  and  $p_2$  represent the cavity and ambient pressures respectively. This is the underlying idea of the aerodynamic windows shown in Figure 82, obtained from Reference 79. Here, three types of windows are illustrated. All three use a convergent-divergent nozzle to expand the flow to supersonic speeds. In the expansion window, an expansion wave is formed at the nozzle lip on the cavity side. In the compression window, an oblique shock wave is formed at the nozzle lip on the ambient side. The shock-expansion window combines both of the above wave systems. In all three, the laser beam propagates out of the low pressure cavity, through the expansion and/or shock waves, and into the ambient air at 1 atmosphere. Since air is almost transparent at  $10.6\mu$ , the laser intensity is not attenuated. Of course, with the aerodynamic window, there are no material heating problems.

A drawback of aerodynamic windows is that they require high mass flow rates of dry air or  $H_2$ . Parmentier<sup>79</sup> has shown that the mass flow is proportional to the square of the aperture diameter,  $D$  (see Figure 82). His results are shown in Figure 83 for the compression window, and in Figure 84 for the expansion and shock-expansion windows. Clearly, for meaningful aperture sizes on the order of 10-20 cm, large mass flow rates are required. Parmentier<sup>79</sup> points out that the shock-expansion window requires the smallest mass flow of any of the three types.

There are density variations in the beam direction through an aerodynamic window, hence there are phase distortions introduced



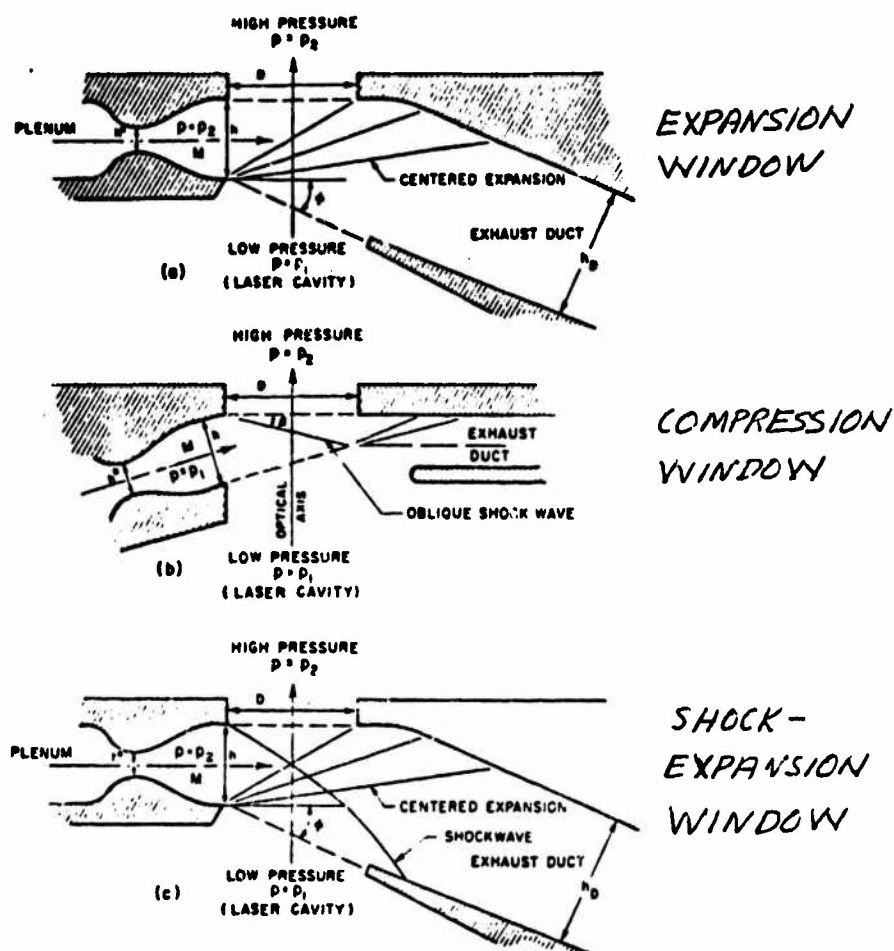


Fig. 82 Design and nomenclature for supersonic flow aerodynamic windows.

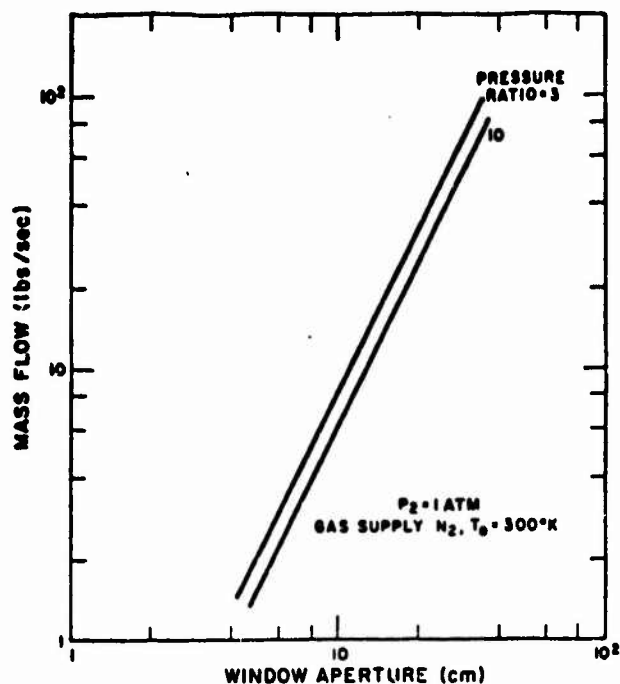


Fig. 83 Mass flow required for compression window operation.

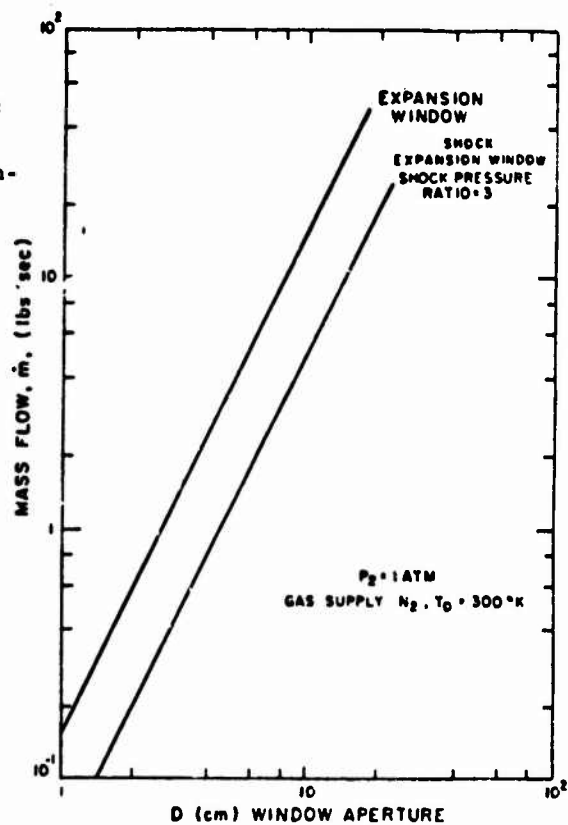


Fig. 84 Mass flow required for expansion window operation.

by the window into the beam. For the expansion or compression windows, the phase distortion is linear which results in simple beam steering, but no degradation in the far field. The density distributions through a shock-expansion window calculated by the method of characteristics are given by Parmentier<sup>79</sup>, and are shown in Figure 85. The corresponding phase distortion is shown in Figure 86.

Parmentier has conducted experiments with a shock-expansion window which are reported in Reference 79. Among these tests, an independent CO<sub>2</sub> laser beam from an electric discharge laser was passed through a 4 cm aperture aerodynamic window, as shown in Fig. 87. The results for the output beam intensity distribution are shown in Figure 88, which indicates only a small effect of the flow on the beam.

The results of Parmentier clearly show the feasibility, indeed the necessity, for aerodynamic windows on high power gas lasers.

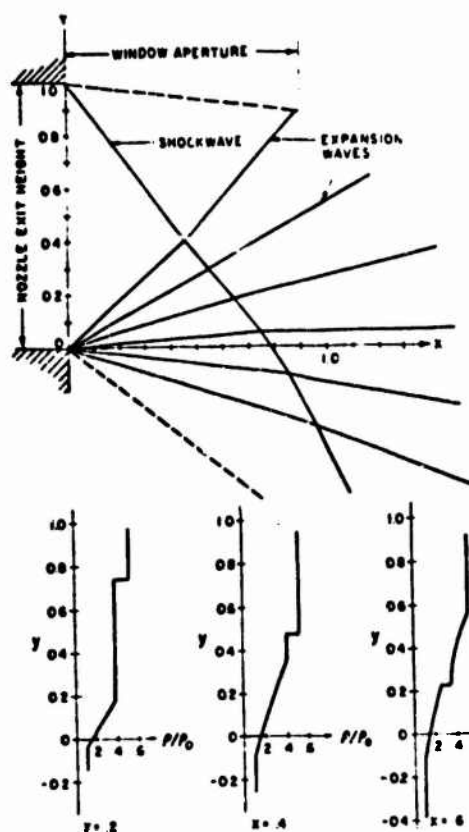


Fig. 85 Wave structure and density field in shock-expansion window aperture.

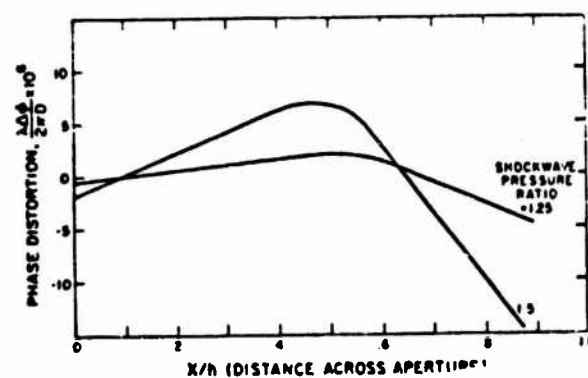


Fig. 86 Non-dimensional phase variation across the output aperture.

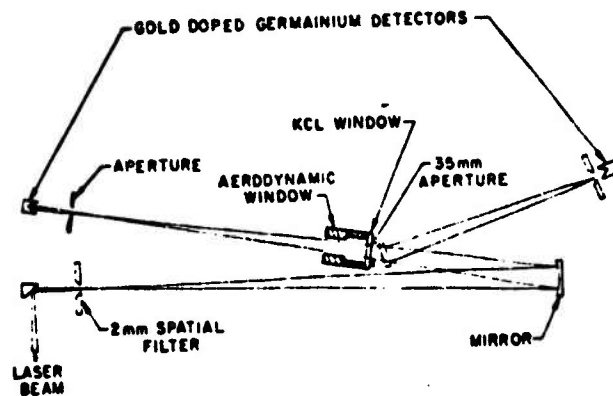


Fig. 87 Optical system for measuring beam quality degradation.

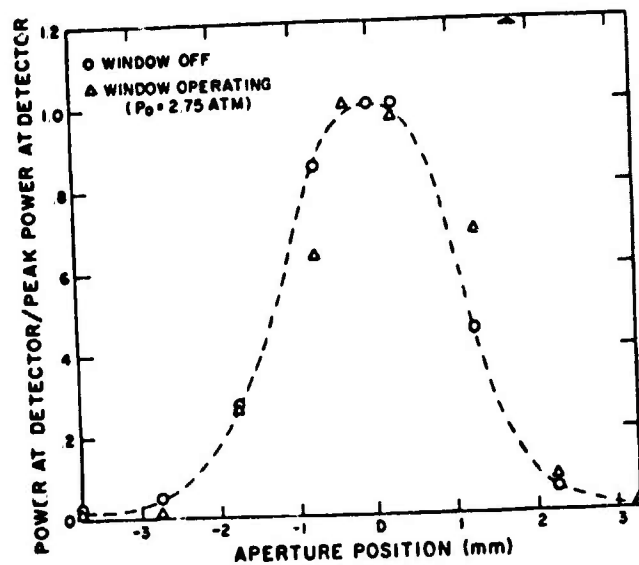


Fig. 88 Intensity distributions obtained by moving scanning aperture through focal point.

#### IV EPILOGUE

It is the author's hope that a serious student with no prior familiarity with gasdynamic lasers can, by studying these Notes and by examining the cited references, bring himself to the forefront of GDL understanding and the state-of-the-art. However, the technology of such lasers is developing rapidly, and what is the state-of-the-art today can become "classical" tomorrow. Therefore, the reader is encouraged to build on these Notes by keeping up with the modern literature, and indeed making his own contributions in the laboratory or in the theory of lasers. In the pressing energy conversion problems of today, high energy lasers will have a multitude of applications. We have just scratched the surface so far.

## REFERENCES

Note: A number of the following references are AIAA preprints, some of which are not yet available in the formal archive journals. Copies of these preprints may be obtained by writing to the American Institute of Aeronautics and Astronautics, 1290 Avenue of the Americas, New York, New York, U.S.A., 10019, at a cost of \$1.50 each for members and \$2.00 for non-members.

1. Gerry, E.T., "Gasdynamic Lasers", AIAA Paper No. 71-23 (1971), American Institute of Aeronautics and Astronautics, New York. See also, IEEE Spectrum, Vol. 7, Nov. 1970, pp. 51-58.
2. Klosterman, E.L. and Hoffman, A.L., "A High Pressure Shock Tube Driven Gasdynamic Laser", in Recent Developments in Shock Tube Research, Stanford University Press, Stanford, California, 1973, pp. 156-166.
3. Basov, N.G. and Oraevskii, A.N., "Attainment of Negative Temperatures by Heating and Cooling of a System", Soviet Physics JETP, Vol. 17, No. 5, Nov. 1963, pp. 1171-1172.
4. Hurle, I.R. and Hertzberg, A. "Electronic Population Inversions by Fluid-Mechanical Techniques," The Physics of Fluids, Vol. 8, No. 9, September 1965, pp. 1601-1607.
5. Kantrowitz, A.R., "Heat Capacity Lag in Gas Dynamics," Journal of Chemical Physics, Vol. 14, March 1946, pp. 150-164.
6. Basov, N.G., Mikhaylov, V.G., Oraevskii, A.N., and Shcheglov, V.A., "Obtaining a Population Inversion of Molecules in a Supersonic Stream of Binary Gas in a Laval Nozzle," Zhurnal Tekhnicheskoy Fiziki, Vol. 38, No. 12, 1968, pp. 2031-2041.
7. Taylor, R.L. and Bitterman, S., "Survey of Vibrational Relaxation Data for Processes Important in the  $\text{CO}_2$ - $\text{H}_2$  Laser System," Reviews of Modern Physics, Vol. 41, No. 1, Jan. 1969, pp. 26-47.
8. Anderson, John D., Jr., "Time-Dependent Analysis of Population Inversions in an Expanding Gas," The Physics of Fluids, Vol. 13, No. 8, August 1970, pp. 1983-1989.
9. Lee, G. and Gowen, F.E., "Gain of  $\text{CO}_2$  Gasdynamic Lasers," Applied Physics Letters, Vol. 18, No. 6, 15 March 1971, pp. 237-239.

10. Lee, G., Gowen, F.E. and Hagen, J.R., "Gain and Power of CO<sub>2</sub> Gasdynamic Lasers," AIAA Journal, Vol. 10, No. 1, January 1972, pp. 65-71.
11. Anderson, John D., Jr., Humphrey, R.L., Vamos, J.S., Plummer, M.J. and Jensen, R.E., "Population Inversions in an Expanding Gas: Theory and Experiment," The Physics of Fluids, Vol. 14, No. 12, December 1971, pp. 2620-2624.
12. Anderson, John D., Jr. and Winkler, E.M., "High Temperature Aerodynamics with Electromagnetic Radiation," Proceedings of the IEEE, Vol. 59, No. 4, April 1971, pp. 651-658.
13. Christiansen, W.H. and Tsongas, G.A., "Gain Kinetics of CO<sub>2</sub> Gasdynamic Laser Mixtures at High Pressure," The Physics of Fluids, Vol. 14, No. 12, December 1971, pp. 2611-2619.
14. Hertzberg, A., Johnston, E.W. and Ahlstrom, H.G., "Photon Generators and Engines for Laser Power Transmission," AIAA Journal, Vol. 10, No. 4, April 1972, pp. 394-400.
15. Vamos, John S., "Small-Signal Gain Measurements in a High-Ratio Nozzle Shock Tunnel GDL," AIAA Paper No. 74-177, presented at the AIAA 12th Aerospace Sciences Meeting, Jan. 30-Feb. 1, 1974.
16. Tennant, R., Vargas, R. and Hadley, S., "Effects of Gaseous Contaminants on Gasdynamic Laser Performance," AIAA Paper No. 74-178, presented at the AIAA 12th Aerospace Sciences Meeting, Jan. 30-Feb. 1, 1974.
17. Kuehn, D.H. and Honson, D.J., "Experiments with a CO<sub>2</sub> Gasdynamic Laser," Applied Physics Letters, Vol. 16, No. 1, Jan. 1970, pp. 48-50.
18. Tulip, J. and Sequin, H., "Explosion-Pumped Gas-Dynamic CO<sub>2</sub> Laser," Applied Physics Letters, Vol. 19, No. 8, 15 Oct. 1971, pp. 263-265.
19. Yatsiv, S., Greenfield, E., Dothan-Deutsch, F., Chuchem, D. and Bin-Hun, E., "Pulsed CO<sub>2</sub> Gas-Dynamic Laser," Applied Physics Letters, Vol. 19, No. 3, 1 August 1971, pp. 65-68.
20. Heinzer, R.A., "Experimental Gasdynamic Laser Studies", AIAA Journal, Vol. 10, No. 4, April 1972, pp. 383-393.
21. Anderson, John D., Jr. and Harris, E.L., "Modern Advances in the Physics of Gasdynamic Lasers," AIAA Paper No. 72-143, Presented at the AIAA 10th Aerospace Sciences Meeting, Jan. 17-19, 1972.
22. Anderson, John D., Jr., "Gas Dynamic Lasers: A State-of-the-Art Survey," 1972 IEEE Record, Vol. 14, pp. 180-183.



23. Anderson, John D., Jr. and Harris, E.L., "Gasdynamic Laser 2 Years Later," Laser Focus, Vol. 8, No. 5, May 1972, pp. 32-34.
24. Anderson, John D., Jr., "Effect of  $\text{H}_2$  on  $\text{CO}_2$ - $\text{H}_2$  Gasdynamic Laser Gain," Journal of Applied Physics, Vol. 43, No. 2, Feb. 1972, pp. 534-536.
25. Anderson, John D., Jr., "Sensitivity of Gasdynamic Laser Calculations to Uncertainties in Kinetic Rates," Tech. Report No. AE 73-2, Dept. of Aerospace Engineering, Univ. of Maryland, October 1973.
26. Anderson, John D., Jr., "The Effect of Kinetic Rate Uncertainties on Gasdynamic Laser Performance," AIAA Paper No. 74-176, presented at the AIAA 12th Aerospace Sciences Meeting, Jan. 30-Feb. 1, 1974.
27. Hoffman, Alan L. and Vlases, G.C., "A Simplified Model for Predicting Gain, Saturation, and Pulse Length for Gas Dynamic Lasers," IEEE Journal of Quantum Electronics, February 1972, pp. 46-53.
28. Murty, S.S.R., "Rapid Estimation of the Performance Characteristics of  $\text{CO}_2$  Gasdynamic Lasers," AIAA Paper No. 74-226, presented at the AIAA 12th Aerospace Sciences Meeting, Jan. 30-Feb. 1, 1974.
29. McKenzie, R.L., "Diatomic Gasdynamic Lasers," The Physics of Fluids, Vol. 15, December 1972, pp. 2163-2173.
30. Lengyel, Bela A., Lasers, 2nd Edition, Wiley Interscience, New York, 1971.
31. Gerry, E.T. and Leonard, D.A., "Measurements of  $10.6\mu$   $\text{CO}_2$  Laser Transition Probability and Optical Broadening Cross Sections," Applied Physics Letters, Vol. 8, 1 May 1966, pp. 227-229.
32. Anderson, John D., Jr., "Numerical Experiments Associated with Gas Dynamic Lasers," NOLTR 70-198, Naval Ordnance Laboratory, White Oak, Md., Sept. 1970.
33. Hall, J. Gordon, and Treanor, Charles E., "Nonequilibrium Effects in Supersonic-Nozzle Flows," AGARDograph No. 124, 1967.
34. Anderson, John D., Jr., "A Time-Dependent Analysis for Vibrational and Chemical Nonequilibrium Nozzle Flows," AIAA Journal, Vol. 8, No. 3, March 1970, pp. 545-550.
35. Anderson, John D., Jr., "Time-Dependent Solutions of Nonequilibrium Nozzle Flows -- A Sequel," AIAA Journal, Vol. 8, No. 12, December 1970, pp. 2280-2282.
36. MacCormack, R.W., "The Effect of Viscosity in Hypervelocity Impact Cratering," AIAA Paper No. 69-354.

37. Courant, R., Friedrichs, K.O. and Levy, H., "Ueber die Differenzengleichungen der Mathematischen Physik," Math. Ann. Vol. 100, 1928, p. 32.
38. Taylor, R.L. and Bitterman, S., "Survey of Vibrational Relaxation Data for Processes Important in the  $\text{CO}_2$ - $\text{H}_2$  Laser System," AVCO Everett Research Report 282, October 1967.
39. Rich, J. W. and Treanor, C.E., "Vibrational Relaxation in Gas-Dynamic Flows," in Annual Review of Fluid Mechanics, Annual Reviews, Inc., Palo Alto, California, Vol. 2, 1970, pp. 355-396.
40. Anderson, John D., "A Time-Dependent Quasi-One-Dimensional Analysis of Population Inversions in an Expanding Gas," NOLTR 69-200, Naval Ordnance Laboratory, White Oak, Md., December 1969.
41. Munjee, S.A., "Numerical Analysis of a Gasdynamic Laser Mixture," Physics of Fluids, Vol. 15, No. 3, pp. 506-508, March 1972.
42. Buonadonna, V.R. and Christiansen, W.H., "Gain Measurements of High Temperature  $\text{CO}_2$  Laser Mixtures in a Shock Tube Driven Flow," in Recent Developments in Shock Tube Research, Stanford University Press, Stanford, California, 1973, pp. 174-183.
43. Heiche, G. and Harris, E.L., Naval Ordnance Laboratory, White Oak, Md. (unpublished)
44. Rigrod, W.W., "Saturation Effects in High-Gain Lasers," Journal of Applied Physics, Vol. 36, August 1965, pp. 2487-2490.
45. Anderson, John D., Jr., Humphrey, R.L., Vamos, J.S., Plummer, H.J. and Jensen, R.E., "Population Inversions in an Expanding Gas: Theory and Experiment," NOLTR 71-116, Naval Ordnance Laboratory, White Oak, Md., June 1971.
46. Sharma, R.D., "Vibrational Relaxation of  $\text{CO}_2$  by  $\text{H}_2\text{O}$ ," Journal of Chemical Physics, Vol. 54, No. 2, 15 January 1971, pp. 810-811.
47. Winkler, E.H., Humphrey, R.L. and Koenig, J.A., "The NOL Four-Ring Three-Phase AC Arc Heater (HKIV)," NOLTR 70-12, Jan. 1970.
48. Warren, W.R., "Determination of Air Stagnation Properties in High-Enthalpy Test Facility," Journal of Aerospace Sciences, Vol. 26, No. 12, Dec. 1959, pp. 835-836.
49. Madden, M.T., Anderson, J.D., Jr., and Piper, C.H., "Equilibrium Normal Shock Properties for Vibrationally Excited  $\text{CO}_2$ - $\text{H}_2$ -He Gas Mixtures," NOLTR 70-103, May 1970.
50. Greenberg, R.A., Schneiderman, A.M., Ahouse, D.R., and Parmentier, E.H., "Rapid Expansion Nozzles for Gas Dynamic Lasers," AVCO Research Laboratory AWP 314, Dec. 1970.

51. Wagner, J.L., "A Cold Flow Field Experimental Study Associated with a Two-Dimensional Multiple Nozzle," NOLTR 71-78, July 1971.
52. Howgate, D.W., Roberts, T.G. and Barr, T.A., "Numerical Calculation of the Arc-Driven Supersonic Laser Operating in the Gas-Dynamic Mode," Journal of Applied Physics, Vol. 43, No. 6, June 1972, pp. 2799-2804.
53. McLeary, R., "Calculation of Gain and Power Output for a Gas-Dynamic Laser," IEEE Journal of Quantum Electronics, August 1972, pp. 716-718.
54. Biriukov, A.S., Dronov, A.P., Koudriavtsev, E.M. and Sobolev, N.M., "Gas Dynamic CO<sub>2</sub>-He-N<sub>2</sub> Laser Investigations," IEEE Journal of Quantum Electronics, Vol. QE-7, No. 8, August 1971, pp. 388-391.
55. Sato, K. and Sekiguchi, T., "Dependence of the Output Power of CO<sub>2</sub> Gas-Dynamic Laser on the Distance from Nozzle Throat," Journal of the Physical Society of Japan, Vol. 35, 1973, pp. 630.
56. Gembarzhevskiy, G.V., Generalov, N.A., Kozlov, G.I. and Roytenburg, D.I., "Amplification Factor of Light in a CO<sub>2</sub>, N<sub>2</sub>, He Mixture as it Expands in a Supersonic Nozzle," Zhurnal Eksperimental'noy i Teoreticheskoy Fiziki, Vol. 62, No. 3, 1972, pp. 844-847.
57. Gabai, A., Rokni, M., Greenfield, E., Dothan-Deutsch, F. and Yatsiv, S., "CO<sub>2</sub> Gasdynamic Laser by Detonation of a Solid Explosive," presented at the VII International Quantum Electronics Conference, Montreal, May 1972.
58. Anderson, John D., Jr., and Madden, H.T., "Population Inversions behind Normal Shock Waves," AIAA Journal, Vol. 9, No. 8, August 1971, pp. 1630-1632.
59. Anderson, John D., Jr., Madden, H.T. and Piper, C.H., "Vibrational Population Inversions Behind Normal Shock Waves in CO<sub>2</sub>-N<sub>2</sub>-He Mixtures," NOLTR 70-214, Oct. 1970.
60. Lalos, G., private communication, Aug. 6, 1970, Naval Ordnance Laboratory, White Oak, Md.
61. McKenzie, R.L., "Diatomic Gasdynamic Lasers," The Physics of Fluids, Vol. 15, Dec. 1972, pp. 2163-2173.
62. Glowacki, Walter J. and Anderson, John D., Jr., "A Computer Program for CO<sub>2</sub>-N<sub>2</sub>-H<sub>2</sub>O Gasdynamic Laser Gain and Maximum Available Power," NOLTR 71-210, Oct. 1971.
63. Pallay, B.G. and Zovko, C.T., "Fuels, Oxidizers and Gas Generators for Gas Dynamic Lasers," AIAA Paper No. 73-1233 (1973)
64. Treanor, C.E., Rich, J.W. and Rehm, R.G., "Vibrational Relaxation of Anharmonic Oscillators with Exchange-Dominated Collisions," Journal of Chemical Physics, Vol. 48, No. 4, Feb. 1968, pp. 1793-1807.

65. Bronfin, B.R., Boedeker, L.R., and Cheyer, J.P., "Thermal Laser Excitation by Mixing in a Highly Convective Flow," Applied Physics Letters, Vol. 16, No. 5, March 1970, pp. 214-217.
66. Milewski, J., Brunne, M., Stanco, J., Zielinski, A., Irczuk, M. and Kusmierek, Jr., "CW Gasdynamic Sthermally Excited and Selectively Pumped CO<sub>2</sub>-N<sub>2</sub> Mixing Laser," Bulletin De L'Academie Polonaise Des Sciences, Vol. 20, No. 4, 1972, pp. 313-319.
67. Chroshko, V.N., Soloukhin, R.I., and Wolanski, P., "Population Inversion by Mixing in a Shock Tube Flow," Optics Communications, Vol. 6, No. 3, Nov. 1972, pp. 275-277.
68. Chroshko, V.N., Soloukhin, R.I. and Wolanski, P., "Population Inversion by Mixing in a Shock Tube Flow," in Recent Advances in Shock Tube Research, Stanford Univ. Press, 1973, pp. 167-172.
69. Borghi, R. and Charpenel, M., "The High Velocity Mixing Between Vibrationally Excited Nitrogen and Carbon Dioxide," Astronautica Acta Vol. 17, Nos. 4 and 5, 1972, pp. 833-842.
70. Taran, J.P.E., Charpenel, M. and Borghi, R., "Investigation of a Mixing CO<sub>2</sub> GDL," AIAA Paper No. 73-622 (1973)
71. Clari, P.O., "Design Considerations for High Power Laser Cavities," AIAA Paper No. 72-708 (1972).
72. Kogelnik, H. and Li, T., "Laser Beams and Resonators," Applied Optics Vol. 5, No. 10, October 1966, pp. 1550-1567.
73. Simons, G.A., "The Effect of Boundary Layers on GDL Medium Homogeneity," AIAA Paper No. 72-709 (1972).
74. Royle, J.K., Bowling, A.G. and Lukasiewicz, J., "Calibration of Two-Dimensional and Conical Supersonic Multi-Nozzles," RAE Report AERO 2221, S.D. 23, 1947.
75. Russell, D.A., "Fluid Mechanics. of High Power Grid Nozzle Lasers," AIAA Paper No. 74-223 (1974)
76. Director, Mark H., "Aerodynamic Parameters Affecting Practical Gas Dynamic Laser Design," AIAA Paper No. 73-626 (1973)
77. Hoffman, A.L. and Jones, T.G., "Geometrical Methods for Improving the Optical Quality of Gasdynamic Lasers," AIAA Paper No. 72-217 (1972).
78. Sutton, G.W., "Effect of Turbulent Fluctuations in an Optically Active Fluid Medium," AIAA Journal, Vol. 7, No. 9, Sept. 1969, pp. 1737-1743.
79. Parmentier, E.M., "Supersonic Flow Aerodynamic Windows for High Power Lasers," AIAA Paper No. 72-710 (1972)

# THE EFFECT OF KINETIC RATE UNCERTAINTIES ON GASDYNAMIC LASER PERFORMANCE<sup>†</sup>

John D. Anderson, Jr.  
Professor and Chairman  
Department of Aerospace Engineering  
University of Maryland  
College Park, Maryland 20742

## ABSTRACT

Recent data for the vibrational energy exchange rates associated with  $\text{CO}_2\text{-N}_2\text{-H}_2\text{O}$  gas lasers are compared with previous compilations. From this, current uncertainties in the rate data are established. Using an existing computer code, a study is made of the sensitivity of gasdynamic laser performance to these uncertainties. The results show that present-day calculations of gasdynamic laser gain and maximum available power are subject to at least a 25 percent inaccuracy due to such rate data uncertainties.

## I. INTRODUCTION

The first successful demonstration of a  $\text{CO}_2\text{-N}_2$  gasdynamic laser took place in 1965, as described by Gerry<sup>(1)</sup>. Since then, the state-of-the-art has blossomed and matured at a rapid rate, as surveyed in References 2-4. In particular, a number of gasdynamic laser experiments have been carried out in arc tunnels<sup>(5-7)</sup>, shock tunnels<sup>(7-9)</sup> and combustion driven devices<sup>(1, 10-12)</sup>. In many of these experimental investigations, comparisons have been made with theory for small-signal laser gain and/or laser power extraction. Fair agreement has been obtained in some but not all cases. With the rapid development of such lasers, there is an increasing need to obtain closer agreement between prediction and experiment; indeed, it is desirable to calculate gasdynamic laser performance as accurately as possible -- ultimately to within a few percent.

At present, there is an inherent limitation to the accuracy with which such calculations can be made, namely, the uncertainty in the pertinent vibrational kinetic rates. The heart of a gasdynamic laser is the nonequilibrium nozzle expansion in which the population inversion is created, and the laser cavity downstream of the nozzle exit where power is extracted. In both these regions the computed nonequilibrium flow (and hence the theoretical laser performance) is dependent on a complex finite-rate vibrational energy exchange mechanism which is still not yet fully understood. For the  $\text{CO}_2\text{-N}_2\text{-H}_2\text{O}$  mixture common to most gasdynamic lasers, at least eight distinct vibrational kinetic rates must be utilized in the calculations. In turn, uncertainties in these rates will cause inaccuracies in the computed gasdynamic laser performance. Hence, two questions immediately arise: (1) what are the present uncer-

tainties in the measured kinetic rates, and (2) how sensitive are calculations of gasdynamic laser performance to these uncertainties? The purpose of the present investigation is to answer these questions.

In particular, the rates, their uncertainties, and some details concerning their effect on gasdynamic laser small-signal gain and maximum available power are discussed in Section II. The quantitative sensitivity of gasdynamic laser calculations to each vibrational kinetic energy exchange reaction is defined in Section III, and bar charts are presented which graphically demonstrate the absolute uncertainties which currently exist in such calculations. Finally, those particular reactions which have the most influence on gasdynamic laser gain and maximum available power are clearly delineated.

The calculations of gasdynamic laser performance in the present paper were made with an existing computer program described in Reference 13. This computer code is based on the time-dependent nonequilibrium nozzle flow analysis discussed in References 14 and 15, and applied to gasdynamic lasers in Reference 16.

## II. RATES AND UNCERTAINTIES

The vibrational kinetic rates pertinent to  $\text{CO}_2\text{-N}_2$  gas lasers were examined and compiled by Taylor and Bitterman, first in 1967 (Reference 17) and slightly updated in 1969 (Reference 18). These references are timely and excellent surveys, and have become a standard source for laser calculations. However, in 1969, References 17 and 18 clearly show that a large scatter existed in much of the data; moreover, for a few rates, only one set of data were available. Hence, in the present paper, additional  $\text{CO}_2\text{-N}_2\text{-H}_2\text{O}$  vibrational rates measured or calculated since 1969 are presented along with the standard Taylor and Bitterman data; this is an effort to assess uncertainties which currently exist in these rates. (Some of the rates measured since 1969 have been recently catalogued in an unpublished memorandum by D. W. Hall<sup>(19)</sup>. The present author gratefully acknowledges the help of this memorandum as a reference source.)

The reactions that must be included in the calculation of small-signal gain and maximum available power in gasdynamic lasers are:

<sup>†</sup>This research was supported by the Air Force Office of Scientific Research under AFOSR Grant No. 74-2575, with Captain Lloyd R. Lawrence, Jr. as Program Manager. A portion of the computer time was kindly provided by the Computer Science Center of the University of Maryland.

\*Member, AIAA

1.  $\text{CO}_2^* (\nu_2) + \text{H}_2\text{O} \rightleftharpoons \text{CO}_2 + \text{H}_2\text{O}$
2.  $\text{N}_2^* + \text{H}_2\text{O} \rightleftharpoons \text{N}_2 + \text{H}_2\text{O}$
3.  $\text{CO}_2^* (\nu_3) + \text{H}_2\text{O} \rightleftharpoons \text{CO}_2^{***} (\nu_2) + \text{H}_2\text{O}$
4.  $\text{CO}_2^* (\nu_2) + \text{N}_2 \rightleftharpoons \text{CO}_2 + \text{N}_2$
5.  $\text{CO}_2^* (\nu_2) + \text{CO}_2 \rightleftharpoons 2\text{CO}_2$
6.  $\text{CO}_2^* (\nu_3) + \text{N}_2 \rightleftharpoons \text{CO}_2^{***} (\nu_2) + \text{N}_2$
7.  $\text{CO}_2^* (\nu_3) + \text{CO}_2 \rightleftharpoons \text{CO}_2^{***} (\nu_2) + \text{CO}_2$
8.  $\text{N}_2^* + \text{N}_2 \rightleftharpoons 2\text{N}_2$

For such calculations, the pumping rate between excited  $\text{N}_2$  and  $\text{CO}_2(001)$ , as well as the Fermi resonance between  $\text{CO}_2(100)$  and  $\text{CO}_2(020)$ , are considered to be sufficiently rapid that local equilibrium is established between  $\text{H}_2$  and  $\text{CO}_2(\nu_3)$  as well as between  $\text{CO}_2(\nu_1)$  and  $\text{CO}_2(\nu_2)$ . Hence, the rates for these reactions are not considered here. However, it should be noted that recent information has raised some questions about the local equilibrium normally assumed between the  $\text{CO}_2(\nu_1)$  and  $\text{CO}_2(\nu_2)$  modes. Specifically, Rosser,

Moag and Gerry<sup>(20)</sup> present data which indicate that such equilibrium may not exist for all laser conditions. This contention is further supported by Bulthius<sup>(21)</sup>, who presents a measured rate for energy transfer from the (100) to (020) level which is an order of magnitude slower than previously reported values, and prompts a comment that the vibrational temperatures of the  $\text{CO}_2(\nu_1)$  and  $\text{CO}_2(\nu_2)$  modes are not always the same, particularly during peak power extraction. On the other hand, De Temple et al<sup>(22)</sup> countered these contentions by presenting measurements for the decay rate of  $\text{CO}_2(100)$  which are an order of magnitude faster than those of Rosser et al<sup>(20)</sup>. De Temple et al feel that their measurements are more representative of the intrinsic V-V relaxation process, whereas those of Reference 20 are more characteristic of a V-T process under the influence of a perturbing radiation field. This matter, albeit an important one, is still in a state of flux; until it is resolved, the assumption of local equilibrium between the  $\text{CO}_2(\nu_1)$  and  $\text{CO}_2(\nu_2)$  modes appears to be the only logical recourse for gasdynamic laser calculations.

The effect of  $\text{H}_2\text{O}$  on the laser process is governed by reactions 1-3 above. The role of  $\text{H}_2\text{O}$  is quite important; indeed, the deactivation of the lower laser level by  $\text{H}_2\text{O}$  has been considered in the past to be the pivotal reaction for  $\text{CO}_2\text{-N}_2\text{-H}_2\text{O}$  gasdynamic lasers. The rate data for this reaction is compiled in Figure 1. In this and other figures to follow, the lines and symbols are identified as follows:

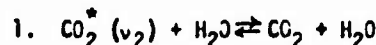
(1) The vertical bars delineate the scatter of experimental data shown in the 1969 paper by Taylor and Bitterman<sup>(18)</sup>.

(2) The solid curves delineate the rates used by the present author in earlier calculations of gasdynamic laser properties<sup>(2-4, 7, 16, 23, 24)</sup>. The solid curves will be denoted as "reference" rates in the present paper. Simple correlations of these rates are given in Appendix A of Reference 23, which is a modified version of the earlier correlations given in Appendix A of Reference 24. These correlations were originally obtained from the "best fits" given in the 1967 report of Taylor and Bitterman<sup>(17)</sup>, which for some reactions differ from the results shown in the 1969 paper by the same authors<sup>(18)</sup>.

(3) The dotted lines represent fast and slow rates chosen for performing numerical uncertainty tests, to be described later. In those figures where only one dotted line appears, the reference curve is used for the other limit on the rate. Note that the dotted curves are for numerical experimentation only; they do not necessarily reflect the actual uncertainty that exists in the data.

(4) The solid and open symbols are new data published after the appearance of the 1969 paper by Taylor and Bitterman<sup>(18)</sup>.

Finally, a note is made that the rate constants and their effects on gasdynamic laser performance which are examined in the present paper are also discussed in depth in Reference 25; this reference should be consulted for more details.



The rate data for this reaction is compiled in Figure 1, which gives the constant as a function of temperature. The wide scatter in the data demonstrates the large uncertainty which still exists in this rate; indeed, even the temperature dependence of the rate constant is not clear. The experimental data of Bulthius et al<sup>(26,27)</sup>, Buchwald and Bauer<sup>(28)</sup>, and the calculations of Sharma<sup>(29)</sup> are shown along with the original spread of data from Taylor and Bitterman<sup>(18)</sup>. At the present time, the reference rate (solid line) appears to be as good a representation of this rate as any other.

Using the computer code described in Reference 13, gasdynamic laser calculations have been made alternately employing the fast and slow rates shown as the dotted lines in Figure 1. Some corresponding results for small-signal gain,  $G_0$ , are shown as the dotted curves in Figures 2 and 3. In these calculations, only the rate for  $\text{CO}_2^* (\nu_2) + \text{H}_2\text{O} \rightleftharpoons \text{CO}_2 + \text{H}_2\text{O}$  is varied; all other rates are held fixed at their reference values. The solid curves in these figures are the results obtained using the reference rates only. In particular, Figures 2 and 3 illustrate the peak small-signal gain as a function of reservoir temperature,  $T_0$ , for the following cases respectively.

(1) 20:1 area ratio nozzle with throat height

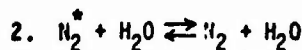


$h^* = 1.0 \text{ mm}$ , 7%  $\text{CO}_2$ , 1%  $\text{H}_2\text{O}$ , 92%  $\text{N}_2$ .

(2) 50:1 area ratio nozzle with  $h^* = 0.365 \text{ mm}$ , 7%  $\text{CO}_2$ , 3.5%  $\text{H}_2\text{O}$  and 89.5%  $\text{N}_2$ .

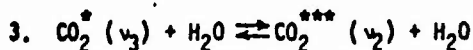
Cases (1) and (2) are typical of "first and second generation" gasdynamic lasers respectively, as described in References 2-4. In Figure 2, the results for the fast and slow rates differ appreciably. In Figure 3, which is a case with 3.5%  $\text{H}_2\text{O}$  content in the gas mixture, the difference is not large at low temperatures, but increases at higher temperatures. For this case, the relatively high water content promotes rapid equilibration of the lower laser level with the translational temperature, and tends to swamp the effect of a factor of 3 difference between the fast and slow rates. Additional results are presented and discussed in Reference 25.

From the results shown in Figures 2 and 3, a quantitative measure of the sensitivity of gasdynamic laser gain to uncertainties in the rate constant can be established. Such quantitative "sensitivity factors" and "absolute uncertainties" are discussed in Section III of this paper. Moreover, the trends shown in these figures clearly indicate that the reaction  $\text{CO}_2^*(v_2) + \text{H}_2\text{O} \rightleftharpoons \text{CO}_2 + \text{H}_2\text{O}$  plays an important role in the gasdynamic laser process, a fact that is well known. However, there are other reactions which are equally as important; these will be discussed in the following paragraphs. The importance of all the reactions will be compared in Section III.



The rate constants for this reaction are given in Figure 4 as a function of temperature. The symbols and curves have the same meaning as before. The post-1969 experimental data of von Rosenberg et al (30) and Evans (31) are shown. Comparing all the data in Figure 4, a wide discrepancy exists at the higher temperatures.

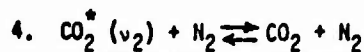
The effect of fast and slow rates on peak gain, gain profiles, and maximum available energy,  $e_{\text{max}}$ , is shown in detail in Reference 25, and will be summarized in Section III of this paper. However, from these results, the conclusion is made that the reaction  $\text{N}_2^* + \text{H}_2\text{O} \rightleftharpoons \text{N}_2 + \text{H}_2\text{O}$  is very important to the gasdynamic laser process, especially for the case of a 50:1 nozzle with 3.5%  $\text{H}_2\text{O}$  (typical of possible second generation devices). This reaction is something of a "sleeper" in that (to the author's knowledge) its importance has not been fully appreciated in the past.



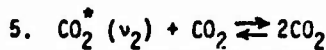
The rate constants for this reaction are plotted in Figure 5 as a function of temperature. The data of Rosser and Gerry (32), and Heller and Moore (33) are compared with the single set of data from Taylor and Bitterman (18). Again, there exists a definite uncertainty in the data, even with

regard to the correct temperature dependence.

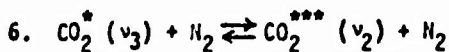
The influence of uncertainties in this rate on gasdynamic laser gain and maximum available energy are shown in detail in Reference 25. As in the case of the previous two rates, the reaction  $\text{CO}_2^*(v_3) + \text{H}_2\text{O} \rightleftharpoons \text{CO}_2^{***}(v_2) + \text{H}_2\text{O}$  exerts a strong influence on laser performance, as will be discussed in Section III.



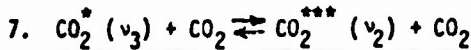
The rate constants for this reaction are plotted in Figure 6. For this rate, Taylor and Bitterman (18) show no actual data, hence no bars are shown in Figure 6. Instead, they recommend a rate which is 0.2 times that for  $\text{CO}_2^*(v_2) + \text{CO}_2 \rightleftharpoons 2\text{CO}_2$ . The reference rate (13), shown as the solid line, uses a factor of 0.25. However, data from Shields, Warf and Bass (34), Merrill and Amme (35), and Bauer and Schotter (36) are now available, and are plotted on Figure 6. From this recent information, it appears that the rate for  $\text{CO}_2^*(v_2) + \text{N}_2 \rightleftharpoons \text{CO}_2 + \text{N}_2$  is closer to 0.5 times that for  $\text{CO}_2^*(v_2) + \text{CO}_2 \rightleftharpoons 2\text{CO}_2$ . As will be shown in Section III, this rate does not have a strong influence on gasdynamic laser performance.



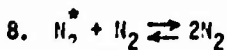
The rate constants for this reaction are plotted in Figure 7 as a function of temperature. The recent data of Eckstrom and Bershader (37) are also shown. This rate appears to be well-known; moreover, as will be shown in Section III, it has a very minor influence on gasdynamic laser performance. Hence, any uncertainty in this rate is of little consequence.



The rate constants for this reaction are given in Figure 8 as a function of temperature. The data of Rosser, Wood and Gerry (38) are also shown. There appears to be a reasonable uncertainty in this rate, which, as will be shown in Section III, has a strong influence on gasdynamic laser performance.



The rate constants for this reaction are given in Figure 9, along with the more recent data of Reid et al (39) and Seery (4). The uncertainty is not severe; moreover, as will be shown in Section III, the laser performance is insensitive to uncertainties in this rate. Hence, this rate is of little importance.



This is by far the least important rate in the gasdynamic laser process, as will be shown in Section III. Hence, the uncertainty in the rate

shown by Taylor and Bitterman<sup>(18)</sup> is of no consequence in laser performance.

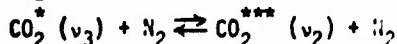
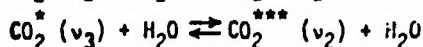
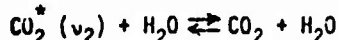
### III. SENSITIVITY OF GASDYNAMIC LASER PERFORMANCE TO UNCERTAINTIES IN RATES

In this section, the aforementioned rate processes, their uncertainties, and their effect on the gasdynamic laser process are quantified and compared. Specifically, the vertical distance between the dotted lines (or dotted and solid lines) shown in the previous figures for the rate constants,  $k$ , define a "change in rate constant",  $\Delta k$ . In turn, this change,  $\Delta k$ , causes a corresponding change in small-signal gain,  $\Delta G_0$ , as shown for example in Figures 2 and 3. Hence, a sensitivity factor,  $S$ , can be defined for each rate as:

$$S = (\Delta G_0 / G_0) / (\Delta k / k)$$

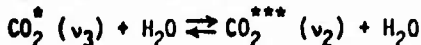
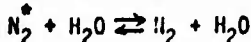
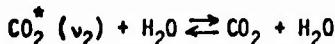
Here,  $\Delta k$  is specified on the previous figures, and  $\Delta G_0$  is calculated from the results of gasdynamic laser calculations<sup>(13)</sup>, as shown in Figures 2 and 3. Therefore,  $S$  physically represents the uncertainty in gain per unit uncertainty in rate constant.

The sensitivity of gasdynamic laser gain to the various rates is clearly shown in Figure 10 for a low nozzle area ratio case typical of first generation devices. Here, the sensitivity factor  $S$  is plotted as a function of reservoir temperature,  $T_0$ ; a curve is shown for each of the rates considered in the present investigation. For the case shown, the laser gain is most sensitive to reactions 1, 3 and 6, and least sensitive to reaction 8. In fact, for  $T_0 = 1200^\circ\text{K}$  (which is typical of first generation gasdynamic lasers), the rather remarkable observation is made that the reactions



all exert equal and maximum sensitivity on calculations of gasdynamic laser gain.

Similar results are shown in Figure 11 for a case typical of high area ratio, high  $\text{H}_2\text{O}$  content, second generation devices. Here, in addition to reactions 1, 3 and 6, reaction 2 is seen to be important. In fact, at  $T_0 = 1800^\circ\text{K}$  (which is typical of second generation devices), the reactions



exert the most sensitivity on calculations of gasdynamic laser gain. Reflecting on Figure 11, emphasis is made of the importance of the reaction  $\text{N}_2 + \text{H}_2\text{O} \rightleftharpoons \text{H}_2 + \text{H}_2\text{O}$ . The effect of this reaction previously has not been fully appreciated by the present author, nor presumably by other workers in the field as well.

Considering maximum available energy,  $e_{\text{max}}$ , a sensitivity factor can also be defined analogous to that for gain. This factor is shown in Figures 12 and 13 for the first and second generation laser cases respectively. Curves for the rates involving deactivation of the lower laser level are not shown because they have a minimal effect on  $e_{\text{max}}$ .

Comparing Figures 12 and 13 with 10 and 11, the reactions that exert maximum and minimum sensitivities on  $e_{\text{max}}$  are the same that exert maximum and minimum sensitivity on  $G_0$ .

The results shown in Figures 10-13 are uncertainties in performance per unit uncertainty in rate constant, hence they indicate the sensitivity of gasdynamic laser calculations to the individual rates. However, as previously discussed, some rate constants are known more accurately than others; hence, the question is now posed, what are the absolute uncertainties in  $G_0$  and  $e_{\text{max}}$  due to the existing absolute uncertainties in rate constants? These existing absolute uncertainties are given below, and were obtained from examination of the data scatter shown in Figures 1,4-9.

Reaction	Uncertainty in data, $\Delta k/k$
1. $\text{CO}_2^*(v_2) + \text{H}_2\text{O} \rightleftharpoons \text{CO}_2 + \text{H}_2\text{O}$	3
2. $\text{N}_2 + \text{H}_2\text{O} \rightleftharpoons \text{H}_2 + \text{H}_2\text{O}$	5
3. $\text{CO}_2^*(v_3) + \text{H}_2\text{O} \rightleftharpoons \text{CO}_2^{***}(v_2) + \text{H}_2\text{O}$	5
4. $\text{CO}_2^*(v_2) + \text{H}_2 \rightleftharpoons \text{CO}_2 + \text{H}_2$	4
5. $\text{CO}_2^*(v_2) + \text{CO}_2 \rightleftharpoons 2\text{CO}_2$	0.5
6. $\text{CO}_2^*(v_3) + \text{N}_2 \rightleftharpoons \text{CO}_2^{***}(v_2) + \text{N}_2$	5.0
7. $\text{CO}_2^*(v_3) + \text{CO}_2 \rightleftharpoons \text{CO}_2^{***}(v_2) + \text{CO}_2$	0.25
8. $\text{H}_2 + \text{H}_2 \rightleftharpoons 2\text{H}_2$	0.5

In establishing the values of  $\Delta k/k$  shown above, some weight has been given to the recent data. In addition, in reactions 2, 3 and 6, which effect the deactivation of the upper laser level, more weight has been given to the data scatter at the higher temperatures because a large part of the upper level deactivation in a gasdynamic laser occurs in the throat region of the nozzle, where the static temperature is still reasonably high.

When the sensitivity factors shown in Figures 10-13 are multiplied by the above absolute rate data uncertainties,  $\Delta k/k$ , the overall uncertainties in  $G_0$  and  $e_{\text{max}}$  are obtained. These results are shown as bar charts in Figures 14 and 15 for  $G_0$  and  $e_{\text{max}}$  respectively. In these figures, reservoir temperatures of  $1200^\circ\text{K}$  and  $1800^\circ\text{K}$  are chosen as typical of first and second generation gasdynamic lasers, respectively. The important conclusion apparent from Figures 14 and 15 is that gasdynamic laser calculations of gain and maximum available energy, based on present-day knowledge of rates in the existing literature, appear to be subject to at least a 25 percent uncertainty.



#### IV. COMPARISON WITH EXPERIMENT

Based on the above study, the rates that are used in the existing computer code of Reference 13 appear to be reasonable, with the exception of  $N_2^* + H_2O \rightleftharpoons N_2 + H_2O$  (Figure 4) and  $CO_2^*(v_2) + N_2 \rightleftharpoons CO_2 + N_2$  (Figure 6). In Figures 4 and 6, the dot-dashed curve represents a modification to the reference rates; these modifications are prompted by the post-1969 rate data. When these two rates are improved as shown, the computer code of Reference 13 yields the results shown in Figure 16, which illustrates  $G_0$  as a function of  $H_2O$

content for the given conditions. Two curves are shown, one using the old rates and the other using the improved rates. These are compared with experimental data obtained from the shock tunnel measurements by Vamos<sup>(41)</sup>. The good agreement obtained between the theory utilizing the improved rates and the experimental data seems to substantiate the two modifications which are independently based on Figures 4 and 6.

For convenience, the rates used in the gasdynamic laser computer code of Reference 13, modified by the two improved rates discussed above, are given in Appendix A of the present paper.

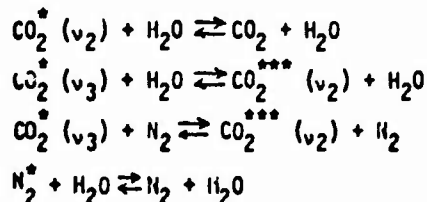
#### V. CONCLUSIONS

From the present study of the sensitivity of gasdynamic laser performance to uncertainties in the vibrational rate data, the following conclusions are made:

(1) Recent data have been compared with the rates compiled by Taylor and Bitterman<sup>(18)</sup> in 1969. This comparison shows that an inordinately large uncertainty still exists in many of the important vibrational rates used for the calculation of  $CO_2 - H_2 - H_2O$  gasdynamic laser performance.

(2) As a result of these uncertainties, present-day calculations of gasdynamic laser gain and maximum available energy are subject to at least a 25 percent inaccuracy.

(3) Because the existing rate data are not sufficient to confidently calculate gasdynamic laser performance to within a few percent, new efforts should be made to more accurately measure the  $CO_2 - H_2 - H_2O$  vibrational exchange rates. Of particular importance are the rates for



along with their proper temperature dependence.

(4) The rate of deactivation of excited  $H_2$  by  $H_2O$  is important, particularly for second generation gasdynamic lasers. In fact, it is equally as important as the effect of  $H_2O$  on  $CO_2$ . This fact has not been fully appreciated in the

past.

#### APPENDIX B

The vibrational relaxation times used for generating the theoretical curve (improved rates) in Figure 16 are given below. They are the same as appear in Appendix A of Reference 23, with the exception of the two improvements mentioned in the present report. The nomenclature is the same as References 23 and 24.

$$(\tau_a^p)_{CO_2-H_2} = 1.3 \times 10^5 (T^{-1/3})^{4.9}$$

$$(\tau_a^p)_{CO_2-CO_2} = 0.27 (\tau_a^p)_{CO_2-H_2}$$

$$(\tau_a^p)_{CO_2-H_2O} = 5.5 \times 10^{-2}$$

$$\log(\tau_b^p)_{H_2-H_2} = 93 (T^{-1/3}) - 4.61$$

$$(\tau_b^p)_{H_2-CO_2} = (\tau_b^p)_{H_2-H_2}$$

$$\log(\tau_b^p)_{H_2-H_2O} = 27.65 (T^{-1/3}) - 3.2415$$

$$\log(\tau_c^p)_{CO_2-CO_2} = 17.8 (T^{-1/3}) - 1.808$$

$$(\tau_c^p)_{CO_2-H_2} = 2(\tau_c^p)_{CO_2-CO_2}$$

$$\log(\tau_c^p)_{CO_2-H_2O} = -20.4 (T^{-1/3}) + 0.643 \quad (\text{For } T > 600^\circ K)$$

$$\log(\tau_c^p)_{CO_2-H_2O} = -20.4 (600^{-1/3}) + 0.642 = \text{constant} \quad (\text{For } 200 < T < 600^\circ K)$$

In the above correlations,  $(\tau_p)$  is in  $(\mu \text{ sec} - \text{atm})$  and  $T$  is in  $^\circ K$ .

#### REFERENCES

1. Gerry, E.T., "Gasdynamic Lasers," AIAA Paper No. 71-23 (1971).
2. Anderson, John D., Jr. and Harris, E.L., "Modern Advances in the Physics of Gasdynamic Lasers," AIAA Paper No. 72-143 (1972).
3. Anderson, John D., Jr. and Harris, E.L., "Gasdynamic Laser 2 Years Later," *Laser Focus*, Vol. 8, No. 5, May 1972, pp. 32-34.
4. Anderson, John D. Jr., "Gasdynamic Lasers: A State-of-the-Art Survey," 1972 HEREM Record, Vol. 14, pp. 180-183.
5. Lee, G. and Gowen, F.E., "Gain of  $CO_2$  Gasdynamic Lasers," *Applied Physics Letters*, Vol. 18, No. 6, 15 March 1971, pp. 237-239.
6. Lee, G., Gowen, F. and Hagen, J.R., "Gain and Power of  $CO_2$  Gasdynamic Lasers," *AIAA Journal*, Vol. 10, No. 1, January 1972, pp. 65-71.
7. Anderson, John D., Jr., Humphrey, R.L., Vamos, J.S., Plummer, M.J. and Jensen, R.E., "Population Inversions in an Expanding Gas: Theory and Experiment," *The Physics of Fluids*, Vol. 14, No. 12, December 1971, pp. 2620-2624.
8. Christiansen, W.H. and Tsongas, G.A., "Gain

- Kinetics of CO<sub>2</sub> Gasdynamic Laser Mixtures at High Pressure," The Physics of Fluids, Vol. 14, No. 12, December 1971, pp. 2611-2619.
9. Herzberg, A., Johnston, E.W. and Ahlstrom, H.G., "Photon Generators and Engines for Laser Power Transmission," AIAA Journal, Vol. 10, No. 4, April 1972, pp. 394-400.
  10. Tulip, J. and Sequin, H., "Explosion-Pumped Gas-Dynamic CO<sub>2</sub> Laser," Applied Physics Letters, Vol. 19, No. 8, 15 October 1971, pp. 263-265.
  11. Yatsiv, S., Greenfield, E., Othman-Deutsch, F., Chuchem, O., and Bin-hun, E. "Pulsed CO<sub>2</sub> Gas-Dynamic Laser," Applied Physics Letters, Vol. 19, No. 3, 1 August 1971, pp. 65-68.
  12. Meinzer, R.A., "Experimental Gas Dynamic Laser Studies," AIAA Journal, Vol. 10, No. 4, April 1972, pp. 388-393.
  13. Glowacki, Walter J. and Anderson, John D., Jr., "A Computer Program for CO<sub>2</sub>-N<sub>2</sub>-H<sub>2</sub>O Gasdynamic Laser Gain and Maximum Available Power," NOLTR 71-210, October 1971, Naval Ordnance Laboratory, White Oak, Md.
  14. Anderson, John D., Jr., "A Time-Dependent Analysis for Vibrational and Chemical Nonequilibrium Nozzle Flows," AIAA Journal, Vol. 8, No. 3, March 1970, pp. 545-550.
  15. Anderson, John D., Jr., "Time-Dependent Solutions of Nonequilibrium Nozzle Flows -- A Sequel," AIAA Journal, Vol. 8, No. 12, December 1970, pp. 2280-2282.
  16. Anderson, John D., Jr., "Time-Dependent Analyses of Population Inversions in an Expanding Gas," The Physics of Fluids, Vol. 13, No. 8, Aug. 1970, pp. 1983-1989.
  17. Taylor, R.L. and Bitterman, S., "Survey of Vibrational Relaxation Data for Processes Important in the CO<sub>2</sub>-N<sub>2</sub> Laser System," AVCO Everett Research Report 282, October 1967, AVCO Everett Research Lab., Everett, Mass.
  18. Taylor, R.L. and Bitterman, S., "Survey of Vibrational Relaxation Data for Processes Important in the CO<sub>2</sub>-N<sub>2</sub> Laser System," Reviews of Modern Physics, Vol. 41, No. 1, Jan. 1969, pp. 26-47.
  19. Hall, D.W., "A Computer Program for the Calculation of Population Inversions and Small-Signal Gain for a CO<sub>2</sub>-N<sub>2</sub>-H<sub>2</sub>O-O<sub>2</sub> Gas Dynamic Laser," unpublished internal memorandum, General Electric Co., Re-entry and Environmental Systems Division, Philadelphia, Pa.
  20. Rosser, W.A., Jr., Hoag, E. and Gerry, E.T., "Relaxation of Excess Populations in the Lower Laser Level CO<sub>2</sub> (100)," Journal of Chemical Physics, Vol. 57, No. 10, 15 Nov. 1972, pp. 4153-4164.
  21. Bulthius, K., "Laser Power and Vibrational Energy Transfer in CO<sub>2</sub> Lasers," Journal of Chemical Physics, Vol. 58, No. 12, 15 June 1973, pp. 5786-5794.
  22. DeTemple, T.A., Suhre, D.R. and Coleman, P.D., "Relaxation Rates of Lower Laser Levels in CO<sub>2</sub>," Applied Physics Letters, Vol. 22, No. 8, 15 April 1973, pp. 349-350.
  23. Anderson, John D., Jr., Humphrey, R.L., Vamos, J.S., Plummer, M.J. and Jensen, R.E., "Population Inversions in an Expanding Gas: Theory and Experiment," NOLTR 71-116, June 1971, Naval Ordnance Laboratory, White Oak, Md.
  24. Anderson, John D., Jr., "A Time-Dependent Quasi-One-Dimensional Analysis of Population Inversions in an Expanding Gas," NOLTR 69-200, Dec. 1969, Naval Ordnance Laboratory, White Oak, Md.
  25. Anderson, John D., Jr., "Sensitivity of Gasdynamic Laser Calculations to Uncertainties in Kinetic Rates," Tech. Report AE 73-2, October 1973, Department of Aerospace Engineering, University of Maryland, College Park, Md.
  26. Bulthius, K. and Ponsen, G.J., "Vibrational Relaxation of the CO<sub>2</sub> Lower Laser Level by H<sub>2</sub>O," Physics Letters, Vol. 36A, No. 2, 16 Aug. 1971, pp. 123-124.
  27. Bulthius, K. and Ponsen, G.J., "On the Relaxation of the Lower Laser Level of CO<sub>2</sub>," Chemical Physics Letters, Vol. 14, No. 5, July 1972, pp. 613-615.
  28. Buchwald, M.I. and Bauer, S.H., "Vibrational Relaxation in CO<sub>2</sub> with Selected Collision Partners. I. H<sub>2</sub>O and D<sub>2</sub>O," Journal of Physical Chemistry, Vol. 76, No. 22, October 1972, pp. 3108-3115.
  29. Sharma, R.U., unpublished data provided to the present author by R.L. Taylor, Physical Sciences, Inc., Wakefield, Mass., Aug. 1973.
  30. von Rosenberg, C.W., Bray, K.N.C. and Pratt, H.H., "Shock Tube Vibrational Relaxation Measurements: N<sub>2</sub> Relaxation by H<sub>2</sub>O and the CO<sub>2</sub>-N<sub>2</sub> V-V Rate," Journal of Chemical Physics, Vol. 56, No. 7, 1 April 1972.
  31. Evans, L.B., "Vibrational Relaxation in Moist Nitrogen," The Journal of the Acoustical Society of America, Vol. 51, No. 1 (Part 2), 1972, pp. 409-411.
  32. Rosser, W.A., Jr. and Gerry, E.T., "De-excitation of Vibrationally Excited CO<sub>2</sub> (v<sub>3</sub>) by Collisions with He, O<sub>2</sub> and H<sub>2</sub>O," Journal of Chemical Physics, Vol. 51, 1969, pp. 2286-2287.
  33. Heller, D.F. and Moore, C.B., "Relaxation of

the Asymmetric Stretching Vibration of  $\text{CO}_2$  by Collisions with  $\text{H}_2\text{O}$ ,  $\text{D}_2\text{O}$  and  $\text{HCO}$ ," Journal of Chemical Physics, Vol. 52, No. 2, Jan. 1970, pp. 1005-1006.

34. Shields, F.D., Warf, C.C. and Bass, H.E., "Acoustical Method of Obtaining Vibrational Transition Rates Tested on  $\text{CO}_2/\text{N}_2$  Mixtures," Journal of Chemical Physics, Vol. 58, No. 9, 1 May 1973, pp. 3837-3840.
35. Merrill, K.M. and Anne, R.C., "Deactivation of the  $\text{CO}_2$  Bending Mode by Collisions with  $\text{H}_2$  and  $\text{N}_2$ ," Journal of Chemical Physics, Vol. 51, No. 2, 15 July 1969, pp. 844-846.
36. Bauer, H.J. and Schotter, R., "Collision Transfer of Vibrational Energy from Nitrogen and Methane to the Carbon Dioxide Molecule," Journal of Chemical Physics, Vol. 51, No. 8, 15 October 1969, pp. 3261-3270.
37. Eckstrom, D.J. and Bershader, D., "Vibrational Relaxation of the Bending Mode of Shock-Heated  $\text{CO}_2$  by Laser-Absorption Measurements," Journal of Chemical Physics, Vol. 57, No. 2, July 1972, pp. 632-638.
38. Rosser, W.A., Jr., Wood, A.D. and Gerry, E.T., "Deactivation of Vibrationally Excited Carbon Dioxide ( $\nu_3$ ) by Collision with Carbon Dioxide or with Nitrogen," Journal of Chemical Physics, Vol. 50, No. 11, 1 June 1969, pp. 4996-5008.
39. Reid, J., Garside, B.K. and Ballik, E.A., "Vibrational Relaxation Measurements in  $\text{CO}_2$  Employing an Incremental TEA Laser Gain Technique," IEEE Journal of Quantum Electronics, Vol. QE-9, No. 6, June 1973, pp. 602-604.
40. Serry, D.J., "Intramolecular Energy Transfer in  $\text{CO}_2$ ," Journal of Chemical Physics, Vol. 56, No. 9, May 1972, pp. 4714-4715.
41. Vamos, John S., "Small-Signal Gain Measurements in a High-Area Ratio Nozzle Shock Tunnel GDL," AIAA Paper to be presented at the AIAA 12th Aerospace Sciences Meeting, Jan. 1974.

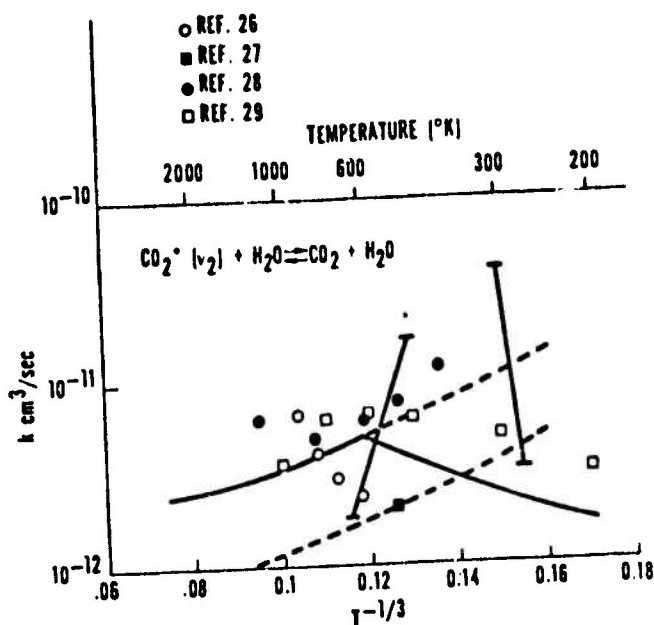


Fig. 1: Rate constant versus temperature; deactivation of the lower laser level by  $\text{H}_2\text{O}$

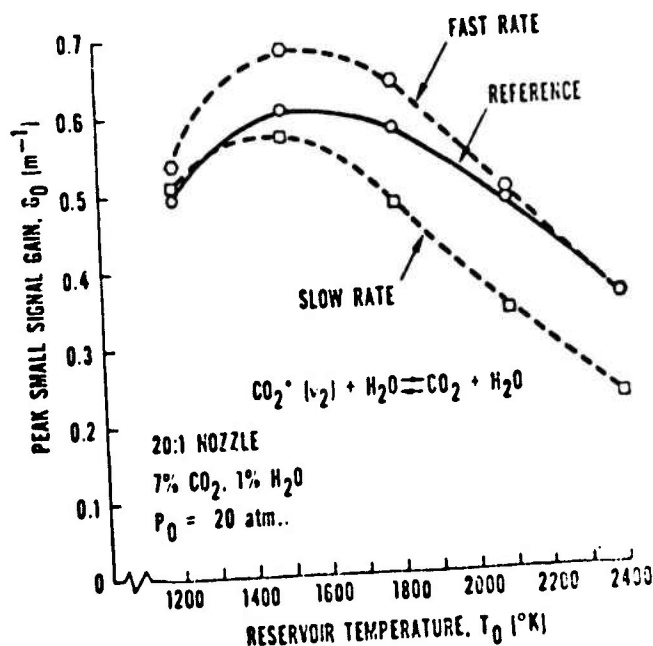


Fig. 2: Gain versus temperature; effect of reaction 1 on a first generation gasdynamic laser

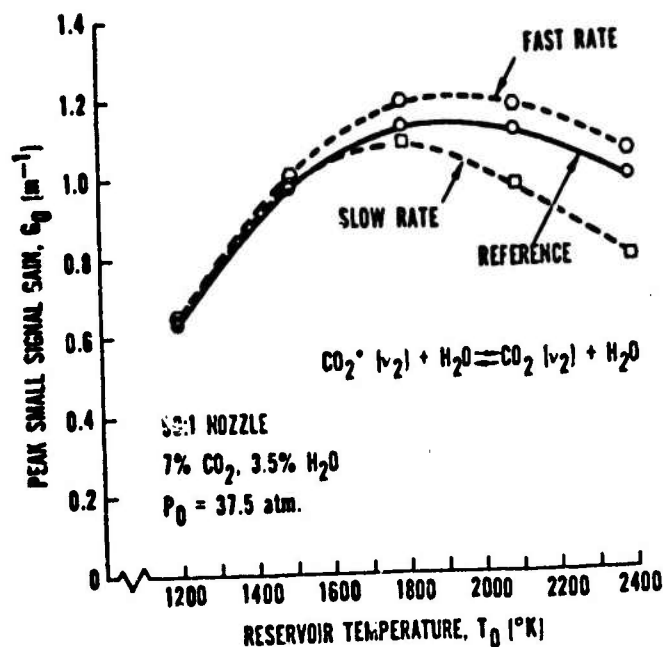


Fig. 3: Gain versus temperature; effect of reaction 1 on a second generation gas-dynamic laser, 3.5% H<sub>2</sub>O

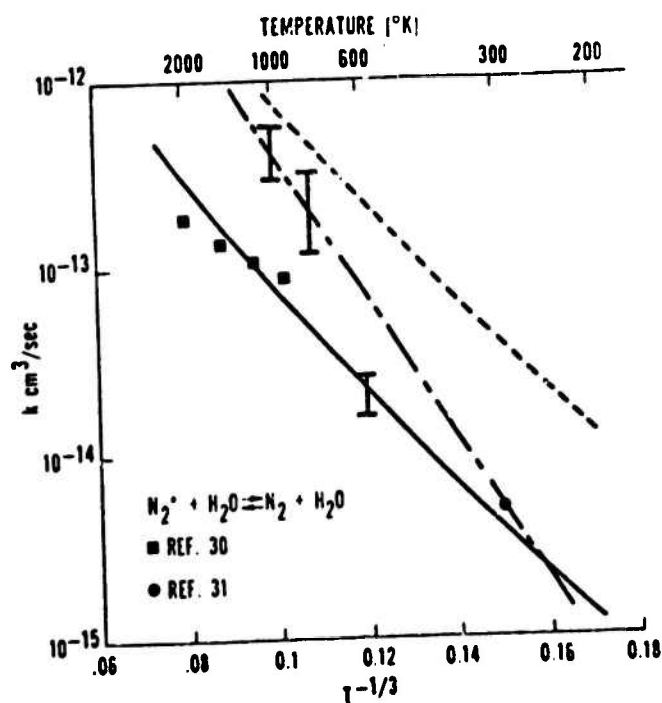


Fig. 4: Rate constant versus temperature; deactivation of H<sub>2</sub> by H<sub>2</sub>O

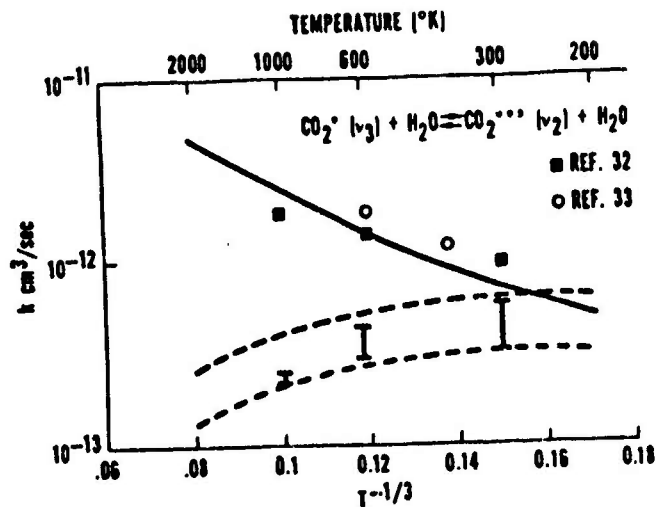


Fig. 5: Rate constant versus temperature; deactivation of the upper laser level by H<sub>2</sub>O

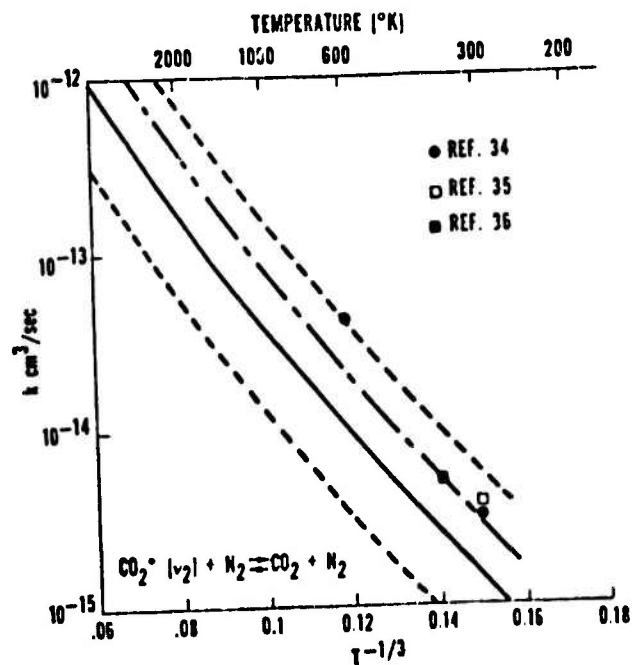


Fig. 6: Rate constant versus temperature; deactivation of the lower laser level by H<sub>2</sub>

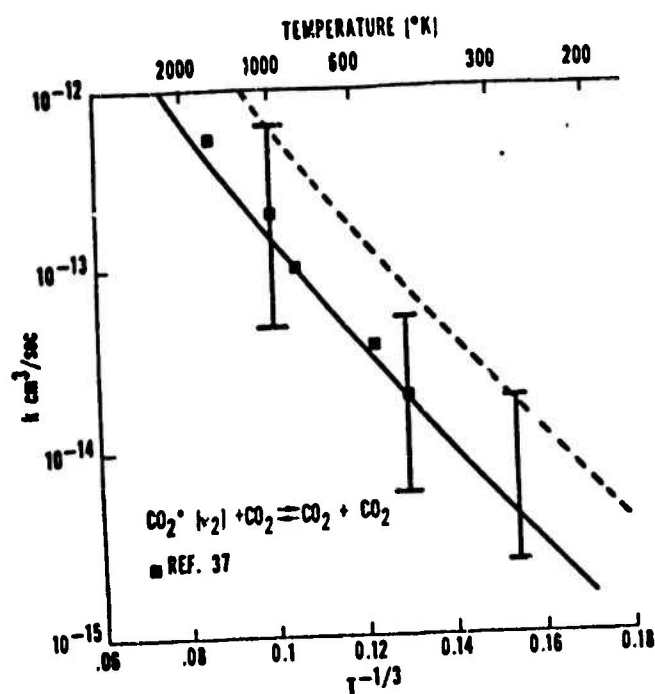


Fig. 7: Rate constant versus temperature; deactivation of the lower laser level by  $\text{CO}_2$

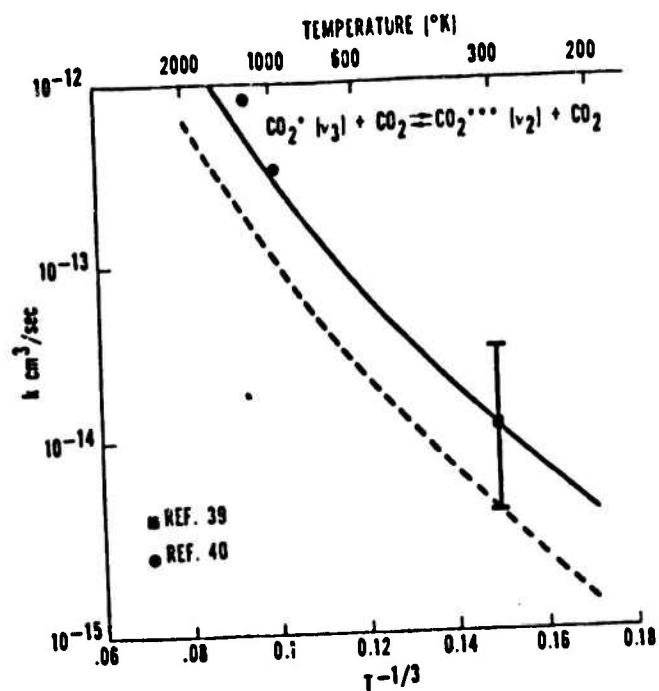


Fig. 9: Rate constant versus temperature; deactivation of the upper laser level by  $\text{CO}_2$

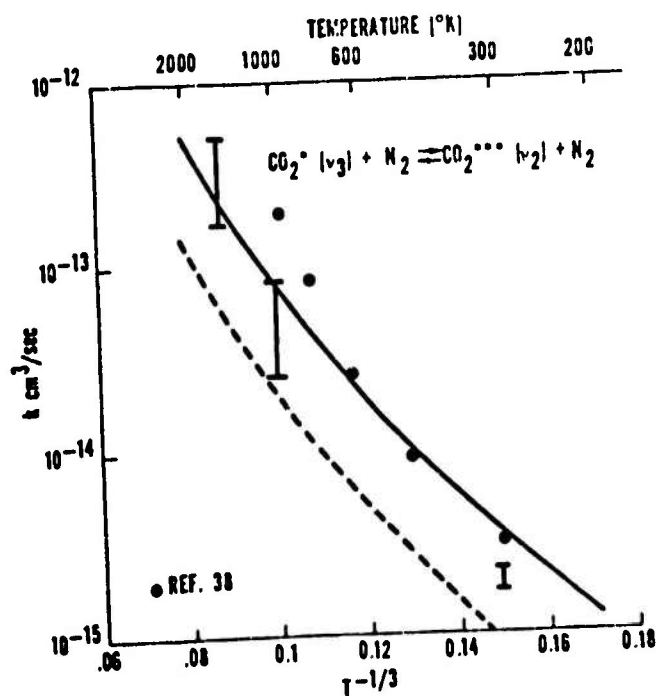


Fig. 8: Rate constant versus temperature; deactivation of the upper laser level by  $\text{N}_2$

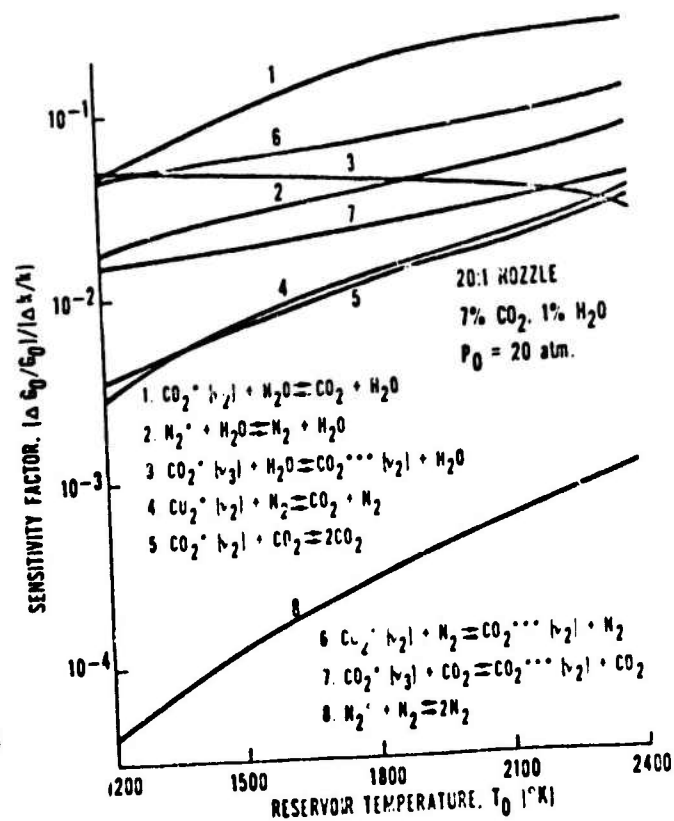


Fig. 10: Gain sensitivity factor; first generation gasdynamic laser

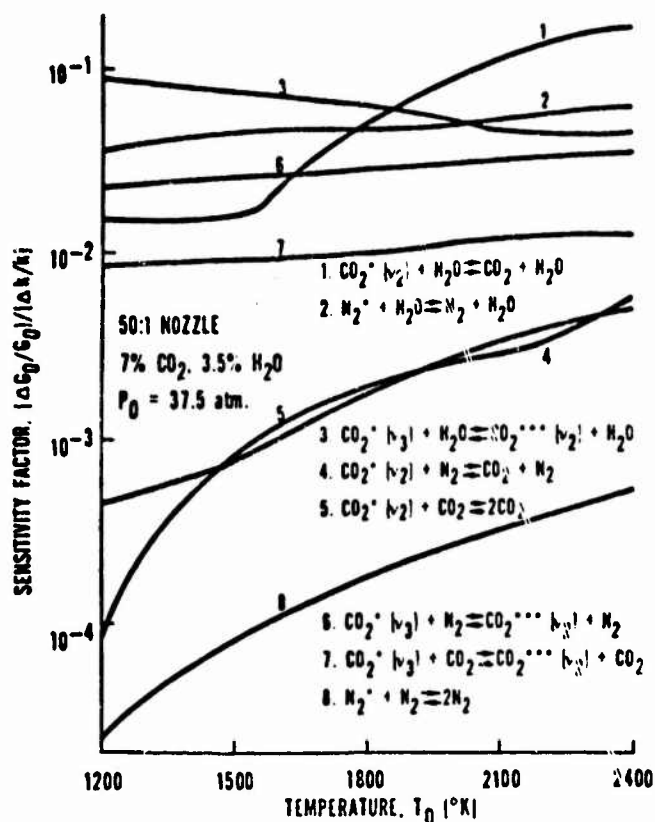


Fig. 11: Gain sensitivity factor; second generation gasdynamic laser

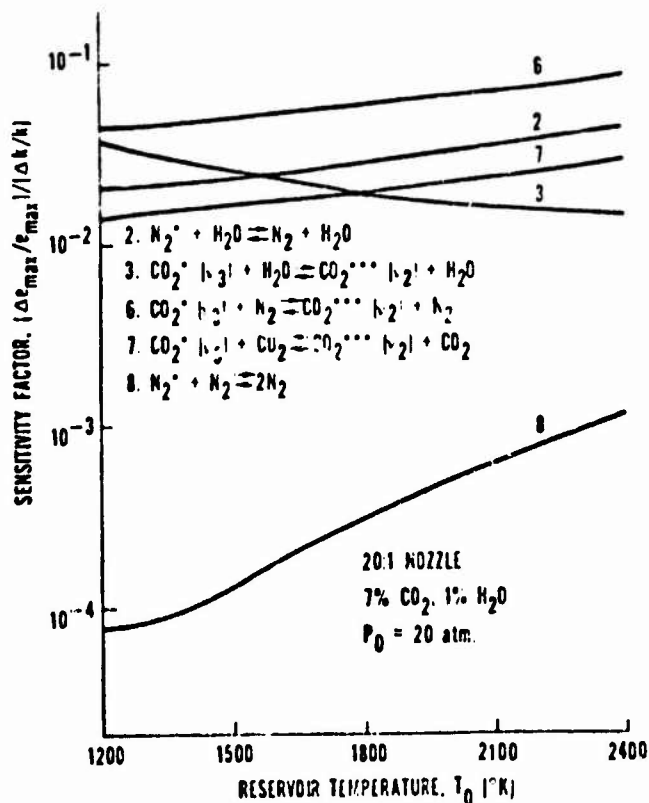


Fig. 12: Maximum available energy sensitivity factor; first generation gasdynamic laser

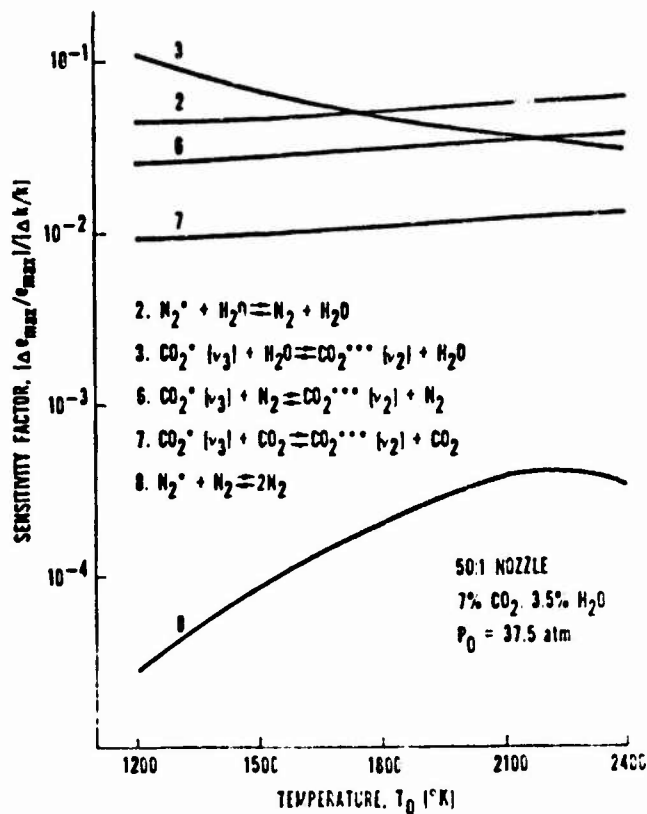
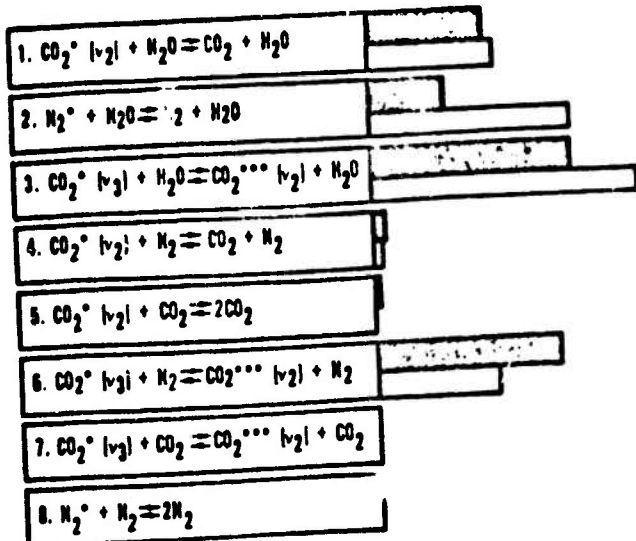


Fig. 13: Maximum available energy sensitivity factor; second generation gasdynamic laser

PERCENT UNCERTAINTY IN  
SMALL SIGNAL GAIN

0 10% 20% 30%



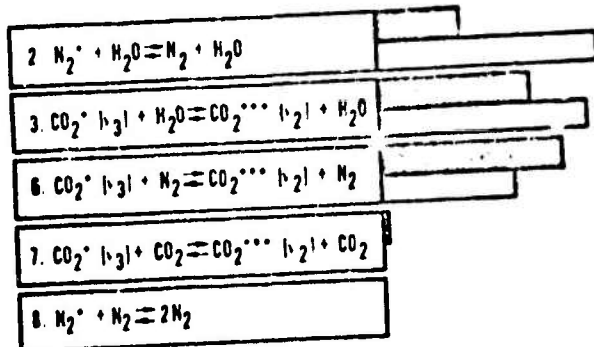
20:1 NOZZLE,  $P_0 = 20$  atm.,  $T_0 = 1200^\circ\text{K}$

50:1 NOZZLE,  $P_0 = 37.5$  atm.,  $T_0 = 1800^\circ\text{K}$

Fig. 14: Uncertainty in small-signal gain

PERCENT UNCERTAINTY IN  
MAXIMUM AVAILABLE POWER

0 10% 20% 30%



20:1 NOZZLE,  $P_0 = 20$  atm.,  $T_0 = 1200^\circ\text{K}$

50:1 NOZZLE,  $P_0 = 37.5$  atm.,  $T_0 = 1800^\circ\text{K}$

Fig. 15. Uncertainty in maximum available energy

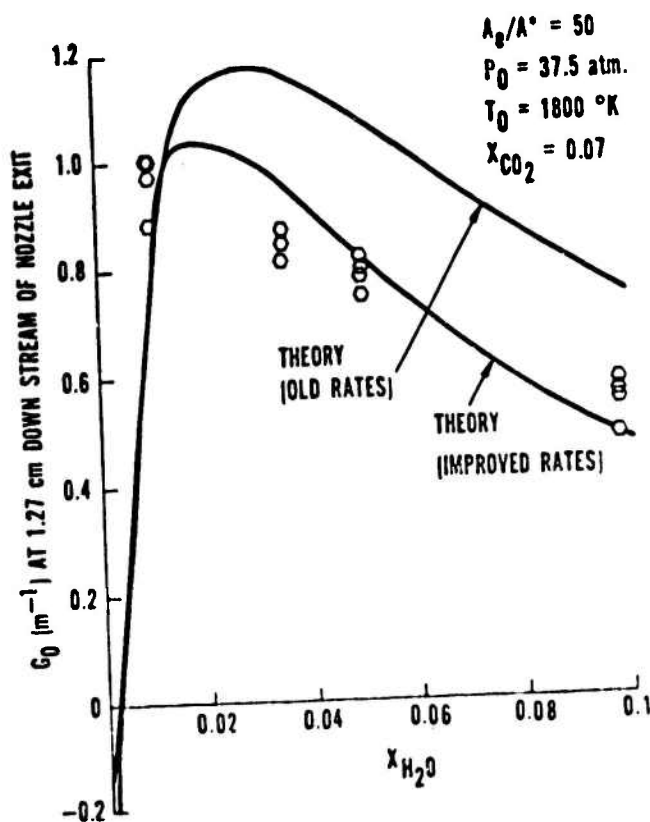


Fig. 16: Gain versus  $\text{H}_2\text{O}$  content; comparison between theory and experiment

# INVESTIGATION OF A MIXING CO<sub>2</sub> GDL

by

J.P.E. Taran, M. Charpenel and R. Borghi

Office National d'Etudes et de Recherches Aéronautiques  
92320 Châtillon (France)

## Abstract

Practical nozzle configurations for a mixing CO<sub>2</sub> GDL have been investigated numerically and experimentally. One particular configuration gave excellent results: pure hot N<sub>2</sub> is expanded through a two-dimensional Mach 5 supersonic nozzle, while a mixture of cold CO<sub>2</sub> and He is injected at the throat. The experiment was done with an arc heater providing a 100 g/s, 2000-4000°K flow of N<sub>2</sub>. Good mixing was obtained, and gain constants greater than 0.03 cm<sup>-1</sup> were measured. A laser cavity was also operated, at an estimated efficiency close to 2%.

## I. Introduction

CO<sub>2</sub> gas-dynamic lasers are considered to have comparatively poor efficiencies. Their efficiency is typically 1%, which is small compared with the 10% figure characteristic of electrical CO<sub>2</sub> lasers. The overall efficiency of a gas-dynamic laser can be written as the product of two factors,  $\eta = \eta_{th} \times \eta_{opt}$ ,  $\eta_{th}$  representing the thermodynamic part of the efficiency and  $\eta_{opt}$  the efficiency of the optical cavity. The term  $\eta_{th}$  itself further separates into two contributions  $\eta_{th} = \eta_{vib} \times \eta_{fr}$ , where  $\eta_{vib}$  is the fraction of the initial enthalpy that goes into the vibration of N<sub>2</sub> and mode  $v_2$  of CO<sub>2</sub>, and  $\eta_{fr}$  the friction efficiency of the nozzle.

There exists a number of ways of increasing  $\eta_{th}$ .  $\eta_{vib}$  can be increased by raising the stagnation temperature  $T_1$ , going from 1500°K to 4000°K doubles  $\eta_{vib}$  (Fig.1). On the other hand,  $\eta_{fr}$  improves as the CO<sub>2</sub> and H<sub>2</sub>O or He contents are reduced; it also improves if the nozzle throat is narrowed. Unfortunately, there are limits to these improvements: the optical cavity efficiency demands a minimum CO<sub>2</sub> and He or H<sub>2</sub>O contents, while boundary layers set a lower limit to the throat height. Since  $\eta_{fr}$  is a decreasing function of  $T_1$ , an optimum  $T_1$  is to be found which maximizes the product  $\eta_{th} = \eta_{vib} \times \eta_{fr}$ . This optimum  $T_1$  lies in the vicinity of 2000°K (1,2).

Further improvements should be obtainable, though, if one were able to produce the hot N<sub>2</sub> and expand it prior to mixing with cold CO<sub>2</sub> and He or H<sub>2</sub>O. This idea, which has been suggested originally in the proposal of the GDL (3,4), is difficult to put into practice.

We have investigated two practical arrangements for the mixing of supersonic flows in a CO<sub>2</sub> GDL. The first type of arrangement, where mixing is made in a constant area duct after complete supersonic expansion of the N<sub>2</sub> flow, is found to give poor results (5). The second type of arrangement, with mixing around the throat, was predicted and experimentally verified to give excellent results (6).

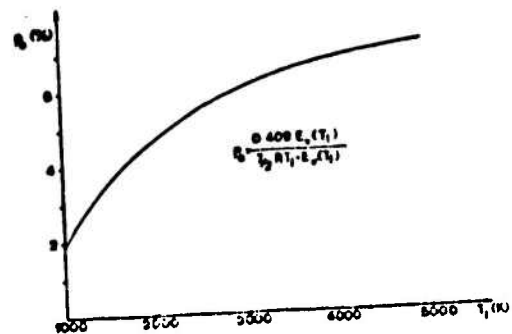


Figure 1 - Plot of the usable fraction of N<sub>2</sub> enthalpy versus stagnation temperature  $T_1$ ;  $E_v$ : vibrational energy; numerical factor; quantum efficiency.

## II. Mixing design

Figure 2 is a diagram of a two dimensional mixing assembly where a slightly supersonic flow of pre-mixed CO<sub>2</sub> and He is mixed with a high (4 to 6) Mach number flow of pure N<sub>2</sub> in a constant area channel. This arrangement is in essence similar to that of Spencer and coworkers (7) for the HF chemical laser, or even that of Bronfin et al (8), but the static pressures are much higher here (100 : 5 approximately). The system presents a number of drawbacks:

- it is difficult to achieve rapid mixing at the higher pressures appropriate for a GDL with atmospheric pressure recovery, although some flexibility is afforded in the selection of the relative Mach numbers and the convergence angle of the flows;
- strong shocks will form at the side of the corner nozzle wall, causing optical distortions;
- the static temperature in the mixing region is raised to high values by the collision of the fast N<sub>2</sub> stream with the slower stream of cold He and CO<sub>2</sub> (2,4) resulting in a loss of optical gain and power.



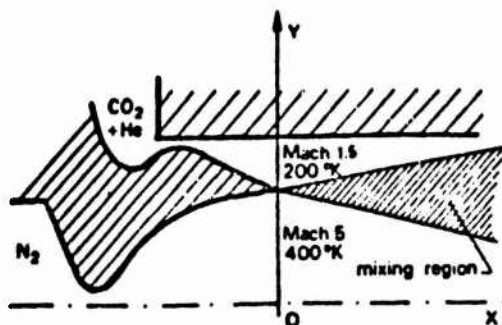


Figure 2 - Diagram of a supersonic mixing nozzle with  $\text{CO}_2$  injection after expansion of  $\text{N}_2$ .

The aerodynamic picture improves as the injection port is moved upstream; mixing is initiated earlier, and the shock waves lose their strength; further, the loss of vibrational energy in the mixing zone should not increase excessively. However, one does not want to inject  $\text{CO}_2$  and He far upstream of the throat, since the advantage of mixing would be lost. Injection at the throat or slightly downstream offers a reasonable compromise (Fig. 3). Injection on the axis is preferred here, rather than injection through the walls, in order to avoid the presence of  $\text{CO}_2$  in the boundary layers; this is of importance if the laser beam is to traverse these boundary layer, as in a multiple parallel nozzle system for instance. A similar system has been described recently by Greshko and coworkers<sup>(9)</sup>.

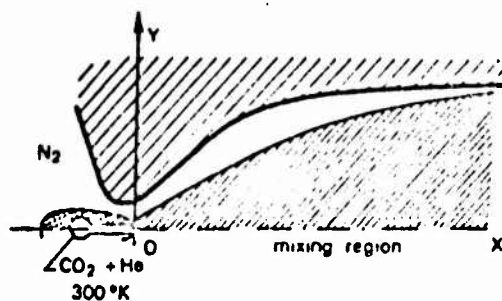


Figure 3 - Diagram of a nozzle with injection at the throat.

The injection slot is located at a point where the  $\text{N}_2$  Mach number is of the order of 1.2. Cold premixed  $\text{CO}_2$  and He are introduced at sonic velocities into the  $\text{N}_2$ . The near equality of the pressures of both flows will minimize the onset of shocks and their low velocities permit their smooth mixing. Down to the point where the injection is made, the  $\text{N}_2$  coming from the stagnation chamber retains about 90% of its initial vibrational energy owing to its long relaxation time in the absence of the He and  $\text{CO}_2$  contaminants<sup>(10)</sup>. In the subsequent portion of the flow, the largest fraction of the collisional deactivation of the  $\text{N}_2$  is caused by the  $\text{CO}_2$  and He, in the immediate vicinity of the injector, where the static temperature is still

high. A few centimeters downstream of the throat, most of the initial  $\text{N}_2$  vibrational energy has been frozen while the  $\text{CO}_2$  + He and the  $\text{N}_2$  have completed their mixing. The  $\text{N}_2$  has shared its vibrational energy with mode  $\nu_2$  of  $\text{CO}_2$ , causing a high population inversion and creating a large optical gain.

It should be stressed that other advantages are also seen in the injection of room temperature  $\text{CO}_2$  and He. Firstly, it represents a saving in initial enthalpy, and therefore an increase in thermodynamic efficiency; secondly, as the  $\text{CO}_2$  and He expand, their temperature is lowered further, thus lowering the  $\text{N}_2$  static temperature as they diffuse into it. Smaller area ratio nozzles can then be selected for a given final static temperature.

These qualitative understandings have been substantiated by numerical calculations, which were conducted in order to characterize various nozzle designs in terms of mixing efficiency, gain constant and optical power available.

### III. Numerical calculations

The program treats the case of steady state two-dimensional turbulent supersonic mixing in a fashion similar to the Patankar and Spalding method<sup>(11)</sup> for subsonic flows. Modifications have been made in order to account for the supersonic nature of the flows and the divergence of the nozzle. Nevertheless, instabilities render calculations at the throat impossible.

The equations of motion include conservation of axial momentum, species, and total enthalpy; the terms of momentum, species and enthalpy transfer resulting from turbulence are expressed according to the simple Prandtl theory<sup>(12)</sup> and depend on an experimental determination of a mixing length constant. In addition, equations are provided for the vibrational energy exchange between the various molecular species. For that purpose, a vibrational model inspired from the model proposed by H.G. Easov et al<sup>(13)</sup> for the  $\text{CO}_2$  and  $\text{N}_2$  molecules has been adopted<sup>(14)</sup>. Three vibrational modes are considered, namely  $\nu_1$  (for  $\text{N}_2$ ),  $\nu_2$  of  $\text{CO}_2$ , and the group of

modes  $\nu_1$  and  $\nu_2$  of  $\text{CO}_2$  which are known to be tightly coupled. The energy exchange between the vibrational modes and translation is described by the equations of Ref. 13, while the rate constants are taken from Taylor and Bittormann's review paper<sup>(10)</sup>. It has also been assumed for simplicity that there are no fluctuations in these terms resulting from turbulence, and therefore the mean values of the parameters (concentration, temperature, etc.) can be taken at each particular location.

The boundary conditions are those that reign the supersonic streams, which have equal static pressures, and which come into contact at the injection plane: the Mach 1  $\text{CO}_2$  + He flow is supposed to be in equilibrium at room temperature, while the velocity,

density, static and vibrational temperatures for the  $\text{N}_2$  flow are supplied by a program developed for premixed  $\text{N}_2$ - $\text{CO}_2$ -He flows typical of standard CDL<sup>(14)</sup> with the  $\text{CO}_2$  and He concentrations being set at zero. Integration of the von Mises transformed partial differential equations is then carried out from the injection plane downstream, with an implicit numerical scheme. The computing time is approximately 12 minutes on an IEM 360-50 computer for an axial distance of 15 cm. Note that Spencer and coworkers<sup>(7)</sup> also worked out a similar program for their HF laser. The main differences lie in their explicit scheme and their constant pressure assumption.

Typical results for the arrangement in Fig. 2 are presented in Fig. 4 and 5. As expected, a large temperature increase is found in the mixing region, and the gains are small and unevenly distributed.

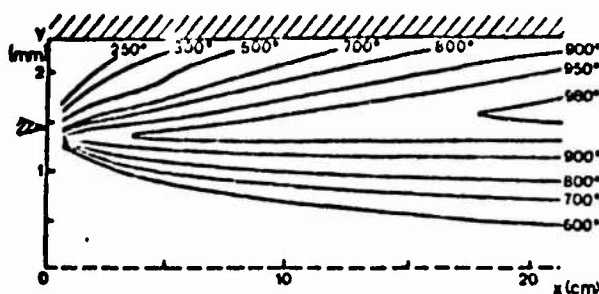


Figure 4 - Temperature distribution for supersonic mixing of a Mach 5  $\text{N}_2$  flow at 500 °K with a Mach 1, 250 °K, pure  $\text{CO}_2$  flow. Note the x and y scales are different.

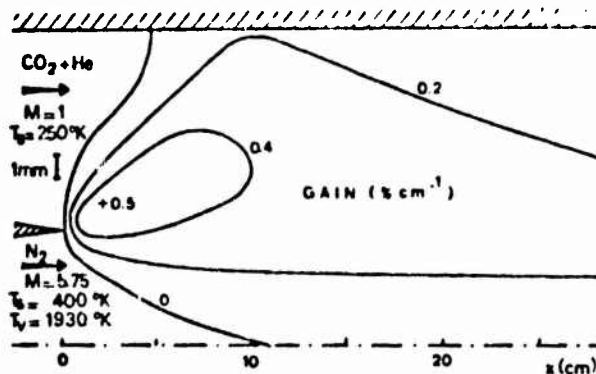


Figure 5 - Gain distribution for supersonic mixing of a Mach 5.75, 400 °K static temperature and 1930 °K vibrational temperatures  $\text{N}_2$  flow with a 10%  $\text{CO}_2$ , 90% He flow at Mach 1 and 250 °K. Gain was calculated for the P 30 line (optimum gain is slightly larger for lines P 22 - P 24).

On the contrary, large gains are set up across the flow for the arrangement of Fig. 3. One can see (Fig. 6) that the distribution is quite uniform and that the gain does not fall off along the flow direction. The calculations further indicate that the

freezing efficiency  $\eta_f$  approaches 80%, with a net efficiency  $\eta_{th}$  of 4%.

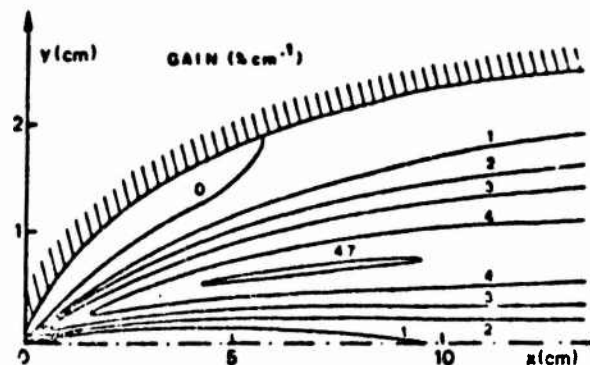


Figure 6 - Gain distribution on the P 16 line for mixing at the throat. The stagnation conditions for  $\text{N}_2$  are 2500 °K and 15 atm. The 30%  $\text{CO}_2$ , 70% He mixture is at room temperature; the half slot height of the injector is 0.3 mm. The throat height for the  $\text{N}_2$  (between the injector and one nozzle wall is 0.7 mm). Flow proportions are 44%  $\text{N}_2$ , 39% He, 17%  $\text{CO}_2$ .

#### IV. Experimental results

Both types of mixing nozzles were tested. A d.c. 2 MW arc heater provided a 100 g/s flow of  $\text{N}_2$  at temperatures ranging from 2000 to 4000 °K. We failed to detect any appreciable optical gain with the first type of arrangement in a 4 cm wide two-dimensional channel, as had been anticipated.

The mixing assembly for the other arrangement is sketched in Fig. 7. The throat height for the  $\text{N}_2$  is approximately 0.8 mm on either side of the injector. Various injectors were tested, with 0.8 mm diameter injection holes oriented either on axis as in Fig. 7 (injector I), or alternately up and down at an angle of 22° from the mid plane for a better mixing (injector II); all the holes were spaced at 1.2 mm apart.

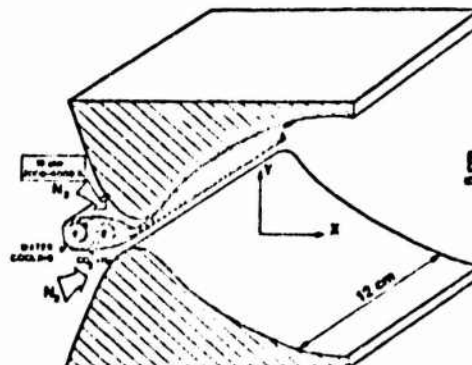


Figure 7 - Sketch of a Mach 5 nozzle with  $\text{CO}_2$  injection at the throat; the initial supersonic expansion angle is 7°. The nozzle has a 10 cm long divergent profile plus another 10 cm long parallel section.

### Mixing

The mixing of the two flows was investigated. Samples were taken simultaneously at various positions in the flow and subsequently analysed with a gas chromatograph. Figure 8 gives a typical profile versus position  $y$  across nozzle for injector II at a distance  $x = 19$  cm from the nozzle throat.

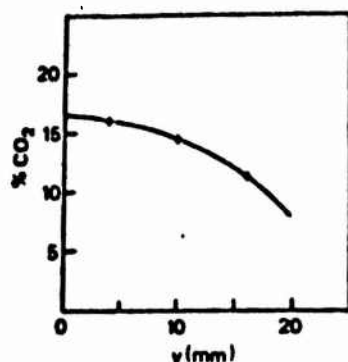


Figure 8 -  $\text{CO}_2$  mole fraction 19 cm downstream from the throat, for the injection at the throat (the He concentration is proportional to that of  $\text{CO}_2$ ). The  $\text{N}_2$  stagnation temperature is 2000°K, with mean proportions of 46%  $\text{N}_2$ , 15%  $\text{CO}_2$  and 39% He.

### Optical homogeneity

Schlieren pictures of the flow have been taken with 1  $\mu\text{s}$  exposure times, revealing the absence of shocks; the turbulence level of the mixed flows was not found to exceed significantly that of the pure heated  $\text{N}_2$  with the injector removed from the throat.

### Gain measurements

The gain measurements were carried out with the equipment described in Ref. 14. The measurements were made with the probe beam parallel to the nozzle throat, at  $x = 15$  cm. No significant changes in the profiles could be found from  $x = 10$  cm to  $x = 19$  cm. The lower halves of the gain profiles are plotted in Fig. 9 versus the distance  $y$  from the mid-plane. For injector I, the experimental points (open circles) compare well with theory (solid curve), assuming effective throat heights of 0.8 mm for  $\text{N}_2$  and 0.15 mm for  $\text{CO}_2 + \text{He}$ , with respective stagnation temperatures of 2000°K and 3000°K. The mixing constant was taken as a fitting parameter, and a value of 0.03 was selected for it. Injected constituent proportions ( $\text{N}_2/\text{CO}_2/\text{He}$ ) are, in moles, (66/15/25), but local proportions in the flow vary from these figures. A central dip appears on the experimental gain distribution (at  $y = 0$ ), but less markedly than on the theoretical profile; this can be attributed to the difference between the actual injector design, which is composed of a series of holes, and the simple slit injector model taken for the calculation. The

actual injector permits  $\text{N}_2$  to penetrate into the mid-plane between the injection holes.

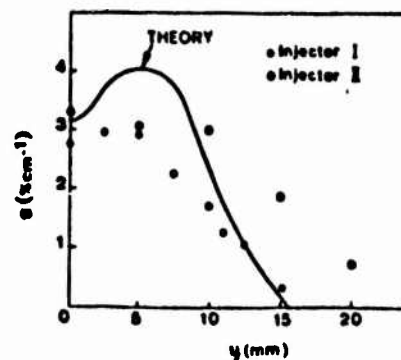


Figure 9 - Gain distributions across the nozzle, at  $x = 15$  cm downstream from the throat.

For injector II (heavy dots), one can see that the mixing is more efficient. The data (taken for the conditions of Figure 8) confirm that the mixing is near satisfactory for  $|y| < 15$  mm. The stagnation temperature is 2000°K, the freezing efficiency is of the order of 80%, mean injected constituent proportions (46/15/39) being adjusted for maximum gain; the stagnation pressures are 9 and 14 atm for  $\text{N}_2$  and  $\text{CO}_2 + \text{He}$  respectively. The slightly higher stagnation pressure for  $\text{CO}_2 + \text{He}$  permits deeper penetration into  $\text{N}_2$ . Data taken with the same injector, but with a 3000°K stagnation temperature, 80 g/s  $\text{N}_2$  mass flow rate and a (45/12/43) mixture are presented in Figure 10. The large gains one observes can be maintained up to 4000°K temperature, provided the  $\text{CO}_2$  mole fraction is lowered to 10% approximately.

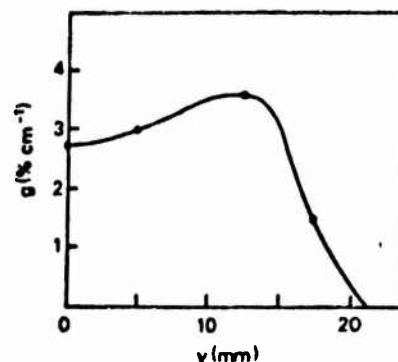


Figure 10 - Gain distribution for a 3000°K  $\text{N}_2$  stagnation temperature with a lower  $\text{CO}_2$  mole fraction.

### Oscillator experiments

A laser cavity was also operated, with a stable resonator configuration. The mirrors had to be recessed somewhat from the flow, in order to avoid damage by the numerous solid particles from the

are-heater carried by  $H_2$ . Various output mirrors were tested, including Ge or double NaCl plate, and hole coupled reflectors. A cw power of 2 kW was obtained with the Ge, in a well collimated 2.5 cm dia beam, for a stagnation temperature of 2800°K. Rough calculations, based on the 120 kW enthalpy fed to the  $H_2$  which actually flows through the cavity and contributes to the optical power, give an efficiency of 1.6% and a specific power of 25 kW per kg/s. These figures compare well with values of 0.4% and 4 kW per kg/s respectively obtained by Gerry (15).

### V. Conclusion

Extremely promising results have been obtained with a mixing  $CO_2$  GDL. Nevertheless, a number of experiments remain to be done on this system.

- 1) A combustion powered system is preferable, since the arc heater is not very efficient. One might use the combustion of  $C_2H_2$  and  $H_2O_2$ , which gives a mixture of  $H_2$  and CO at 1000°K for 2 : 1 proportions. Although CO is not expected to ruin the efficiency, some loss may occur through collisional deactivation of  $CO_2$  in the mixing zone.
- 2) Even though the He mole fraction is quite low, it seems preferable to replace it by  $H_2O$  or  $H_2$  for reduced operating costs.
- 3) The stagnation pressures must be raised for diffuser exhaust into the atmosphere. With a Mach number of 5, a stagnation pressure of 30 atm is needed for  $H_2$ .

Finally, this mixing technique might also prove useful for chemical mixing and electrical mixing lasers (7,8, 16), by allowing larger gas pressures and better optical homogeneities.

### References

1. Anderson, Jr., J.D. and Leroy Harris, E., "Modern Advances in the Physics of Gas Dynamic Lasers", AIAA paper No. 72-143 (1972).
2. Greenberg, R.A., Schneiderman, A.M., Abouse, D.R., and Parmentier, E.N., "Rapid Expansion Nozzles for Gas Dynamic Lasers", AIAA Journal, Vol. 10, No 11, Nov. 1972, pp 1494-1498.
3. Wisniewski, E.E., Fein, M.E., Verdeyen, J.T., and Cherrington, B.E., "Thermal Production of Population Inversion in Carbon Dioxide", Applied Physics Letters, Vol. 12, No 8, Apr. 1968, pp 257-259.
4. Basov, N.G., Oraevskii, A.N., and Shcheglov, V.A., "Production of a Population Inversion in Molecules of a Working Gas Mixed with a Thermally Excited Auxiliary Gas", Zhurnal Tekhnicheskoi Fiziki, Vol. 40, No 1, Jan. 1970, pp 173-180 [Soviet Physics-Technical Physics, Vol. 15, No 1, July 1970, pp 126-130].
5. Borghi, R., and Charpenel, M., "Le Mélange à Grande Vitesse d'Azote Excité en Vibration avec du Gaz Carbonique", Astronautica Acta, Vol. 17, No 4, 5, May 1972, pp 833-842.
6. Borghi, R., Carrega, A.F., Charpenel, M., and Taran, J.-P.E., "Supersonic Mixing Nozzle for Gas Dynamic Lasers", to be published in Applied Physics Letters.
7. Spencer, D.J., Mirels, H., Jacobs, T.A., and Grose, R.W.F., "Preliminary Performance of a cw Chemical Laser", Applied Physics Letters, Vol. 16, No 6, Mar. 1970, pp 235-237. ; King, W.S., and Mirels, H., "Numerical Study of a Diffusion Type Chemical Laser", AIAA Paper No 72-146 (1972).
8. Bronfin, B.R., Boedeker, L.R., and Choyer, J.P., "Thermal Laser Excitation by Mixing in a Highly Convective Flow", Applied Physics Letters, Vol. 16, No 5, Mar. 1970, pp 214-217.
9. Greshko, V.N., Soloukhin, R.I., and Wolanski, P., "Population Inversion by Mixing in a Shock Tube Flow", Optics Communications, Vol. 6, No 3, Nov. 1972, pp 275-277.
10. Taylor, R.L., and Eitterman, S., "Survey of Vibrational Relaxation Data for Processes Important in the  $CO_2 - N_2$  Laser System", Reviews of Modern Physics, Vol. 41, No 1, Jan. 1969, pp 26-47.
11. Patankar, S.V., and Spalding, D.B., "Heat and Mass Transfer in Boundary Layers", Intertext Books, London (1970).
12. Zvandil, L., "Über die ausgebildete Turbulenz", Zeitschrift für Mathematik und Mechanik, Vol. 5, 1925, p. 175.
13. Basov, N.G., Mikhailov, V.G., Oraevskii, A.N., and Shcheglov, V.A., "Molecular Population Inversion in the Supersonic Flow of a Binary Gas in a Laval Nozzle", Zhurnal Tekhnicheskoi Fiziki, Vol. 38, No 12, Dec. 1968, pp 2031-2041 [Soviet Physics - Technical Physics, Vol. 13, No 12, Jun. 1969, pp 1630-1636].
14. Andraud-Thoms, M., Carrega, A.F., Leuchter, O., and Taran, J.-P.E., "Laser Thermique à Haute Pression avec Réchauffage par Compression", La Recherche Aéronautique, Vol. 151, No 6, Dec. 1972, pp 325-332.
15. Gerry, E.T., "Gas Dynamic Lasers", American Physical Society Meeting, Washington, 29 April 1970.
16. Brunot, H., and Mabru, M., "Electrical  $CO_2$ -mixing Gas Dynamic Laser", Applied Physics Letters, Vol. 21, No 9, Nov. 1972, pp 432-433.